LBNL-39000
UC-1600

ERNEST ORLANDO LAWRENCE
BERKELEY NATIONAL LABORATORY

Wind-Induced Contaminant Transport in Near-Surface Soils with Application to Radon Entry into Buildings

W.J. Riley
Energy and Environment Division

May 1996
Ph.D. Thesis

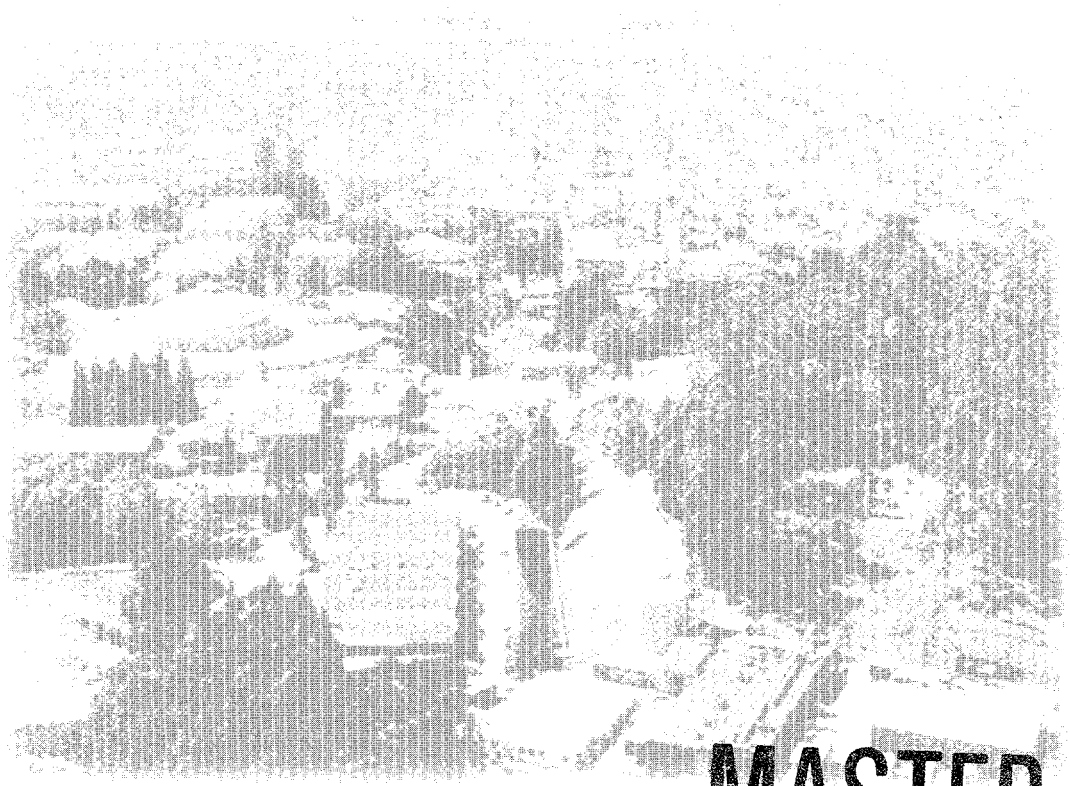

LBNL-39000
UC-1600

Wind-Induced Contaminant Transport in Near-Surface Soils with Application to Radon Entry into Buildings

William Jowett Riley
Ph.D. Thesis

May 1996

Departments of Engineering-Civil and Environmental
University of California at Berkeley

and

Indoor Environment Program
Energy and Environment Division
Lawrence Berkeley National Laboratory
University of California
Berkeley, CA 94720

This work was supported by the Director, Office of Energy Research, Office of Health and Environmental Research, Environmental Sciences Division, and by the Assistant Secretary for Energy Efficiency and Renewable Energy, Office of Building Technology, Building Systems and Materials Division, of the U.S. Department of Energy (DOE), under Contract DE-AC03-76SF00098.

Wind-Induced Contaminant Transport in Near-Surface Soils with Application to Radon Entry into Buildings

by

William Jowett Riley

B.S. (Rensselaer Polytechnic Institute) 1984
M.S. (University of North Carolina, Chapel Hill) 1988
M.S. (University of California, Berkeley) 1993

A dissertation submitted in partial satisfaction of the
requirements for the degree of
Doctor of Philosophy

in

Engineering-Civil and Environmental Engineering

in the

GRADUATE DIVISION

of the

UNIVERSITY OF CALIFORNIA at BERKELEY

Committee in Charge:

Professor William W. Nazaroff, co-Chair
Ashok J. Gadgil, Ph.D., co-Chair
Professor James R. Hunt
Professor John Harte

1996

Wind-Induced Contaminant Transport in Near-Surface Soils with Application to Radon Entry into Buildings

by

William Jowett Riley

Abstract

Wind-Induced Soil-Gas Contaminant Transport in Near-Surface Soils with Application to Radon Entry into Buildings

by

William Jowett Riley

Doctor of Philosophy in Engineering-Civil and Environmental Engineering

University of California at Berkeley

Professor William W. Nazaroff, co-Chair
Ashok J. Gadgil, Ph.D., co-Chair

Indoor air exposures to gaseous contaminants originating in soil can cause large human health risks. To predict and control these exposures, the mechanisms that affect vapor transport in near-surface soils need to be understood. In particular, radon exposure is a concern since average indoor radon concentrations lead to much higher risks than are generally accepted for exposure to other environmental contaminants. This dissertation examines an important component of the indoor radon problem: the impacts of wind on soil-gas and radon transport and entry into buildings. The research includes experimental and modeling studies of wind's interactions with a building's superstructure and the resulting soil-gas and radon flows

in the surrounding soil. In addition to exploring the effects of steady winds, we develop a novel modeling technique to examine the impacts of fluctuating winds on soil-gas and radon transport.

The original impetus for this investigation arose from the design and development of a passive radon mitigation system at the Lawrence Berkeley National Laboratory. That effort was initiated in response to the relatively high costs of subslab depressurization (SSD), a common active mitigation system. Chapter 2 quantifies the regional and national energy requirements, operating expenses, and CO_2 emissions associated with SSD system use. We estimate that operating SSD systems in U.S. houses where it is both appropriate and possible (about 2.6 million houses) would annually consume 1.7×10^4 TJ of end-use energy, cost $230 million (at current energy prices), and generate 2.0×10^9 kg of CO_2. These figures are central estimates; Chapter 2 presents the associated uncertainties.

The relatively high costs of SSD system operation prompted our research group to install and monitor a full-scale passive radon mitigation system in a house in Spokane, Washington. This study revealed that wind could strongly affect the mitigation system's performance. We therefore began to systematically investigate the impacts of wind on soil-gas radon transport and entry into buildings. Chapter 3 describes the results of a wind-tunnel experiment designed to measure the ground-surface pressure field established around a house in the presence of wind. We report wind-induced ground-surface pressure fields for several wind-incidence angles, two

atmospheric boundary layer structures, and two house geometries. Relatively small changes in the ground-surface pressure field resulted from perturbations in the atmospheric boundary layer structure (i.e., the surface roughness and displacement height) and the house geometry. The experimental results were compared to numerical predictions using a k-ε turbulence model. In most cases, this turbulence model is inappropriate for geometries with separated flow, as in the case of air flow over a building. However, we found the numerical model predictions of the ground-surface pressure field sufficiently accurate to predict wind-induced soil-gas contaminant transport.

The wind-induced ground-surface pressure field induces a bulk soil-gas flow which can flush radon from the soil adjacent to a building's basement. Chapter 4 investigates this phenomenon by presenting results from three-dimensional, steady-state simulations of wind-induced soil-gas and radon flow around a prototypical house. These simulations demonstrate that the wind-induced ground-surface pressure field can reduce the predicted radon entry rate, compared to that for a uniform ground-surface pressure field, by more than two orders of magnitude. We also present full-scale experimental measurements supporting the prediction that steady winds can depress soil-gas radon concentrations.

The finding that steady winds have a large impact on radon transport and entry rates motivated an investigation of the influence of transient winds on soil-gas and radon transport. Prior to this work, numerical models that could simulate this

geometrically complex, transient system did not exist. We therefore developed START, a transient, three-dimensional, finite-difference model of soil-gas and radon transport around a building. This model is computationally too expensive to conduct the simulations required to thoroughly investigate the effects of transient winds. Consequently, we apply START to generate unit-step responses, which characterize the temporal response of the soil-gas pressure field to changes in the wind speed.

To perform the three-dimensional simulations necessary to study the effects of transient winds on radon entry, we developed a novel simulation technique based on Duhamel's theorem. A software package (named RapidSTART) implements the technique, taking, as input, the unit-step responses generated by START. Duhamel's theorem describes a linear superposition method applicable to the simulation of the transient soil-gas pressure and velocity fields. Once the velocity field is generated, the model applies a standard finite-difference method to compute the soil-gas concentration field and radon entry rate. RapidSTART can simulate the effects of both fluctuating wind speed and wind direction on radon transport around and entry into houses. The simulations can be executed 500 to 5000 times faster (depending on the soil permeability) than comparable finite-difference simulations. This large reduction in computational time makes possible detailed analysis of transient, wind-induced soil-gas and radon transport.

We used the RapidSTART model to explore the effects of fluctuating winds on radon entry rates. Simulations were conducted for several wind signals and two

soil permeabilities. The simulation results indicate that fluctuations in wind speed characteristic of the peak in the wind-speed power spectrum have a negligible impact on the time-averaged radon entry rate. However, we found changes of up to 30% in the predicted radon entry rate when the fluctuating components of a real wind signal were included, as compared with the predictions for steady wind.

In summary, the results of this research demonstrate that the interactions of wind with near-surface soils can strongly affect soil-gas contaminant entry into buildings. The permeability-dependent flushing of radon from the soil gas below the building slab can dominate radon entry rate predictions. The development of RapidSTART is also an important product of this dissertation, representing the first application of Duhamel's theorem to the simulation of subsurface contaminant transport. The improvement in simulation runtime by three orders of magnitude, coupled with no loss of model accuracy, makes RapidSTART a very powerful tool for such investigations. In addition to the understanding gained regarding the subsurface transport of radon, the techniques and tools developed here apply to the study of passive and low-energy radon mitigation systems, the transport of other contaminants and trace gases in near-surface soils, and the simulation of other complex, transient systems.

Dedicated to my mother and father,
Alice and William Riley,
whose love and support have given me the
opportunity to pursue my dreams

TABLE OF CONTENTS

LIST OF FIGURES

CHAPTER 1

CHAPTER 2

CHAPTER 3

CHAPTER 4

CHAPTER 5

CHAPTER 6

CHAPTER 7

LIST OF TABLES

CHAPTER 2

CHAPTER 4

CHAPTER 5

CHAPTER 6

CHAPTER 7

ACKNOWLEDGMENTS

I thank my advisers, Bill Nazaroff and Ashok Gadgil, for their strong support and sincere interest in my education. There is no doubt in my mind that I was blessed with the best pair of mentors possible. I could always count on a smile, good ideas, and encouragement from Ashok, even when the situation seemed uncertain and the consequences dire. Bill's efforts on my behalf, his creative insights, and his contributions to this work will always be appreciated. I consider the examples Bill and Ashok set as individuals and scientists to be the most valuable part of the education I have received at Berkeley.

This dissertation represents a compilation of the efforts of many people. In addition to Ashok and Bill, I especially wish to thank Anushka Drescher, Bill Fisk, Phil Price, Allen Robinson, Tonny Sasse, and Rich Sextro for their intellectual contributions. Having access to such a wonderful group of people has made these four years an exceptional period of personal growth for me. I also wish to thank my office mate of three years, Anushka, for her constant smile and clear perspective on the goal. Her energy and enthusiasm made our office a great place to work. Conversations with Allen have been invaluable sources of ideas and venues for venting frustrations - thanks for the patience, and the help with the soil column

Joyce Cordell's efforts over the past four years have smoothed more rough times than I can remember. I appreciate all of your efforts on my behalf. Thanks also to Pat Johnson for her enthusiastic help.

The friendships I have formed at Berkeley have been the icing on the cake. Thanks everyone: Abra, Allen, Andy, Angus, Anushka, Carlos, Cheryl, David, Evan, Jenny, Jessica, Katie, Nikki, and Steve. I look forward to having more time to spend with all of you.

I am grateful for the financial support provided by the Indoor Environment Program of the Lawrence Berkeley National Laboratory. In the face of declining budgets, the Indoor Environment Program's constant support made this work possible. Thanks Ashok, Bill, and Rich for all of your work to see me through to the end.

I especially want to thank my parents, who have encouraged me to think for myself, have provided me with exceptional opportunities to learn and grow, and have given so much of themselves. I credit their love, dedication, and support for the opportunity to pursue my dreams.

CHAPTER 1

INTRODUCTION

1.1 Background

During the 1970's, exposure to radon's progeny in residential settings was shown to pose a serious human health risk. Subsequent research has revealed that indoor radon accounts for the single largest source of radiation exposure in the U.S. general population (Nero, 1988). Lung cancer is the primary health concern associated with radon exposure, although Henshaw et al. (1990) have presented evidence implicating radon as a cause of childhood leukemia. Lubin and Boice (1989) estimate that 10% of annual U.S. lung cancer deaths result from indoor radon. Even in houses with average concentrations, the estimated lifetime risk of lung cancer attributable to radon exposure is high; the EPA (1992) estimates a risk of 0.4% (4×10^{-3}), while the National Research Council (1988; 1991) estimates a risk of 0.7% (7×10^{-3}). Taken at face value, these numbers can be misleading, since epidemiological data show a synergism between radon and smoking that results in the risk of radon exposure to smokers being about 10 times larger than the risk to non-smokers (National Research Council, 1988). Nevertheless, the risk is orders of magnitude larger than the risks associated with many pollutants released from human activities into outdoor air or drinking water.

For example, the USEPA often sets standards to insure that risks associated with exposure to drinking water contaminants do not exceed 10^{-6}. These standards can force significant expenditures of societal resources. In this context, dedicating resources to reduce the relatively high risks associated with radon exposure appears to be a good investment.

Several studies have characterized indoor radon concentrations in the United States (Nero et al., 1986; EPA, 1992; Marcinowski et al., 1994). The reported indoor radon concentration distributions are well-described as lognormal. For example, Marcinowski et al. (1994) report a geometric mean and standard deviation of 28.5 Bq m^{-3} and 2.92, respectively, for all ground-contact homes in the nation. This distribution implies that 6.0% (or 5.7 million) of the houses in the U.S. exceed the EPA guideline of 148 Bq m^{-3}, and that 0.06% exceed 5 times the guideline.

The largest human radiation exposures in indoor air are associated with the progeny of ^{222}Rn (see Figure 1.1 for ^{222}Rn's decay chain). ^{222}Rn is a naturally occurring noble gas with a half life of about 3.8 days. The related isotope, ^{220}Rn, has a much shorter half life (50 s). This short lifetime leads to small migration distances in the soil; ^{220}Rn therefore does not significantly contribute to indoor radon concentrations (Schery, 1990). For this reason, we restrict the work presented in this dissertation to ^{222}Rn, hereafter referred to as "radon".

Of radon's progeny, the largest radiation dose to the lung results from the α-decays of ^{218}Po and ^{214}Po. Unlike ^{222}Rn, both of the Po isotopes are chemically

reactive, as are ^{214}Bi and ^{214}Pb. The β-decays of ^{214}Bi and ^{214}Pb, however, generate a much smaller radiation dose than that associated with the α-decays of the Po isotopes. The chemical reactivity of the Po, Bi, and Pb isotopes increases the probability of attachment directly to the lung or to particles in the air which subsequently can deposit on lung surfaces. The short half lives (less than 30 minutes) of radon's progeny also preclude them being effectively removed by the lung's clearance mechanisms.

1.1.1 Motivation for this Research

As the risks associated with exposure to radon's progeny became known, efforts to design, build, and understand radon mitigation systems were initiated. Currently, subslab depressurization (SSD) is the most commonly applied and thoroughly tested technique to reduce indoor radon concentrations (see Turk et al. (1987; 1991) for a description of other mitigation options). However, because SSD systems can be expensive to operate, several research groups have begun investigating the feasibility of using passive and low-energy mitigation systems.

The research presented in this dissertation stemmed from the study of a passive radon mitigation system developed at the Indoor Environment Program (IEP) of the Lawrence Berkeley National Laboratory (Fisk et al., 1995). After preliminary tests indicated that the mitigation system had the potential to significantly reduce indoor radon concentrations, a group from the IEP installed a full-scale version of the system in a house in Spokane, WA. The house was thoroughly instrumented to monitor the

system's long-term effectiveness and the influence of various environmental factors on the system's performance.

That study demonstrated that wind could strongly affect the performance of the passive mitigation system. The IEP group therefore began an inquiry into the relationship between wind, the operation of the mitigation system, and the subsurface transport of radon around the mitigated house. However, it was soon recognized that we lacked an understanding of the impacts of wind on radon transport around even very simple, unmitigated houses. A review of the literature showed that, during full-scale experiments, several investigators had observed a correlation between wind speed and soil-gas radon concentrations (Nazaroff et al., 1985; Turk et al., 1990). These studies, and our own preliminary modeling work, indicated that wind could substantially affect radon entry rates by altering the subsurface radon concentration field.

1.1.2 Entry Mechanisms and Driving Forces

Advective entry of radon-bearing soil gas is the dominant source of indoor radon in most homes with elevated concentrations (Nazaroff, 1992). In buildings with basements, a small depressurization can draw significant amounts of radon-laden soil gas through cracks in the substructure (such as the joint between the footer and the basement slab). Entry can also occur through permeable walls, especially those made from concrete blocks (Garbesi and Sextro, 1989). The small indoor-outdoor pressure difference (typically on the order of one to ten Pa) responsible for radon entry can be

generated by indoor-outdoor temperature differences, space conditioning equipment, mechanical exhaust, fluctuating barometric pressures, and the interaction of wind with the building superstructure. In addition to depressurizing the building, wind establishes a ground-surface pressure field around the building that influences soil-gas flow. Although the wind-induced ground-surface pressure field can dramatically affect the radon entry rate into the building, this feature has largely been ignored in previous modeling studies (Gadgil, 1992).

1.1.3 Previous Modeling Studies of Radon Transport and Entry

Simple analytical models have been employed to investigate the impacts of environmental and structural factors on radon entry into buildings. Nazaroff et al. (1987) used an electrical analogy to predict pressure coupling between a real basement and the surrounding soil gas. The model underpredicted the pressure coupling by more than a factor of 10. Mowris and Fisk (1988) developed analytical models to examine the impacts of exhaust ventilation on radon entry rates and indoor concentrations. They report that their simplified modeling approach predicted soil-gas entry rates to within 16% of predictions from a more detailed finite-difference model. However, the model was not tested against data from real houses. RAETRAD, a simulation code developed by Nielsen et al. (1994), was used to investigate the entry of radon to slab-on-grade houses. The model underpredicted indoor radon concentrations by about 50% when compared to a suite of 50 test houses.

Detailed numerical models, using finite-difference or finite-element techniques, have also been developed to study soil-gas radon transport and entry into buildings. The earliest of these models considered only advective radon transport in a uniform, isotropic soil (DSMA Atcon Ltd., 1983; Eaton and Scott, 1984; DSMA Atcon Ltd., 1985). Loureiro et al. (1990) developed a three-dimensional, steady-state, finite-difference model of radon and soil-gas transport around a house. That model allowed for variable soil characteristics and radon diffusion. Bonnefous et al. (1992) extended Loureiro's work by incorporating non-Darcy flow and applying the model to the study of active radon mitigation systems. Revzan et al. (1991; 1992) developed a two-dimensional, steady-state model based on Darcy's law that takes advantage of geometrical symmetry to significantly reduce model complexity and computational time. RN3D, a transient, finite-element model developed by Holford (1994), can simulate two- and simple three-dimensional geometries. Gadgil (1992) reviews several of the existing models of radon entry into houses, and discusses the strengths and weaknesses of the various approaches.

Models of radon transport and entry into buildings rely on the accuracy of both the soil and substructure characterization. Of the factors used to define the soil and house system, the soil permeability is probably the most important. Garbesi (1994) showed that soil permeability varies with the physical scale over which it is measured. She developed a technique to measure a single soil permeability value that corresponds to the scale at which the building interacts with the surrounding soil gas. Using this soil permeability to represent a homogeneous soil block greatly reduced previously

observed discrepancies between model predictions and experimental measurements of radon entry.

Two groups have performed numerical simulations in an attempt to quantify the effects of wind on radon entry (DSMA Atcon Ltd., 1985; Owczarski et al., 1991). However, neither of these modeling studies took into account the full three-dimensional, transient nature of the problem, nor did they attempt to explain the characteristics of the soil-gas and radon flows generated by wind.

1.2 Objectives of this Research

This dissertation aims to improve our understanding of the interactions of wind with soil gas and soil-gas contaminants in near-surface soils. Although many of the results can be generalized, we focus on the impacts of wind on radon's subsurface transport and entry into basement houses. We demonstrate that wind can significantly deplete soil-gas radon concentrations near the building. The wind-induced flushing of radon from soil gas, which can dominate predictions of indoor radon concentrations, was largely ignored in previous studies of the impacts of wind on radon entry into houses.

The heterogeneity of the ground-surface pressure field, the complexity of a typical house substructure, and the level of detail required in the spatial discretization make the study of the effects of fluctuating winds on radon transport computationally very expensive. To address this problem, we develop a novel modeling tool that can perform efficient simulations of wind-induced soil-gas and radon transport around

buildings. The model, called RapidSTART (Rapid *S*imulation of *T*ransient *A*ir and *R*adon *T*ransport), can perform these simulations thousands of times faster than a standard finite-difference model, thereby making the study of transient, wind-induced radon transport around buildings tractable.

Using the RapidSTART model, we examine the relative importance, with respect to radon entry rates, of the steady and fluctuating components of wind speed and direction. The development and application of the RapidSTART model is itself an important result of this research. We expect the technique can be productively applied to the simulation of other contaminants (e.g., volatile organic compounds (VOC's)) and other complex linear systems subject to transient boundary conditions.

The research described here relates to a broader effort by the IEP to investigate soil-gas and contaminant entry into buildings. In this context, IEP's research goals have included several specific objectives: (1) determining and quantifying the sources and sinks of indoor air contaminants (particularly radon, but including, for example, VOC's); (2) developing an understanding of the factors that affect the subsurface transport of soil-gas contaminants; (3) applying this understanding to the development of numerical models that can predict contaminant entry for a range of building geometries and environmental conditions; and (4) designing and testing radon mitigation techniques. This dissertation applies primarily to the second and third of these goals, although RapidSTART will undoubtedly be a useful tool in the development of passive or low-energy radon mitigation systems.

1.3 Outline of Dissertation

This section highlights the topics covered in the remainder of this dissertation. We begin by quantifying the costs of SSD system operation in Chapter 2. Chapters 3 and 4 report on the impacts of steady winds on radon transport and entry into a prototypical house. We develop the three-dimensional, transient modeling tools START and RapidSTART in Chapters 5 and 6, respectively. Chapter 7 applies RapidSTART to examine the impacts of fluctuating winds on soil-gas and radon entry into houses. Finally, Chapter 8 summarizes our findings, and indicates directions for future research. The remainder of this section presents details of the specific topics discussed in each chapter.

Chapter 2 quantifies the regional and national costs associated with active radon mitigation (i.e., subslab depressurization (SSD)) systems. We conclude that if SSD systems were installed nationally in houses where it is both necessary and possible (about 2.6 million homes), the systems would annually consume 1.7×10^4 (6.4×10^3 to 3.9×10^4) TJ of end-use energy, cost $230 ($130 to $400) million (at current energy prices), and generate 2.0×10^9 (1.2×10^9 to 3.5×10^9) kg of CO_2. These figures represent our central estimates and expected ranges of possible values. The relatively high costs of SSD system operation demonstrate the need to develop passive, or low-energy, radon mitigation systems.

Chapter 3 presents the results of a wind-tunnel study designed to measure the wind-induced ground-surface pressure field for several wind-incidence angles, two

atmospheric boundary layer structures, and two house geometries. These parameters were chosen to bound conditions around typical single-family homes.

Chapter 4 describes a study examining the effects of steady winds on soil-gas and radon transport around a prototypical house. The investigation combines the ground-surface pressure fields generated in the wind tunnel (Chapter 3), a previously tested steady-state soil-gas and radon transport model, a three-dimensional Navier-Stokes model of air flow over the house, and models of wind's impact on indoor depressurization and the building's ventilation rate. We accomplished several goals with this framework. First, we determined the complex soil-gas flow patterns resulting from the spatially heterogeneous wind-induced ground-surface pressure field. Second, the "flushing" effect of these soil-gas flows on the radon concentration field was quantified. Finally, we calculated the impact of wind on the radon entry rate and indoor radon concentration. Comparisons were made to simulations that ignored the wind-induced ground-surface pressure field, which has been common practice. Chapter 4 also presents experimental measurements from several houses of simultaneous wind speed and subslab soil-gas radon concentration measurements. These experimental results support our contention that wind can significantly deplete the soil-gas radon concentration near the building. We conclude that the wind-induced ground-surface pressures can dominate near-surface transport of soil gas and radon, thereby strongly affecting radon entry rates.

The large impacts of steady winds on indoor radon concentrations motivated us to further our understanding by including fluctuating winds in the analysis. Prior to this

work there was not, to our knowledge, a modeling tool capable of practically simulating the transient, three-dimensional soil-gas and radon concentration fields generated by fluctuating winds.

Chapter 5 describes the development and validation of START, a transient, three-dimensional, finite-difference soil-gas and radon transport model. Although capable of modeling the effects of fluctuating winds on the subsurface transport of radon, START is computationally very expensive when simulating transient, three-dimensional problems. The model can, however, practically simulate one- and two-dimensional systems of soil-gas and radon flow. We validate START by comparing simulation predictions to four analytical solutions of flow through a soil column and experimental results from a well-characterized basement structure. The model performed exceptionally well in all of these tests.

For the objective of simulating radon entry due to fluctuating winds, we use START to generate the unit-step response of the soil-gas pressure field. The unit-step response characterizes the temporal response of the soil-gas pressure field to an instantaneous change in boundary conditions. For wind-induced soil-gas transport, the boundary conditions of interest are the ground-surface pressure field and the basement depressurization. Other transient boundary conditions can also be modeled by START for use as input to RapidSTART. For example, we have employed START to generate the response of the soil-gas pressure field to a unit change in atmospheric pressure. With this information, RapidSTART can simulate the transport of soil gas and radon around a building in the presence of a fluctuating atmospheric pressure signal.

Robinson et al. (1995b) have shown that, under some conditions, atmospheric pressure fluctuations are an important driving force for radon entry.

Chapter 6 presents the RapidSTART model, which simulates the soil-gas pressure field by applying a linear superposition technique described by Duhamel's theorem (Duhamel, 1833; Myers, 1987). We then use a standard finite-difference technique to compute the radon concentration field. Since winds fluctuate in direction as well as speed, a method to model this feature in RapidSTART has also been developed. Although modeling a wind signal with a fluctuating direction does not increase the RapidSTART simulation time, generating the additional unit-step responses can be computationally expensive.

The linear superposition theorem used in the development of RapidSTART has been applied to the study of heat transfer in solids (Myers, 1987) and a few groundwater systems (Pinder et al., 1969; Moench et al., 1974; Weeks, 1978). More recently, Robinson et al. (1995a; 1995b) have employed the concept to examine the effects of fluctuating atmospheric pressures on soil-gas entry into buildings. To our knowledge, the technique has not been applied in the manner presented here to simulate the transport of a subsurface contaminant.

The final sections of Chapter 6 present the validation tests of the RapidSTART model. We demonstrate that RapidSTART can accurately and efficiently simulate soil-gas and radon entry into houses. Compared to the finite-difference model START, RapidSTART reduces simulation runtimes by a factor of between 500 and 5000, depending on the system's characteristics (i.e., the soil permeability).

Chapter 7 applies RapidSTART to examine the impacts of fluctuating winds on radon entry into a prototypical residence. Simulations are performed for two soil permeabilities and both artificial and real wind signals. These simulations indicate that, for soil permeabilities of 10^{-8} and 10^{-10} m^2 (and fixed wind direction), a fluctuating wind speed characteristic of the peak in the wind-speed power spectrum has a negligible impact on radon entry into houses. However, our results demonstrate that a fluctuating wind direction can affect the predicted radon entry rates by up to 30%.

Chapter 8 summarizes the findings of this research. Although our study has focused on houses with basements, we expect that the impacts of the wind-induced ground-surface pressure field on radon entry rates will be qualitatively similar for slab-on-grade and crawl-space houses. We discuss potential applications of the RapidSTART model to the study of other soil-gas contaminants and topics, and propose several specific projects. For example, many of the same factors that affect radon transport will impact the entry into buildings of other soil-gas contaminants, such as VOC's. Also, soil-atmosphere interactions significantly impact fluxes of water vapor and trace gases, both of which act to regulate the global climate. The understanding and tools developed during this dissertation may prove useful in investigating a wide range of such topics.

1.4 References

Bonnefous Y. C., Gadgil A. J., Fisk W. J., Prill R. J., and Nematollahi A. R. (1992) Field study and numerical simulation of subslab ventilation systems, *Environ. Sci. Technol.* **26**, 1752-1759.

DSMA Atcon Ltd. (1983) Review of existing information and evaluation for possibilities of research and development of instrumentation to determine future levels of radon at a proposed building site, report INFO-0096, Atomic Energy Control Board, Ottawa, Canada.

DSMA Atcon Ltd. (1985) A computer study of soil gas movement into buildings, report 1389/1333, Department of Health and Welfare, Ottawa, Canada.

Duhamel (1833) Memoire sur la methode generale relative au mouvement de la chaleur dans les corps solides plonges dans les milieux dont la temperature varie avec le temps, *J. Ec. Polyt. Paris* **14**, 20.

Eaton R. S. and Scott A. G. (1984) Understanding radon transport into houses, *Radiat. Prot. Dosim.* **7**, 251-253.

EPA (1992) National residential radon survey, EPA 402-R-92-011, Environmental Protection Agency, Washington, D.C.

Fisk W. J., Prill R. J., Wooley J., Bonnefous Y. C., Gadgil A. J., and Riley W. J. (1995) New methods of energy efficient radon mitigation, *Health Phys.* **68**, 689-698.

Gadgil A. (1992) Models of radon entry, *Radiation Protection Dosimetry* **45**, 373-380.

Garbesi K. (1994) Toward resolving model-measurement discrepancies of radon entry into houses, Ph.D. Thesis, report LBL-34244, Lawrence Berkeley National Laboratory, Berkeley, CA.

Garbesi K. and Sextro R. G. (1989) Modeling and field evidence of pressure-driven entry of soil gas into a house through permeable below-grade walls, *Environ. Sci. Technol.* **23**, 1481-1487.

Henshaw D. L., Eatough J. P., and Richardson R. B. (1990) Radon as a causative factor in induction of myeloid leukaemia and other cancers, *Lancet* **335**, 1008-1012.

Holford D. J. (1994) Rn3d: A finite element code for simulating gas flow and radon transport in variably saturated, nonisothermal porous media: User's manual, Version 1.0, PNL-8943, Pacific Northwest Laboratory, Richland, WA 99352.

Loureiro C. O., Abriola L. M., Martin J. E., and Sextro R. G. (1990) Three-dimensional simulation of radon transport into houses with basements under constant negative pressure, *Environ. Sci. Technol.* **24**, 1338-1348.

Lubin J. H. and Boice Jr. J. D. (1989) Estimating Rn induced lung cancer in the United States, *Health Phys.* **57**, 417-427.

Marcinowski F., Lucas R. M., and Yeager W. M. (1994) National and regional distributions of airborne radon concentrations in United States homes, *Health Phys.* **66**, 699-706.

Moench A. F., Sauer V. B., and Jennings M. E. (1974) Modification of routed streamflow by channel loss and base flow, *Wat. Resour. Res.* **10**, 963-968.

Mowris R. J. and Fisk W. J. (1988) Modeling the effects of exhaust ventilation on ^{222}Rn entry rates and indoor ^{222}Rn concentrations, *Health Phys.* **54**, 491-501.

Myers G. E. (1987) *Analytical Methods in Conduction Heat Transfer,* Genium Publishing Corporation, Schenectady, NY.

National Research Council (1988) *Health Risks of Radon and Other Internally Deposited Alpha-Emitters. BEIR IV,* National Academy Press, Washington, DC.

National Research Council (1991) *Comparative Dosimetry of Radon in Mines and Homes,* Panel on Dosimetric Assumptions Affecting the Application of Radon Risk Estimates, National Academy Press, Washington, DC.

Nazaroff W. W. (1992) Radon transport from soil to air, *Reviews of Geophysics* **30**, 137-160.

Nazaroff W. W., Feustel H., Nero A. V., Revzan K. L., Grimsrud D. T., Essling M. A., and Toohey R. E. (1985) Radon transport into a detached one-story house with a basement, *Atmos. Environ.* **19**, 31-43.

Nazaroff W. W., Lewis S. R., Doyle S. M., Moed B. A., and Nero A. V. (1987) Experiments on pollutant transport from soil into residential basements by pressure-driven airflow, *Environ. Sci. Technol.* **21**, 459-466.

Nero A. V. (1988) Radon and its decay products in indoor air: an overview, In Nazaroff W. W. and Nero A. V. (Ed.) *Radon and Its Decay Products in Indoor Air*, John Wiley and Sons, New York, 1-53.

Nero A. V., Schwehr M. B., Nazaroff W. W., and Revzan K. L. (1986) Distribution of airborne radon-222 in U.S. homes, *Science* **234**, 992-997.

Nielson K. K., Rogers V. C., Rogers V., and Rodger H. B. (1994) The RAETRAD model of radon generation and transport from soils into slab-on-grade houses, *Health Phys.* **67**, 363-377.

Owczarski P. C., Holford D. J., Burk K. W., Freeman H. D., and Gee G. W. (1991) Effect of winds in reducing sub-slab radon concentrations under houses laid over gravel beds, Proc. of The 1991 International Symposium on Radon and Radon Reduction Technology, Philadelphia, PA, USEPA, Air and Energy Environmental Research Laboratory, Research Triangle Park, NC.

Pinder G. F., Bredehoeft J. D., and Cooper H. H. J. (1969) Determination of aquifer diffusivity from aquifer response to fluctuations in river stage, *Wat. Resour. Res.* **5**, 850-855.

Revzan K. and Fisk W. (1992) Modeling radon entry into houses with basements: The influence of structural factors, *Indoor Air* **2**, 40-48.

Revzan K. L., Fisk W. J., and Gadgil A. J. (1991) Modeling radon entry into houses with basements: Model description and verification, *Indoor Air* **1**, 173-189.

Robinson A. L., Sextro R. G., and Fisk W. J. (1995a) Soil-gas entry into houses driven by atmospheric pressure fluctuations, part 1 --- Measurements, spectral analysis, and model comparison, report LBL-38232, Lawrence Berkeley National Laboratory, Berkeley CA.

Robinson A. L., Sextro R. G., and Riley W. J. (1995b) Soil-gas entry into houses driven by atmospheric pressure fluctuations, part 2 --- The influence of soil and structural factors, report LBL-38233, Lawrence Berkeley National Laboratory, Berkeley, CA.

Schery S. D. (1990) Thoron in the environment, *J. Air Waste Management Assoc.* **40**, 493-497.

Turk B. H., Harrison J., and Sextro R. G. (1991) Performance of radon control systems, *Energy Build.* **17**, 157-175.

Turk B. H., Prill R. J., Grimsrud D. R., Moed B. A., and Sextro R. G. (1990) Characterizing the occurrence, sources and variability of radon in Pacific Northwest homes, *J. Air Waste Mange. Assoc.* **40**, 498-506.

Turk B. H., Prill R. J., Grimsrud D. T., Moed B. A., and Sextro R. G. (1987) Radon and remedial action in Spokane Valley homes, volume I: Experimental design and data analysis, report LBL-23430, Lawrence Berkeley National Laboratory, Berkeley, CA.

Weeks E. P. (1978) Field determination of vertical permeability to air in the unsaturated zone, U.S. Geological Survey Professional Paper 1051, United States Government Printing Office, Washington, DC.

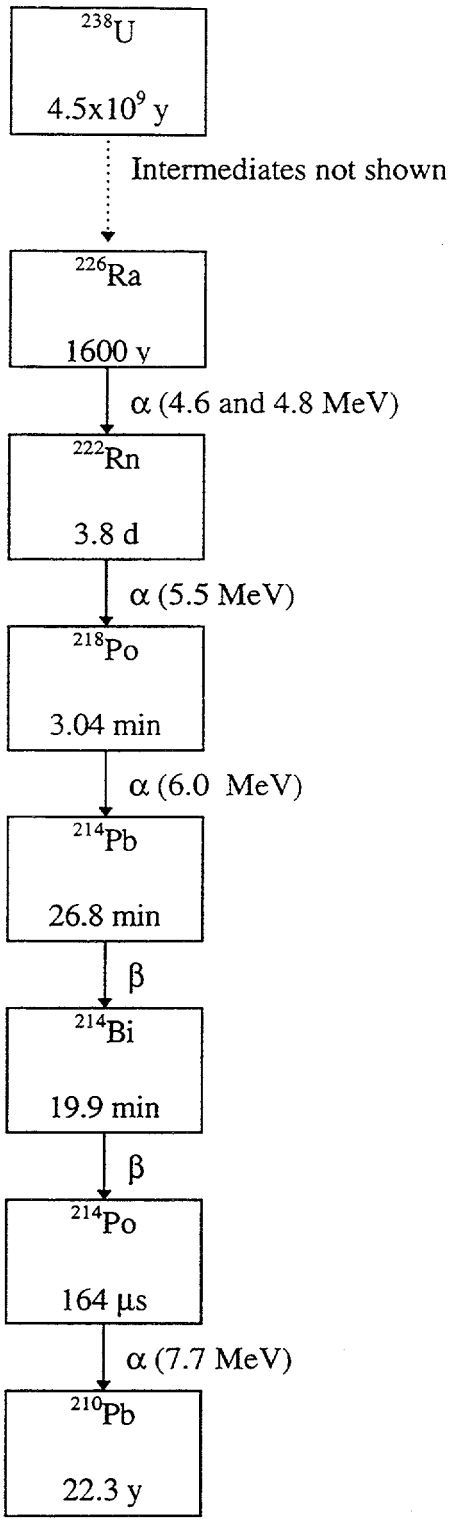

Figure 1.1. The radioactive decay chain containing ^{222}Rn. The boxes show the isotopes and their half lives. The energy associated with alpha decays are given in parenthesis.

CHAPTER 2

REGIONAL AND NATIONAL ESTIMATES OF THE POTENTIAL ENERGY USE, ENERGY COST, AND CO_2 EMISSIONS ASSOCIATED WITH RADON MITIGATION BY SUBSLAB DEPRESSURIZATION*

2.1 Abstract

Active subslab depressurization (SSD) systems are an effective means of reducing indoor radon concentrations in residential buildings. However, energy is required to operate the system fan and to condition the resulting increased building ventilation. We present regional and national estimates of the energy requirements, operating expenses, and CO_2 emissions associated with using SSD systems at saturation (i.e., in all U.S. homes with radon concentrations above the EPA remediation guideline and either basement or slab-on-grade construction). The primary source of uncertainty in these estimates is the impact of the SSD system on house ventilation rate. Overall, individual SSD system operating expenses are highest in the Northeast and Midwest at about \$99 y^{-1}, and lowest in the South and West at about

---

* This chapter is based on a paper: Riley, W. J., W. J. Fisk, and A. J. Gadgil (1996) Regional and national estimates of the potential energy use, energy cost, and CO_2 emissions associated with radon mitigation by sub-slab depressurization, accepted for publication in *Energy and Buildings*.

$66 y^{-1}. The fan consumes, on average, about 40% of the end-use energy needed to operate the SSD system and accounts for about 60% of the annual expense. At saturation, regional impacts are largest in the Midwest because this area has a large number of mitigable houses and a relatively high heating load. We estimate that operating SSD systems in U.S. houses where it is both appropriate and possible (about 2.6 million houses), would annually consume 1.7×10^4 (6.4×10^3 to 3.9×10^4) TJ of end-use energy, cost $230 ($130 to $400) million (at current energy prices), and generate 2.0×10^9 (1.2×10^9 to 3.5×10^9) kg of CO_2. Passive or energy efficient radon mitigation systems currently being developed offer opportunities to substantially reduce these impacts.

2.2 Nomenclature

C_c cost to cool the additional air flow for an average house ($ y^{-1} per house)

C_f cost to run the SSD system fan ($ y^{-1} per house)

C_{fuel} fuel cost ($ GJ^{-1})

C_h cost to heat the additional air flow for an average house ($ y^{-1} per house)

C_{hi} cost to heat the additional air flow for the ith fuel type ($ y^{-1} per house)

c_p heat capacity of air (1000 J kg^{-1} K^{-1})

E_c energy required to cool the additional air flow for an average house (GJ y^{-1} per house)

e_{CO_2} regional CO_2 emission factor ($kgCO_2$ GJ^{-1})

E_f energy required to run the SSD system fan for an average house (GJ y^{-1} per house)

E_h energy required to heat the increased air flow for an average house (GJ y^{-1} per house)

E_{hi} energy required to heat the increased air flow for the "i - th" fuel type (GJ y^{-1} per house)

E_{lh} latent-heat energy demand for an average house (GJ y^{-1} per house)

f_{AC}	fraction of single-family homes with air conditioners (-)
f_i	fraction of houses that use the "i - th" fuel type (-)
f_{use}	fraction of houses with air conditioners that are used regularly (-)
M_c	mass of CO_2 emitted from producing the cooling energy ($kgCO_2\ y^{-1}$ per house)
m_{CO_2}	regional CO_2 emissions ($10^3\ tCO_2$)
M_f	mass of CO_2 emitted from producing the fan energy ($kgCO_2\ y^{-1}$ per house)
M_h	mass of CO_2 emitted from producing the heating energy ($kgCO_2\ y^{-1}$ per house)
M_{hi}	mass of CO_2 emitted for the ith type of heating fuel ($kgCO_2\ y^{-1}$ per house)
N_{CDD}	annual number of cooling degree days for each region ($K\ d\ y^{-1}$)
N_H	number of houses in which an SSD system is appropriate (-)
N_{HDD}	annual number of heating degree days ($K\ d\ y^{-1}$)
N_{LHD}	annual number of latent enthalpy-days ($J\ d\ kg^{-1}\ y^{-1}$)
Q	effective house ventilation rate with the SSD system operating ($m^3\ s^{-1}$)
Q_0	unperturbed house ventilation rate ($m^3\ s^{-1}$)
Q_{SSD}	flow through the SSD pipes ($m^3\ s^{-1}$)
R	ratio of the latent heat to sensible cooling energy load (-)

S	regional electric utility sales (GWh)

Greek letters

η_h	efficiency of the heating and distribution system (-)
η_c	efficiency of the cooling and distribution system (-)
η_d	efficiency of the distribution system (-)
η_e	heating equipment efficiency (-)
ρ	air density (1.2 kg m^{-3})

Note: (-) indicates a nondimensional variable.

2.3 Introduction

Subslab depressurization (SSD) is the most commonly applied and thoroughly tested technique for reducing radon entry into houses. The system typically consists of a pit in the subslab gravel layer into which a pipe connected to outdoor air has been inserted ((EPA, 1994); Figure 2.1). A small fan coupled to the pipe draws radon-bearing soil gas from the gravel layer and exhausts it to the outdoors. To be effective, the SSD system must establish a positive pressure difference between the basement and the gravel layer. This requirement drives the selection of fan power and placement of the system pit(s).

An SSD system can be installed at the time of construction or as a retrofit. For many houses, the systems are effective at reducing indoor radon concentrations, although the system's energy requirements can be considerable. In addition to removing soil gas and radon from below the slab, house air is drawn into the gravel layer and exhausted to the outdoors. The overall house ventilation rate therefore increases. Energy must be supplied to condition this increased air flow and to power the system fan.

Several investigators have studied the energy use and costs associated with SSD system operation in individual houses. Clarkin et al. (1990) performed tracer-gas decay experiments in one Pennsylvania and two Virginia homes to determine the additional house ventilation generated by a SSD system. For these houses they estimated an increase in annual heating costs ranging from $4 to $32. Bohac et al.

(1991) studied a group of houses in the Twin Cities metropolitan area. They concluded that the SSD systems increased the annual energy expense by $75. About half of this expense was due to increased heating requirements; the remainder was due to operation of the system fan. Henschel (1991) examined SSD system operating costs for both a 50 and 90 W fan. He reports annual fan energy costs of $35 and $63 for the 50 and 90 W fan, respectively, and corresponding incremental conditioning costs of $39 and $79. Fisk et al. (1995) estimate that the annual increase in energy expense resulting from SSD system use in a Chicago climate is $42 for homes with gas heat, and $165 for electric resistance heat. Bonnefous et al. (1994), using a numerical model to estimate the increase in house ventilation from an SSD system with two fans, predict an annual incremental heating expense of $345 for a Chicago climate. The use of two SSD system fans in these simulations explains the large predicted increase in heating expense. As this SSD system configuration is relatively unusual, we have not incorporated these modeling results into our calculations. Groups in Canada (Sanchez, 1987) and Sweden (Ericson et al., 1984; Ericson and Schmied, 1987) have also examined SSD system effectiveness and installation costs. Ericson et al. (1984) report annual operating costs of $12 (1984 dollars). This amount does not include costs associated with the increased building ventilation caused by SSD system operation.

These estimates are all for specific homes or for an average home in a specific climate. No effort has yet been made to determine the regional and national energy implications of SSD system operation at saturation. The purpose of this study is to make such estimates. We consider regional distributions of housing characteristics,

types of heating fuels used, and heating and cooling loads. Estimates of SSD system operating expenses are computed using regional fuel prices. The CO_2 emissions associated with SSD system operation are computed by considering each region's mix of fuel use and the emission factor associated with each fuel. This parameter is presented as a metric of the potential environmental effects associated with SSD energy use.

2.4 Methods

2.4.1 Overview

To estimate the energy, cost, and CO_2 emission implications of SSD operation, we have combined data from field tests and national surveys of housing characteristics and fuel use. For an average house in each region, we determine the heating, cooling, and fan energy requirements of SSD system operation. We then calculate the number of houses in each region where an SSD system would be appropriate. In particular, these are the houses with a basement or slab-on-grade construction whose radon concentrations are above the EPA remediation guideline of 148 Bq m^{-3}.

The additional house ventilation generated by SSD system operation is estimated from the results of four field studies. This estimate is the largest source of uncertainty in our calculations, primarily because the available data are limited. We therefore provide a range of values for our predictions based on this uncertainty.

Space conditioning costs are computed by means of a degree-day method (ASHRAE, 1993) that accounts for heating and cooling equipment and air distribution system efficiencies. The significant regional variation in fuel costs, types of heating fuel used, and CO_2 emission factors are included in our determination of cost and CO_2 emissions.

We have neglected the additional heating load imposed on the house by the SSD system drawing cool air through the soil and decreasing winter-time soil temperatures. A complex computer model would be required to accurately estimate the effect of soil cooling on the overall energy requirements of the SSD system. However, assuming that 50% of the air flow out of the SSD system originates from outdoors and 50% from indoors, conservation of energy dictates that this conduction heating load can be no greater than the increased heating load from additional infiltration. In reality, the additional load associated with soil cooling is likely to be substantially smaller than the loads calculated in this paper, and neglecting it makes our estimates of cost and energy use conservative (i.e., real cost and energy increases are likely to be somewhat higher than our estimates).

2.4.2 Census and EPA Regions

We have estimated the impacts associated with SSD operation both for census regions and on a national basis. The indoor radon concentration data available to us are divided into EPA regions (Marcinowski et al., 1994), and do not exactly match the census regions. Table 2.1 shows the division of states into the four census regions:

Northeast (NE), Midwest (MW), South (S), and West (W). We group EPA regions 1 and 2 into the NE census region; EPA regions 5 and 7 into the MW census region; EPA regions 3, 4, and 6 into the S census region; and EPA regions 8, 9, and 10 into the W census region. There are four states which do not fit this categorization: Pennsylvania (EPA region 3, is placed in the NE census region), North and South Dakota (EPA region 8, are placed in the MW census region), and New Mexico (EPA region 6, is placed in the S census region). We expect that the error associated with grouping these four states as described is small.

2.4.3 SSD-Induced House Ventilation

In addition to removing radon-bearing soil gas from below the slab, SSD systems increase the house ventilation rate. We use data collected during four studies of installed SSD systems to estimate this increase in air flow through the house. Two of the studies (Turk et al., 1987; Turk et al., 1991) used tracer-gas decay with and without SSD operation to measure the increase in house ventilation caused by the SSD system. Turk et al. (1987) measured an average increase of 5×10^{-3} m^3 s^{-1} in seven Pacific Northwest homes. In a study of five New Jersey homes, Turk et al. (1991) report an average increase in ventilation rate of 2.5×10^{-2} m^3 s^{-1}.

The other two studies (Clarkin et al., 1990; Bohac et al., 1993) measured flow rates through the SSD pipes and the proportion of the flow that originated in the house. To estimate the increase in house ventilation rate for these two studies we use an equation from the LBL infiltration model (Sherman, 1980)

$$Q = \sqrt{Q_0^{\,2} + Q_{SSD}^{\,2}} \tag{2.1}$$

where Q is the effective house ventilation rate with the SSD system operating ($m^3 \cdot s^{-1}$), Q_0 is an estimate of the unperturbed house ventilation rate ($m^3\ s^{-1}$), and Q_{SSD} is the portion of the flow through the SSD pipes ($m^3\ s^{-1}$) that originated in the house. The increase in ventilation due to SSD operation is then estimated as $Q - Q_0$. The flows in equation (2.1) are added in quadrature since we assume that the superposition of Q_0 and Q_{SSD} can be treated as a sum of their effects on the building pressure. For a structure whose crack resistances are dominated by inertial forces, the pressure drop will be proportional to the square of the flow rate through the crack. This approximation appears to work well for many buildings (Sherman, 1980).

To utilize equation (2.1), an estimate of a typical house ventilation rate, Q_0, is required. Pandian et al. (1993) summarized residential ventilation data based on 1836 perfluorocarbon tracer measurements across the U.S. They report an arithmetic mean and standard deviation of 0.60 and 2.2 h^{-1}, respectively, for houses in the Northeast (this region is different than the NE region we have defined, but includes the areas of the Bohac et al. (1993) and Clarkin et al. (1990) studies). The national average heated floor area for single-family homes is 173 m^2 (RECS, 1992). Therefore, assuming a ceiling height of 2.4 m (8 ft) and using the arithmetic mean air-exchange rate, Q_0 is $6.9 \times 10^{-2}\ m^3\ s^{-1}$.

Table 2.2 summarizes the results from these four studies. The average increase in ventilation rate produced by the 20 SSD systems is 9×10^{-3} m^3 s^{-1}, with a range from -10×10^{-3} to 70×10^{-3} m^3 s^{-1}. It is not possible, given our understanding of the system, for the house ventilation rate to decrease as a result of SSD system operation. We hypothesize that the two decreases observed in the Spokane study(Turk et al., 1987) are a result of factors other than the SSD system (e.g., wind). The value of 6.9×10^{-2} m^3 s^{-1} (in the N.J. study (Turk et al., 1991)) is a significantly larger flow than the system fan is capable of generating. Again, we hypothesize that an external factor is responsible for this large increase. These three values do not, however, significantly affect the mean. The mean increase in ventilation rate calculated from the entire dataset (9×10^{-3} m^3 s^{-1}) is used as the estimate of additional air that must be conditioned throughout the year.

The approximation that this increase in ventilation rate is constant over time implies that varying weather conditions do not have a large impact on the increase in ventilation due to SSD system operation. Given the large uncertainty in the average value of the increase in ventilation rate, our estimate would not be substantially improved by attempting to account for weather effects. We make the further approximation that the ventilation rate measurements of the four studies were made during weather conditions representative of the average. The paucity of data, both geographically and temporally, prevents us from improving on this approximation.

For comparison, Henschel (1991) assumed a SSD-induced increase in house ventilation of 1.8×10^{-2} m^3 s^{-1} for a 90 W fan. However, that estimate is not based on data from real SSD systems. Fisk et al. (1995) report an increased ventilation rate of 2.0×10^{-2} m^3 s^{-1}, based on a subset of the studies listed in Table 2.2 and on the simulations reported by Bonnefous et al. (1994). The current study improves on these estimates by including more data from installed SSD systems.

If the data for the increase in ventilation rate were statistically independent and normally distributed, the 95% confidence interval for the mean increase across the housing stock would be 4.5×10^{-3} to 1.1×10^{-2} m^3 s^{-1}. However, the data are neither normally distributed nor independent, nor is the dataset large enough to formally correct for these circumstances. To estimate uncertainty in SSD-induced ventilation, we therefore choose a range bounded by the minimum and maximum averages from each of the four studies mentioned above, or 6.8×10^{-4} (Clarkin et al., 1990) to 2.5×10^{-2} m^3 s^{-1} (Turk et al., 1991). Thirteen of the twenty datapoints fall within this range. The uncertainty in the increased house ventilation rate dominates the error in our predictions of SSD energy use, operating costs, and CO_2 emissions. We therefore report a mean and an uncertainty range for each of these parameters based on the above approximations.

2.4.4 Heating Energy Requirements

The mix of fuels used to heat homes varies with region. We define f_i to be the fraction of houses that use the "i-th" fuel type for heating in each region of the country. In the Northeast, natural gas and fuel oil constitute the major heating energy sources. Natural gas and electricity are the major sources in the South, and natural gas is the largest source in the West and Midwest.

The energy required to heat the increased air flow through the house for the "i-th" fuel type, E_{hi} (GJ y^{-1} per house), is

$$E_{hi} = \frac{(Q - Q_0)\rho c_p N_{HDD}}{\eta_h}\left(\frac{8.64\text{x}10^4 \text{ s}}{\text{day}}\right)\left(\frac{\text{GJ}}{10^9 \text{ J}}\right) \tag{2.2}$$

where ρ is the air density (1.2 kg m^{-3}), c_p is the heat capacity of air (1000 J kg^{-1} K^{-1}), N_{HDD} is the annual number of heating degree days (K d y^{-1}), and η_h is the overall efficiency of the heating and distribution system (-). The number of heating degree-days, for a single day, is 18 °C minus the day's average temperature if the result is a positive number, and 0 if it is a negative number. For this study, we use "normal heating degree-days", which is the average number of heating degree-days per year between 1951 and 1980 (RECS, 1992). N_{HDD} varies by fuel type because the geographic distribution of fuel-type use is not homogeneous within each region.

The overall efficiency of each heating device is evaluated as

$$\eta_h = \eta_e \eta_d \tag{2.3}$$

where η_e is the equipment (e.g., furnace) efficiency for the particular fuel type (-), and η_d is the efficiency of the distribution system in delivering the conditioned air (-). The population-weighted national average equipment efficiency for LPG, natural gas, and fuel oil furnaces is 0.68 (GRI, 1993). We take the equipment efficiency of electric furnaces to be 1.0, of kerosene heaters to be 0.70, and wood stoves to be 0.30 (Boghosian, 1994).

In a study of houses with basements, Treidler and Modera (1994) predict a duct distribution efficiency of 0.83. This efficiency is an average from three prototypical houses (one each in Georgia, Minnesota, and the District of Columbia), and considers both heating and cooling losses. In another paper, Modera (1993) reports a 0.6-0.7 distribution efficiency for a house in a moderate California climate. For this study, we approximate the distribution system efficiency to be 0.75 for electric (we assume that baseboard electric heaters constitute a small proportion of all electric heating devices), LPG, natural gas, and fuel oil furnaces. A distribution efficiency of 1.0 is used for kerosene and wood heaters.

The energy required to heat the increased ventilation flow for an average house, E_h (GJ y^{-1} per house), in each region is

$$E_h = \sum_{fuels} f_i E_{hi} \tag{2.4}$$

2.4.5 Cooling Energy Requirements

We assume the increase in ventilation flow produced by the SSD system during the cooling season is the same as during the heating system ($Q = 9\times10^{-3}$ m^3 s^{-1}). Ninety nine percent of the central air conditioners in the United States are electric; the remaining are either LPG or natural gas (RECS, 1992; Table 54). For simplicity, we assume that all the air conditioners in the country are electric.

The fraction of single-family homes with air conditioners, f_{AC} (-), is approximated by the ratio of the number of households with air conditioners to the total number of households in each region. In contrast to our assumption regarding the use of heating equipment, we assume that not all homes with air conditioners use them regularly. In the RECS (1992) survey, households were asked how often they used their air conditioners. Four categories were available: "not at all", "only a few times", "quite a bit", and "all summer". We take the fraction of houses with air conditioners who use them regularly, f_{use} (-), to be the fraction of households that declare a usage of "quite a bit" or "all summer".

The annual number of cooling degree days for each region, N_{CDD} (K d y^{-1}), is determined analogously to N_{HDD}. We use an average stock efficiency for the air conditioner of 8.09 Btu W^{-1} h^{-1} (Hanford et al., 1994) and a distribution system efficiency of 0.75. The coefficient of performance is therefore 2.4. The overall cooling system efficiency, η_c (-), is the product of the coefficient of performance and the distribution efficiency, or 1.78.

In addition to the sensible energy required to cool the air, there is a latent-heat energy, E_{lh} (GJ y^{-1} per house) associated with condensing water in the air stream. We use the technique of Byrne et al. (1986) to estimate this energy demand

$$E_{lh} = \frac{(Q - Q_0)\rho N_{LHD}}{\eta_c}\left(\frac{8.64 \times 10^4 \text{ s}}{\text{day}}\right)\left(\frac{\text{GJ}}{10^9 \text{ J}}\right) \tag{2.5}$$

where N_{LHD} is the number of latent enthalpy-days (J d kg^{-1} y^{-1}). Huang et al. (1986) tabulate the number of latent enthalpy-days and the number of cooling degree-days for 45 cities in the U.S. The ratio of the latent-heat to sensible-cooling energy load, R (-), is

$$R = \frac{N_{LHD}}{N_{CDD} c_p} \tag{2.6}$$

We calculate the average value of R for the cities in each region and assume that this average represents conditions throughout the region. For example, in the Northeast, the latent-heat energy adds 13% to the energy requirement based on sensible-cooling load. The largest contribution is in the South, where, on average, the latent-heat load adds 25% to the cooling energy requirements.

Summarizing, the average energy required to cool the increased flow of air generated by the SSD system, E_c (GJ y^{-1} per house), is calculated analogously to E_h (see equation (2.2)). However, E_c also depends on the latent-heat load and the fraction of homes that use their air conditioner on a regular basis:

$$E_c = \frac{(Q - Q_0)\rho c_p N_{CDD}}{\eta_c}(1+R) f_{AC} f_{use} \left(\frac{8.64 \text{x} 10^4 \text{ s}}{\text{day}}\right)\left(\frac{\text{GJ}}{10^9 \text{ J}}\right) \quad (2.7)$$

2.4.6 Fan Energy Requirements

The majority of fans used in SSD systems are either 50 or 90 W. Typically, the 90 W fan is used in existing homes, and a 50 W fan is used in new construction where a sufficient subslab gravel layer has been installed. From conversations with several mitigators and researchers (e.g., Ellis (1994) and Paskarich (1994)), we estimate that 85% of the fans currently being installed are 90 W, and 15% are 50 W; thus the average rated fan power is 84 W. Fans under load draw about 80% of their rated power (Bohac et al., 1991). Therefore, assuming continuous operation, the fan energy required for the average house, E_f (GJ y^{-1} per house), is 2.1 GJ y^{-1} per house.

2.4.7 Fuel Costs

The regional cost of each type of fuel, C_{fuel} (\$ GJ^{-1}), is tabulated in Column 7 of Table 2.3 (EIA, 1993b). The energy cost of wood is approximated by assuming a price of \$100 t^{-1} and an energy content of 15 GJ t^{-1}. Because the fraction of homes that use wood for heat is small, the error introduced by the uncertainty in this price has a negligible effect on the overall energy cost.

2.4.8 *Heating Costs*

The cost to heat the additional ventilation flow for a particular fuel, C_{hi} ($\$ y^{-1}$ per house), is $E_{hi}C_{fuel}$. The cost to heat this flow, C_h ($\$ y^{-1}$ per house), for an average house in each region is

$$C_h = \sum_{fuels} f_i C_{hi} \tag{2.8}$$

2.4.9 *Cooling and Fan Costs*

The cost to cool the additional air flow for an average house, C_c ($\$ y^{-1}$ per house), is the product of E_c and the cost of electricity. The cost to run the SSD system fan, C_f ($\$ y^{-1}$ per house), is the product of E_f and the cost of electricity.

2.4.10 *CO_2 Emissions*

Regional CO_2 emission factors for electricity production are a function of the area's mix of electrical power generating fuels. To account for this, we weight the national average of 186 $kgCO_2\ GJ^{-1}$ (Koomey et al., 1993) by each region's CO_2 emissions, m_{CO_2} (10^3 tCO_2), per electric utility sales, S (GWh) (EIA, 1992). The regional CO_2 emission factor, e_{CO_2} ($kgCO_2\ GJ^{-1}$), is then approximated as

$$e_{CO_2} = (186\ \mathrm{kgCO_2\ GJ^{-1}}) \frac{\left[m_{CO_2} / S \right]_{region}}{\left[m_{CO_2} / S \right]_{national}} \tag{2.9}$$

where the subscripts *region* and *national* refer to the geographical area over which the ratio is taken. The CO_2 emission factors for natural gas, fuel oil, LPG, and kerosene are independent of region (EIA, 1993a). Wood has a net emission factor of 0 if it is harvested sustainably; this is the value we use here.

The mass of CO_2 emitted for a particular heating fuel, M_{hi} ($kgCO_2\ y^{-1}$ per house), is $E_{hi} e_{CO_2}$. The mass of CO_2 emitted from producing the heating energy, M_h ($kgCO_2\ y^{-1}$ per house), is

$$M_h = \sum_{fuels} f_i M_{hi} \tag{2.10}$$

The CO_2 emissions generated as a result of producing the cooling energy, M_c ($kgCO_2\ y^{-1}$ per house), and system fan energy, M_f ($kgCO_2\ y^{-1}$ per house), are $E_c e_{CO_2}$ and $E_f e_{CO_2}$, respectively. In these two expressions, e_{CO_2} is the emission factor for electricity.

2.4.11 Number of Houses Where an SSD System is Applicable

The number of houses in each region with annual-average, living-area indoor radon concentrations greater than 4 $pCi\ l^{-1}$ was estimated by Marcinowski et al. (1994)

(here we assume that the EPA and census regions match). We take the fraction of houses in each region where an SSD system is feasible as the fraction of single-family houses with a basement or slab-on-grade construction. The number of houses in which an SSD system is appropriate, N_H (-), is calculated as the product of the number of houses with indoor concentrations greater than 4 pCi l^{-1} and the fraction of houses with a basement or slab-on-grade construction.

The annual energy required to run all the SSD systems in each region is $N_H(E_h + E_c + E_f)$. The annual cost for this energy is $N_H(C_h + C_c + C_f)$, and the resulting annual CO_2 emissions are $N_H(M_h + M_c + M_f)$. Finally, the energy, cost, and CO_2 emissions for the entire United States are calculated by combining the values from the four regions.

In these computations, we have made the approximation that the type of heating fuel used, radon levels, and substructure type are uncorrelated. To decide whether a more complex analysis was necessary, we examined the radon levels in the National Residential Radon Survey (NRRS) (Lucas et al., 1992) by both house substructure type and type of heating fuel used. We found that the substantive results of performing the analysis with the NRRS data are only slightly different from the results presented here. Most of the discrepancies in estimated energy cost and energy usage are due to the fact that the NRRS suggests a somewhat higher proportion of mitigable homes with high radon concentrations would be electrically heated (and fewer would be gas or oil heated). In no region were the differences between the

results presented here and those using the NRRS data greater than 15 percent. Since use of the NRRS entails its own problems of correcting for small sample sizes (the survey sampled only 125 of about 3,100 counties in the U.S.), a simple analysis based on it would not necessarily be more accurate than the present work.

2.5 Results and Discussion

2.5.1 Regional, Per-House Impacts of SSD System Use

Calculated heating energy impacts and expenditures are summarized in Table 2.3. The energy, E_h (Table 2.3, column 6), required to heat the additional ventilation air ranges from 2.1 GJ y^{-1} per house in the South to 5.8 GJ y^{-1} per house in the Midwest. The cost of supplying this energy, C_h (Table 2.3, column 8), varies from \$19 y^{-1} per house in the South to \$45 y^{-1} per house in the Midwest. The CO_2 emissions associated with this energy generation, M_h (Table 2.3, column 10), range from 160 $kgCO_2$ y^{-1} per house in the South to 370 $kgCO_2$ y^{-1} per house in the Midwest. The per-house heating energy, cost, and associated CO_2 emissions are largest (and comparable) in the Northeast and Midwest.

Calculated cooling energy impacts and expenditures are summarized in Table 2.4. The cooling energy requirements, E_c (Table 2.4, column 7), are much lower than the heating energy requirements. Our estimates range from 0.05 GJ y^{-1} per house in the Northeast to 0.51 GJ y^{-1} per house in the South. The cooling energy requirements are highest in the South where more homes have air conditioners, more of the homes with

air conditioners use them, and the number of cooling-degree days is relatively large. Cooling fuel costs attributable to the SSD system, C_c (Table 2.4, column 8), are relatively small, ranging from \$1 to \$9 y^{-1} per house. CO_2 emissions, M_c (Table 2.4, column 9), are largest in the South, at 90 $kgCO_2$ y^{-1} per house.

The required fan power per house is independent of region. Therefore, the variations in fan operating expense and CO_2 emissions are a function only of regional electricity costs and CO_2 emission factors. Table 2.5 summarizes our calculations. Among regions, the average cost to run the fan, C_f (Table 2.5, column 3), varies from \$38 to \$55 y^{-1} per house, while CO_2 emissions, M_f (Table 2.5, column 4), range from 300 to 540 $kgCO_2$ y^{-1} per house. The emissions generated from producing power for the fan are the largest contributor to CO_2 emissions associated with SSD system operation.

Table 2.6 gives the per-house energy use, expense, and CO_2 emissions associated with SSD system operation. Overall energy requirements range from 4.7 to 7.9 GJ y^{-1} per house. Costs vary from \$66 to \$99 y^{-1} per house. CO_2 emissions range from 500 to 930 $kgCO_2$ y^{-1} per house. The fan consumes, on average, about 40% of the end-use energy used to operate the SSD system. However, because electricity is the most expensive fuel, the fan accounts for about 60% of the annual expense in all four regions.

For comparison, a new, energy efficient refrigerator of moderate size (18 ft^3) consumes about 2.3 GJ y^{-1}. We predict that a SSD system will use about two to three

times this amount of energy; the lower value corresponding to a house in the South or West, and the higher value corresponding to a house in the Midwest or Northeast.

2.5.2 Regional and National Implications

Table 2.7 summarizes our calculations of the regional and national energy demand, cost, and CO_2 emissions associated with SSD system operation at saturation. Here we assume that all houses with a basement or slab-on-grade construction that also have indoor radon concentrations above 4 pCi l^{-1} are mitigated with a SSD system (about 2.6 million houses nationwide). The impacts are largest in the Midwest, where the heating load and the number of mitigable houses are large.

Over the entire U.S., we estimate that, annually, 1.7×10^4 (6.4×10^3 to 3.9×10^4) TJ of end-use energy would be consumed by the SSD systems at a cost of about $230 ($130 to $400) million. In addition, about 2.0×10^9 (1.2×10^9 to 3.5×10^9) $kgCO_2$ per year would be emitted as a result of producing this energy. The ranges presented here reflect estimated uncertainty in the increased house ventilation rate caused by the SSD system.

For perspective, the energy consumed nationally by the SSD systems at saturation would be approximately equal to the energy consumed by 230,000 cars. The national CO_2 emissions associated with SSD system operation would be equivalent to the CO_2 emissions of 350,000 cars (EIA, 1994).

2.6 Conclusions

Individual SSD system operating costs vary, by region, between $66 and $99 per year. The higher cost corresponds to a house in the Northeast or Midwest, and the lower cost to a house in the South or West. By combining data of the distribution of indoor radon concentrations and house substructure types, we estimate a national annual cost of $230 ($130 to $400) million at saturation. This cost is associated with an annual national energy demand of 1.7×10^4 (6.4×10^3 to 3.9×10^4) TJ, and 2.0×10^9 (1.2×10^9 to 3.5×10^9) kg of CO_2 emissions. Because of its relatively high heating load and large number of mitigable houses, the impacts of SSD use are largest in the Midwest. Improving our estimate of the SSD-induced house ventilation could substantially decrease the uncertainty in these predictions.

Very little research has been conducted to optimize the energy efficiency of SSD systems. Saum (1991) and Fisk et al. (1995) have reported satisfactory performance with a 10 W system fan for some new houses. Passive, or energy-efficient systems (Saum and Osborne, 1990; Fisk et al., 1995), offer opportunities to drastically reduce the fan energy required by SSD systems. We expect these techniques will also have a much smaller impact on house ventilation, thereby largely avoiding the heating and cooling expenses associated with SSD system use. Further research should be aimed at defining the possible energy savings, the relative effectiveness for reducing indoor concentrations, and the applicability of these low-energy mitigation techniques.

Acknowledgments-This work was supported by the Assistant Secretary for Energy Efficiency and Renewable Energy, Office of Building Technologies, Building Systems and Materials Division of the U.S. Department of Energy (DOE) under contract no. DE-AC03-76SF00098. The authors wish to thank Phil Price for his help in analyzing the NRRS data and reviewing the manuscript, Barbara Litt for her help in navigating the RECS database, and Jonathon Koomey and David Faulkner for reviewing the manuscript.

2.7 References

ASHRAE (1993) 1993 ASHRAE Handbook: Fundamentals, American Society of Heating, Refrigerating, and Air Conditioning Engineers, Atlanta, GA.

Boghosian S. H. (1994) Personal communication, Lawrence Berkeley National Laboratory, Berkeley, CA.

Bohac D. L., Dunsworth T. S., Shen L. S., and Damm C. J. (1991) The energy penalty of sub-slab depressurization radon mitigation systems, Vol 4, VII-3, report EPA/600/9-90-005, Proc. of 1991 International Symposdium on Radon and Radon Reduction Technology, Philadelphia, PA, USEPA Research Laboratory, Research Triangle Park, NC.

Bohac D. L., Shen L. S., Dunsworth T. S., and Hancock M. W. (1993) *Radon mitigation energy cost penalty research project, year 2,* Minnesota Building Research Center, Univ. of Minnesota, Minneapolis, MN.

Bonnefous Y. C., Gadgil A. J., and Fisk W. J. (1994) Impact of subslab ventilation technique on residential ventilation rate and energy costs, *Energy Build.* **21**, 15-24.

Byrne S. J., Huang Y. J., Ritschard R. L., and Foley D. M. (1986) The impact of wind induced ventilation on residential cooling load and human comfort, report LBL - 20919, Lawrence Berkeley National Laboratory, Berkeley, CA.

Clarkin M., Brennan T., and Osborne M. C. (1990) Energy penalties associated with the use of a sub-slab depressurization system, Vol. IV, paper D-VIII-1, report EPA/600/9-90-005d, Proc. of 1990 International Symposium on Radon and Radon

Reduction Technology, Atlanta, GA, USEPA, Research Laboratory, Research Triangle Park, NC.

EIA (1992) Electric power annual, 1990, report DOE/EIA-0348(90), Energy Information Administration, Washington, DC.

EIA (1993a) Emissions of greenhouse gases in the United States, 1985-1990, report DOE/EIA-0573(91), Energy Information Administration, Washington, DC.

EIA (1993b) State energy price and expenditure report, 1991, report DOE/EIA-0376(91), Energy Information Administration, Washington, DC.

EIA (1994) Monthly energy review: February 1994, report DOE/EIA-0035 (94/02), Energy Information Administration, Washington, DC.

Ellis L. (1994) Personal Communication, FanTech, Sarasota, Fl.

EPA (1994) Model standards and techniques for control of radon in new residential buildings, *Federal Register Notices* **59**, 13402-13416.

Ericson S.-O. and Schmied H. (1987) Modified design in new construction prevents infiltration of soil gas that carries radon, In Hopke P. K. (Ed.) *Radon and its Decay Products*, American Chemical Society, Washington, D.C., 526-535.

Ericson S.-O., Schmied H., and B. Clavensjo B. (1984) Modified technology in new construction, and cost effective remedial action in existing structures, to prevent infiltration of soil gas carrying radon, *Radiation Protection Dosimetry* **7**, 223-226.

Fisk W. J., Prill R. J., Wooley J., Bonnefous Y. C., Gadgil A. J., and Riley W. J. (1995) New methods of energy efficient radon mitigation, *Health Phys.* **68**, 689-698.

GRI (1993) Baseline projection data book - GRI baseline projection of U.S. Energy supply and demand to 2010, Gas Research Institute, Washington, DC.

Hanford J. W., Koomey J. G., Stewart L. E., Lecar M. E., Brown R. E., Johnson F. X., Huang R. J., and Price L. K. (1994) Baseline data for the residential sector and development of a residential forecasting database, report LBL-33717, Lawrence Berkeley National Laboratory, Berkeley, CA.

Henschel D. B. (1991) Cost analysis of soil depressurization techniques for indoor radon reduction, *Indoor Air* **3**, 337-351.

Huang Y. J., Ritschard R., Bull J., and Chang L. (1986) Climate indicators for estimating residential heating and cooling loads, report LBL-21101, Lawrence Berkeley National Laboratory, Berkeley, CA.

Koomey J. G., Johnson F. X., McMahon J. E., Orland M. C., Levine M. D., Chan P., and Krause F. (1993) An assessment of future energy use and carbon emissions from U.S. residences, report LBL-32183, Lawrence Berkeley National Laboratory, Berkeley, CA.

Lucas R. M., Grillo R. B., Perez-Michael A., and Kemp S. S. (1992) National residential radon survey statistical analysis, Volume 2, Summary of the questionnaire data, report RTI/5158/49-2F, USEPA, Research Triangle Park, NC.

Marcinowski F., Lucas R. M., and Yeager W. M. (1994) National and regional distributions of airborne radon concentrations in United States homes, *Health Phys.* **66**, 699-706.

Modera M. (1993) Characterizing the performance of residential air distribution systems, *Energy Build.* **20**, 65-75.

Pandian M. D., Ott W. R., and Behar J. V. (1993) Residential air exchange rates for use in indoor air and exposure modeling studies, *Journal of Exposure Analysis and Environmental Epidemiology* **3**, 407-415.

Paskarich J. (1994) Personal communication, Safe Air, Moline, Il.

RECS (1992) Residential Energy Consumption Survey, Housing Characteristics 1990, report DOE/EIA-0314(90), Energy Information Administration, Washington, DC.

Sanchez D. C. (1987) A review of the Canadian and Swedish experience for the control of indoor radon, Proc. of Proceedings of the Second APCA International Specialty Conference, Indoor Air II, Cherry Hill, NJ, Air Pollution Control Association.

Saum D. W. (1991) Mini fan for SSD radon mitigation in new construction, Proc. of International Symposium on Radon and Radon Reduction Technology, Philadelphia, PA, USEPA, Research Laboratory, Research Triangle Park, NC.

Saum D. W. and Osborne M. C. (1990) Radon mitigation performance of passive stacks in residential new construction, Proc. of 1990 International Symposium on

Radon and Radon Reduction Technology, Atlanta, GA, USEPA, Research Laboratory, Research Triangle Park, NC.

Sherman M. H. (1980) Air Infiltration in Buildings, report LBL-10712, Lawrence Berkeley National Laboratory, Berkeley, CA.

Treidler B. and Modera M. (1994) Thermal performance of residential duct systems in basements, report LBL-33962, Lawrence Berkeley National Laboratory, Berkeley, CA.

Turk B. H., Harrison J., and Sextro R. G. (1991) Performance of radon control systems, *Energy Build.* **17**, 157-175.

Turk B. H., Prill R. J., Grimsrud D. T., Moed B. A., and Sextro R. G. (1987) Radon and remedial action in Spokane Valley homes, volume I: Experimental design and data analysis, report LBL-23430, Lawrence Berkeley National Laboratory, Berkeley, CA.

Table 2.1. Placement of the states into the four Census Regions.

Census Region	*States*	*EPA regions*
Northeast	Connecticut, Maine, Massachusetts, New Hampshire, Vermont, Rhode Island, New Jersey, New York, Pennsylvania	1, 2
Midwest	Illinois, Indiana, Michigan, Ohio, Wisconsin, Iowa, Kansas, Minnesota, Missouri, Nebraska, North Dakota, South Dakota	5, 7
South	Delaware, the District of Columbia, Florida, Georgia, Maryland, North Carolina, South Carolina, Virginia, West Virginia, Alabama, Kentucky, Mississippi, Tennessee, Arkansas, Louisiana, Oklahoma, Texas	3, 4, 6
West	Arizona, Colorado, Idaho, Montana, Nevada, New Mexico, Utah, Wyoming, Alaska, California, Hawaii, Oregon, Washington	8, 9, 10

Table 2.2. Additional house ventilation rate generated by an SSD system, grouped by study.

Study	*Increase in ventilation*[a] *($m^3\ s^{-1}$)*
Turk et al. (1987)	-9.0E-03
	1.3E-02
	1.3E-02
	-9.7E-03
	1.7E-02
	7.6E-03
	4.2E-03
Turk et al. (1991)	1.3E-02
	1.5E-02
	1.9E-02
	6.9E-02
	1.0E-02
Clarkin et al. (1990)	1.8E-03
	2.0E-04
	1.5E-05
Bohac et al. (1993)	2.3E-04
	3.9E-04
	2.9E-03
	5.8E-03
	5.0E-03

[a]In the Turk et al. studies the increase was directly measured. For the Clarkin et al. and Bohac et al. studies the increase was estimated from equation (2.1).

c:/thesis/tab2_2.xls

Table 2.3. Energy requirements, expense, and CO_2 emissions associated with heating the additional ventilation air.

Column:	*2*	*3*	*4*	*5*	*6*	*7*	*8*	*9*	*10*
fuel type	*Region*	*Fractional use*[1] *(-)*	*Number of Heating Degree Days*[2] *(°C d y^{-1})*	*Total Efficiency*[3]	*Energy (GJ y^{-1} per house)*	*Fuel cost*[4] *($ GJ^{-1})*	*Cost ($ y^{-1} per house)*	*Emission Factor*[5,6,7] *(kgCO$_2$ GJ^{-1})*	*CO$_2$ production (kgCO$_2$ y^{-1} per house)*
		f_i	N_{HDD}	η_h	E_{hi} and E_h	C_{fuel}	C_{hi} and C_h	e_{CO_2}	M_{hi} and M_h
natural gas	NE	0.46	2747	0.51	5.0	6.80	34	50.5	250
electricity	NE	0.10	2885	0.75	3.6	26.10	93	157	560
fuel oil	NE	0.39	2860	0.51	5.2	7.30	38	69.4	360
wood	NE	0.03	3728	0.30	11.5	6.70	77	0.0	0
lpg	NE	0.01	3225	0.51	5.9	12.90	76	60.0	350
kerosene	NE	0.02	3706	0.70	4.9	8.30	41	67.7	330
Average	NE				**5.1**		**43**		**320**
natural gas	S	0.44	1407	0.51	2.6	5.50	14	50.5	130
electricity	S	0.38	1003	0.75	1.2	18.30	23	178	220
fuel oil	S	0.05	1750	0.51	3.2	6.70	21	69.4	220
wood	S	0.04	1600	0.30	4.9	6.70	33	0.0	0
lpg	S	0.07	1224	0.51	2.2	9.20	20	60.0	130
kerosene	S	0.02	1369	0.70	1.8	7.70	14	67.7	120
Average	S				**2.1**		**19**		**160**
natural gas	MW	0.72	3175	0.51	5.8	5.80	33	50.5	290
electricity	MW	0.11	3012	0.75	3.7	24.10	90	259	960
fuel oil	MW	0.05	3558	0.51	6.5	7.00	45	69.4	450
wood	MW	0.04	3429	0.30	10.6	6.70	71	0.0	0
lpg	MW	0.07	3311	0.51	6.0	12.10	73	60.0	360
kerosene	MW	0.00	0	0.70	0.0	7.90	0	67.7	0
Average	MW				**5.8**		**45**		**370**
natural gas	W	0.64	1652	0.51	3.0	5.50	16	50.5	150
electricity	W	0.24	2085	0.75	2.6	18.30	47	141	360
fuel oil	W	0.00	2601	0.51	4.7	6.50	31	69.4	330
wood	W	0.06	2911	0.30	9.0	6.70	60	0.0	0
lpg	W	0.02	2341	0.51	4.2	9.60	41	60.0	250
kerosene	W	0.00	0	0.70	0.0	7.70	0	67.7	0
Average	W				**3.2**		**26**		**190**

[1] RECS (1992), Table 20, pg. 62.
[2] RECS (1992), Table 55, pg. 185.
[3] See equation (2.3) of text.
[4] EIA (1993a), pg. 19-174.
[5] EIA (1993b), Table 11, pg. 15.
[6] Koomey et al., (1993), Table A.4, pg. 21.
[7] EIA (1992), Tables 43 and 45.

Table 2.4. Energy requirements, expense, and CO_2 emissions associated with cooling the additional ventilation air.

Column:	*2*	*3*	*4*	*5*	*6*	*7*	*8*	*9*
Region	*Fraction of single family homes with air conditioning*[1] f_{AC}	*Fraction of households with air conditioning that use it*[2] f_{use}	*Number of Cooling Degree Days*[2] *(°C d y^{-1})* N_{CDD}	*Efficiency of air conditioner* and distribution *system* η_c	*Latent enthalpy ratio (-)* R	*Energy (GJ y^{-1} per house)* E_c	*Cost ($ y^{-1} per house)* C_c	*CO_2 production (kgCO_2 y^{-1} per house)* M_c
NE	0.56	0.36	421	1.78	0.13	0.05	1	7.7
S	0.87	0.77	1159	1.78	0.25	0.51	9	90
MW	0.73	0.42	481	1.78	0.15	0.09	2	23
W	0.40	0.50	767	1.78	0.01	0.08	1	11

[1] RECS (1992), Table 11, pg. 38 and Table 54, pg. 180.
[2] RECS (1992), Table 54, pg. 180.
[3] EIA (1993a), pg. 19-174.
[4] EIA (1993b), Table 11, pg 15.
[5] Koomey et al., (1993), Table A.4, pg. 21.

Table 2.5. Energy requirements, expense, and CO_2 emissions associated wtih running the system fan.

Column:	*2*	*3*	*3*	*4*
Region	*Energy* ($GJ\ y^{-1}$ *per house)* E_f	*Fuel cost*[1] ($\$\ GJ^{-1}$)	*Cost* ($\$\ y^{-1}$ *per house)* C_f	CO_2 *production* ($kgCO_2\ y^{-1}$ *per house)* M_f
NE	2.1	26.10	55	330
S	2.1	18.40	39	370
MW	2.1	24.10	51	540
W	2.1	18.30	38	300

Table 2.6. Regional per-house energy use, expense, and CO_2 emissions associated with SSD system use.

Region	*Energy* ($GJ\ y^{-1}$ *per house)*	*Cost* ($\$\ y^{-1}$ *per house)*	CO_2 *production* ($kgCO_2\ y^{-1}$ *per house)*
NE	7.2	99	660
S	4.7	67	620
MW	7.9	97	930
W	5.3	66	500

Table 2.7. Total regional and national energy requirements, expense, and CO_2 emissions associated with SSD system use.

Column:	*2*	*3*	*4*	*5*	*6*	*7*
Region	*# of houses[1] with indoor concentrations > 4 pCi l^{-1}*	*% of houses with a basement or slab-on-grade[2]*	*# of houses that are subject to SSV mitigation N_H*	*Total energy (TJ y^{-1}) (Fan + Ventilation)*	*Total cost (M$ y^{-1}) (Fan + Ventilation)*	*Total CO_2 ($kgCO_2$ y^{-1}) (Fan + Ventilation)*
NE	5.94E+05	54	3.19E+05	2.3E+03	32	2.1E+08
S	1.92E+06	37	7.03E+05	3.3E+03	47	4.4E+08
MW	2.46E+06	52	1.29E+06	1.0E+04	130	1.2E+09
W	7.46E+05	39	2.92E+05	1.6E+03	19	1.5E+08
U.S.	5.72E+06		2.60E+06	1.7E+04	230	2.0E+09

[1] Marcinowski et al., (1994), Table 8, pg. 705.

[2] RECS (1992).

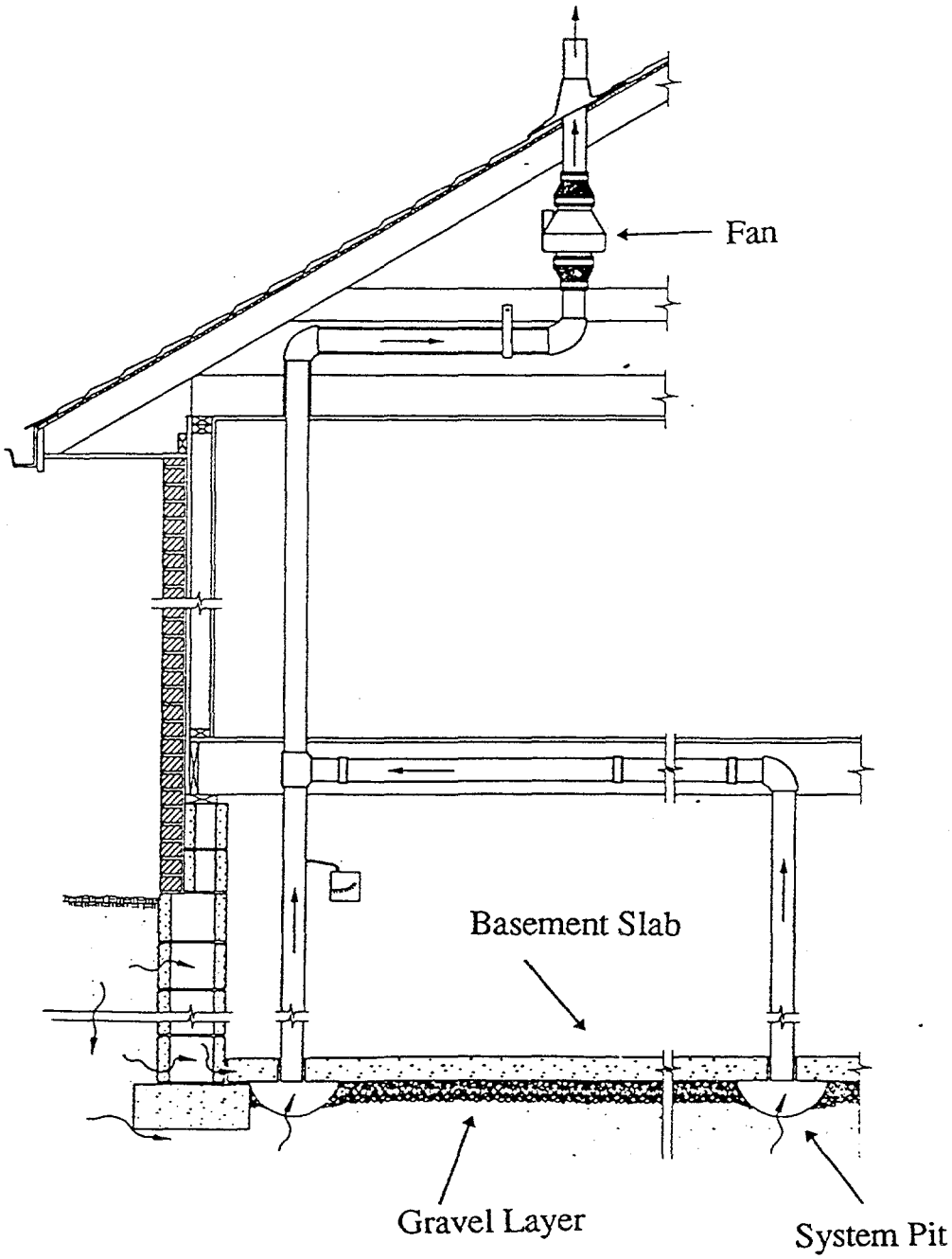

Figure 2.1. Schematic of an SSD system (EPA, 1994). The system fan draws radon-bearing soil gas from the pit and exhausts it to the outdoors.

CHAPTER 3

WIND-INDUCED GROUND-SURFACE PRESSURES AROUND A SINGLE-FAMILY HOUSE*

3.1 Abstract

Wind induces a ground-surface pressure field around a building that can substantially affect the flow of soil gas and thereby the entry of radon and other soil-gas contaminants into the building. To quantify the effect of the wind-induced ground-surface pressure field on contaminant entry rates, the time-averaged ground-surface pressure field was experimentally measured in a wind tunnel for several incidence angles of the wind, two atmospheric boundary layers, and two house geometries. The experimentally measured ground-surface pressure fields are compared with those predicted by a k-ε turbulence model. Despite the fundamental limitations in applying a k-ε model to a system with flow separation, predictions from the numerical simulations were good for the two wind incidence angles tested. The ground-surface pressure

---

* This chapter is based on a paper: Riley, W. J., A. J. Gadgil, and W. W. Nazaroff (1996) Wind-induced ground-surface pressures around a single-family house, accepted for publication in *The Journal of Wind Engineering and Industrial Aerodynamics*.

fields measured in the wind tunnel and presented in this chapter are used as input to the modeling studies described in Chapters 4 and 7.

3.2 Nomenclature

$c_p(x,y)$	mean ground-surface pressure coefficient at (x,y) (-)
$c_p\|_{\mathrm{F}}(x,y)$	mean ground-surface pressure coefficient at (x,y), from FLUENT (-)
$c_p\|_{\mathrm{W}}(x,y)$	mean ground-surface pressure coefficient at(x,y), from the wind tunnel (-)
d	displacement height (m)
$E(x,y)$	error in predicted pressure coefficient at (x,y) (-)
$I(z)$	turbulence intensity (-)
k	turbulent kinetic energy per unit mass of fluid ($m^2 s^{-2}$)
$p_{gs}(x,y)$	mean ground-surface pressure at (x,y) (Pa)
p_∞	free stream pressure (Pa)
$U(z)$	mean wind speed at height z ($m s^{-1}$)
U_{ref}	mean wind speed at stationary reference pitot tube ($m s^{-1}$)
u_*	friction velocity ($m s^{-1}$)
V_{eh}	mean wind speed at eave height ($m s^{-1}$)
(x,y)	ground-surface coordinates (m)
z_0	roughness length (m)
z	height above the ground surface (m)

Greek letters

ε	rate of dissipation of turbulent kinetic energy per unit fluid mass ($m^2\ s^{-3}$)
κ	von Karman's constant (0.4)
ρ	air density ($kg\ m^{-3}$)
$\sigma(z)$	standard deviation of $U(z)$ at height z ($m\ s^{-1}$)
τ_0	shear stress at the ground surface ($kg\ m^{-1}\ s^{-2}$)

Note: (-) indicates a nondimensional variable.

3.3 Introduction

The work presented in this chapter is aimed at developing a better understanding of the soil-gas transport and entry into houses of radon and volatile organic compounds (VOCs). In this context, wind is of interest because its interaction with the building structure and nearby soil surface can significantly affect soil-gas movement around and into a house.

Substantial research effort is being applied to develop models that characterize the environmental and building factors affecting indoor contaminant concentrations. The understanding gained from these models can be used to determine which parts of the population are at risk, to decide where resources should be spent, and to design efficient and effective mitigation systems.

The effects of wind on a building's overall ventilation rate and relative depressurization with respect to outdoor air have been thoroughly studied (Feustel and Sherman, 1989; Ernest, 1991; Sherman, 1992). However, the wind-induced ground-surface pressure field has largely been ignored in models of contaminant entry into houses (Gadgil, 1992). Several authors have presented empirical evidence indicating that this pressure field may be significant when determining radon entry rates (Nazaroff et al., 1985; Turk et al., 1990). In Chapter 4, the wind-tunnel data reported here are used as input to a three-dimensional numerical model of soil-gas and radon transport. We demonstrate that ignoring the wind-induced ground-surface pressure field can lead to large errors in predicted soil-gas and radon entry rates, especially in high-permeability soils.

Other authors have published wind-tunnel studies of flow around bluff bodies that include measurement of the ground-surface pressure distribution. Sakamoto and Mikio (1982) examined the flow around a cube in a turbulent boundary layer and presented contour plots of the pressure distribution on the ground surface. Unfortunately for the present purposes, the results correspond to cube heights that are relatively large compared to the boundary layer thickness, and therefore do not correspond to the case of a building immersed in the atmospheric boundary layer. The lowest ratio of cube height to boundary layer thickness for which Sakamoto and Mikio report results is 0.4, whereas typical values for the ratio of house height to boundary layer depth are less than 0.1. Surry (1991) and Okada and Ha (1992) present the ground-surface pressure coefficient at several positions around a test building at Texas Tech University. The spatial coverage of these measurements, however, is insufficient for our purposes. Levitan (1993) has performed a wind-tunnel study and measurements of the ground-surface pressure field around this same building. Although the building geometry is somewhat different than ours, the ground-surface pressure fields he reports are qualitatively similar to those we present here.

DSMA Atcon Ltd. (1985) reported results, generated in a small wind tunnel, of the mean ground-surface pressure distribution around a single-family home. This information was then used to predict radon entry rates into a house during a summer and winter period in Toronto. In this paper we extend Scott's work by more carefully controlling the experimental conditions and investigating the feasibility of replacing the wind-tunnel experiments with numerical simulations.

Because wind-tunnel experiments are relatively expensive, numerical simulation of air flow around buildings has begun to receive considerable attention. There are many simulation techniques, broadly distinguished by their treatment of turbulence, for modeling these flows. The simplest numerical simulation techniques applicable to the present problem are based on the k-ε turbulence model. In this model, the eddy viscosity is linked to the turbulent kinetic energy per unit fluid mass, k ($m^2 s^{-2}$), and the rate of dissipation of turbulent kinetic energy per unit fluid mass, ε ($m^2 s^{-3}$). The details of the k-ε model are thoroughly documented elsewhere (e.g., Anderson et al. (1984)).

Generally, the k-ε modeling approach encounters difficulty predicting the flow separation that occurs in the vicinity of bluff bodies. Murakami (1993) attributes this failure to an overestimate of the turbulent kinetic energy in the region of separation, which leads to an overestimate of the eddy viscosity. Nevertheless, the k-ε turbulence model has been used extensively to simulate the flow around buildings immersed in turbulent boundary layers. Patterson and Apelt (1990) report very good agreement with experimental results for mean pressures in the vicinity of a cube. Stathopoulos and Zhou (1993) studied wind flow around an L-shaped building. They concluded that their simulation results provided good prediction of building surface pressures, except at areas near the building edges when the wind incidence is oblique. In a full-scale building experiment, Hoxey and Richards (1993) report a number of differences between the experimental measurements and model predictions of the pressure field, especially in regions of separated flow. However, they state that the overall structure

of the pressure distribution is well described by the model. Zhang et al. (1993) studied a cubic building and report that the computed mean velocity fields show good agreement with wind-tunnel measurements; no results were presented for the pressure field around the body.

Current state-of-the-art techniques, such as large eddy simulations, are designed to predict the complex wind flows around buildings more accurately. The increase in accuracy possible with these models comes at the expense of a large increase in computation time (Ferziger, 1993; Murakami, 1993). One goal of the present work, together with that reported in Chapter 4, is to test whether the relatively inexpensive k-ε turbulence model can provide sufficiently accurate ground-surface pressure fields for the simulation of soil-gas contaminant transport around houses.

3.4 Materials and Methods

3.4.1 Boundary Layer Wind Tunnel

The experiments were performed in the boundary-layer wind tunnel of the Department of Architecture at the University of California, Berkeley. A detailed description of the wind tunnel can be found in Bauman et al. (1988). The test area has a cross section of 1.5 m high by 2.1 m wide, and the house model can be oriented at any angle to the incident wind by means of a turntable. A scale of 1:61 was used for the experiments; however, all dimensions reported here will be full-scale values. Three pressure transducers were used to measure the distribution of mean ground-surface

pressures around the model building and the free stream dynamic and static pressures. The wind speed was measured with a hot-wire anemometer at 60 heights in the boundary layer. At each height, 30 readings per second were taken for 30 seconds. The mean and standard deviation of the wind speed were calculated from these data.

For an adiabatic atmosphere, and for the flow through the wind tunnel, the horizontal wind speed in the vicinity of the ground surface is often represented by a logarithmic profile (Seinfeld, 1986)

$$U(z) = \frac{u_*}{\kappa} \ln\left(\frac{z - d}{z_0}\right) \tag{3.1}$$

where $U(z)$ is the mean horizontal wind speed (m s^{-1}) at height z (m), u_* is the friction velocity (m s^{-1}), κ is von Karman's constant (0.4), z_0 is the roughness length (m), and d is the displacement height (m). The displacement height is the distance above the ground surface where $U(z)$ begins to follow the logarithmic profile. It is typically less than the average height of the surrounding buildings, and is taken to be zero for smooth surfaces. The friction velocity, u_*, is defined as $\sqrt{\frac{\tau_0}{\rho}}$, where τ_0 is the shear stress at the ground surface (kg m^{-1} s^{-2}) and ρ is the air density (kg m^{-3}).

The turbulence intensity, $I(z)$ (-), indicates the size of the velocity fluctuations with respect to the mean velocity

$$I(z) = \frac{\sigma(z)}{U(z)} \tag{3.2}$$

where $\sigma(z)$ is the standard deviation associated with temporal fluctuations of $U(z)$.

Experiments were performed for two different atmospheric boundary layers. The first had a roughness length of 0.1 m and a displacement height of 0 m (referred to hereafter as the "countryside" boundary layer), corresponding to the outskirts of a small town or a countryside with many hedges, some trees, and some buildings (ESDU, 1985). The second had a roughness length of 0.29 m and a displacement height of 6 m (referred to hereafter as the "suburban" boundary layer), corresponding to the suburbs of a large town or the interior of a small town. These values were chosen to bound the range of expected conditions around most single family homes. The boundary layers are established in the wind tunnel by placing blocks on the floor upwind of the house model.

Figures 3.1 and 3.2 show the experimental and analytical profiles of horizontal wind speed and turbulence intensity for these two boundary layers. The analytical horizontal wind speed profile is fit to equation (3.1) using friction velocities that are averages over the boundary layer depth: 0.35 m s^{-1} for the countryside boundary layer, and 0.48 m s^{-1} for the suburban boundary layer. The turbulence intensity profile is from ESDU (1985).

3.4.2 Model Geometry and Pressure Measurement

The house geometry used in the wind-tunnel experiment was chosen to represent a typical single-family structure in size and aspect ratio. The building has a plan area of 8.7 m x 10.4 m, a height of 3 m, a 6:12 roof pitch (rise:run), and an eave overhang of 30 cm (Figure 3.3). The model blocks only 0.2% of the wind-tunnel cross section. Separate experiments were performed with a gable roof and a flat roof to determine the effect of roof geometry on the ground-surface pressure field. The permeability of a building's walls (e.g., open windows) was not included in either our wind-tunnel or numerical modeling experiments. We expect that the error introduced by this simplification is small.

The data acquisition system in the wind tunnel can record pressure measurements at 66 discrete points without interrupting the experiment. The complete pressure field was determined by recording 66 values on half of the ground surface and then rotating the house 180° and recording another 66 values. Thus, mean ground-surface pressures were determined at 132 points around the house for each case. Figure 3.4 shows the locations of the ground-surface pressure measurements. Experiments were run at eight wind angles (every 45°) for each boundary layer and house geometry. By taking advantage of symmetry, the data were combined into results for three incident wind angles: 0° (perpendicular to the short side of the house), 45°, and 90° (perpendicular to the long side of the house).

Pressures were read 30 times per second for 30 seconds at each tap location; the mean and standard deviation of the values were recorded. A delay of 15 seconds between measurements at successive pressure taps was imposed to dampen any fluctuations caused by switching between taps. The pressure transducers were calibrated using a manual micromanometer.

The mean ground-surface pressures were normalized with respect to the eave-height free-stream dynamic pressure to give the mean ground-surface pressure coefficient, $c_p(x,y)$

$$c_p(x,y) = \frac{p_{gs}(x,y) - p_\infty}{\frac{1}{2}\rho V_{eh}^{\ 2}} \tag{3.3}$$

where $p_{gs}(x,y)$ is the mean ground-surface pressure (Pa) at location (x,y), p_∞ is the mean free stream pressure (Pa), ρ is the air density (kg m^{-3}), and V_{eh} is the mean wind speed at eave height (m s^{-1}). Castro and Robins (1977) have shown that the pressure coefficient field remains constant for wind speeds greater than about 0.5 m s^{-1}.

3.4.3 Numerical Simulations

FLUENT is a commercially available software package that models a wide range of fluid flow phenomena by solving the conservation equations for mass and momentum (FLUENT, 1993). A control-volume based, finite-difference method is used to discretize the equations, and we chose the k-ε model to simulate turbulence.

The SIMPLEC algorithm, developed by Patankar (1980), provides the iteration framework used to converge to a solution of the pressure and velocity fields.

The above-ground portion of the one-story house is modeled as a rectangular prism with horizontal dimensions of 10.4 m × 8.7 m and a height of 3 m. The physical space is discretized into 100,000 control volumes using the software's automatic grid generator. There is open space a distance of six house dimensions from the building in both horizontal directions, and the vertical dimension is 61 m. This geometry was chosen to minimize impacts of the numerical space boundaries on the predicted flow over the building. The ground is modeled as a smooth surface. We have assumed that the house is isolated from other buildings and that the flow profile at the inlet to the space corresponds to the "countryside" boundary layer. Default values for the parameters in the k-ε turbulence model are used. FLUENT computes pressure and velocity data at each of the node points in the numerical space. We report normalized mean ground-surface pressures (see equation (3.3)).

3.5 Results and Discussion

3.5.1 Experimental Wind-tunnel Results

Contour plots of experimentally measured mean ground-surface pressure coefficients are presented in Figures 3.5 and 3.6. We used the Tecplot (Amtec Engineering, 1993) software package to generate these contour plots from the discrete data. Figure 3.5 shows the mean ground-surface pressure coefficient fields for the

"countryside" boundary layer. Figure 3.6 shows the analogous information for the "suburban" boundary layer. The pressure coefficient fields are remarkably similar, although the flow is perturbed by the building slightly less in the "countryside" boundary layer. As a result, equivalent contour lines are closer to the building for this case, particularly in the immediate vicinity of the house. Patterson and Apelt (1990), in their numerical study of flow past a cube, reached a similar conclusion regarding the pressures near the ground when the boundary layer is altered. Their results, though, showed more influence of the boundary layer structure than do ours.

The effect of the roof geometry on the pressure field is illustrated by comparing the results in the left and right columns of Figures 3.5 or 3.6. As expected, the building with the gable roof causes a larger perturbation of the flow and extension of the ground-surface pressure field. Changing from the gable roof to the flat roof has a larger effect on the pressure field than changing the atmospheric boundary layer. A steeper roof, or protuberances on the house, would also change the ground-surface pressures. These factors probably would have as large an influence on the ground-surface pressure field as the structure of the boundary layer.

To put our results in perspective, we note that a pressure difference of a few pascals between the basement and soil surface is often sufficient to draw significant amounts of soil gas into the house (Nazaroff, 1992). Figures 3.5 and 3.6 indicate that pressure coefficients ranging from about 0.4 to 1 are present on the ground surface near the building. The 50^{th} and 95^{th} percentile eave height wind speeds over a period of 25 years in Spokane, Washington, are 3.6 and 8.3 m s^{-1}, respectively (NOAA, 1980).

We chose Spokane for this illustration because radon entry and mitigation have been investigated in several houses in the area (Turk et al., 1990). For a 3.6 m s^{-1} wind the corresponding mean ground-surface pressures range from about 3.1 to 7.8 Pa; at 8.3 m s^{-1}, the range is about 17 to 41 Pa. These pressures are large in the context of soil-gas transport. The wind-induced ground-surface pressure field is therefore expected to be a significant factor influencing contaminant entry into houses.

3.5.2 Numerical Simulation Results

The mean ground-surface pressure coefficients calculated by FLUENT for wind incidence angles of 0° and 45° are shown in Figure 3.7. Figure 3.7 (a) corresponds to the same boundary layer and house geometry as the wind-tunnel results in Figure 3.5 (e), and Figure 3.7 (b) corresponds to Figure 3.5 (f).

3.5.3 *Comparison Between Wind-tunnel and Simulation Results*

We define the modeling error, $E(x,y)$, as the difference between the predicted pressure coefficients from FLUENT and the wind tunnel measurements

$$E(x,y) = c_p\big|_F(x,y) - c_p\big|_W(x,y) \tag{3.4}$$

where $c_p\big|_F(x,y)$ is the mean pressure coefficient at the ground-surface location (x,y) calculated by FLUENT (-), and $c_p\big|_W(x,y)$ is the mean pressure coefficient at (x,y) determined in the wind tunnel (-). Figure 3.8 shows a plot of the error for the cases

presented in Figures 3.5 (f) and 3.7 (b): wind from the "countryside" boundary layer incident perpendicular to the short side of the house with a flat roof. The errors are similar when the wind is incident at 45° to the house.

The FLUENT predictions are fairly accurate at the front and rear of the house. Directly behind the house the simulation pressure coefficients are more negative than the corresponding experimental values. This feature reverses at about 2 m behind the house, where the numerical predictions are less negative than the experimental values. The experimental pressure field extends further from the sides of the building than the simulated pressure field. A similar observation was made by Hoxey and Richards (1993) in their numerical simulations of a full-scale experiment. The worst agreement between our simulated and observed pressure coefficients occurs towards the upwind edge of either side of the house. This is the region near the ground surface where the flow separates from the building, a feature the k-ε turbulence model often fails to accurately capture. Figure 3.9 is a histogram showing the distribution of errors in the pressure coefficient, $E(x, y)$, for the same boundary layer and house geometry as in Figure 3.8. The mean and standard deviation of these errors are 0.12 and 0.12, respectively. The distribution of errors for wind incident at 45° to the house is similar to that shown in Figure 3.9.

3.6 Conclusions

We have performed wind-tunnel experiments to determine the mean ground-surface pressure field established around a single-family house in the presence of wind.

Two atmospheric boundary layers and two house geometries were studied. The mean ground-surface pressure fields determined in the wind-tunnel experiment were compared to predictions from a k-ε turbulence model simulation. Although the k-ε model has fundamental limitations simulating systems with flow separation, predictions from the numerical simulations were good for the two wind incidence angles tested (0° and 45°).

Our numerical simulations of the flow of soil gas around a building (Chapter 4) indicate that radon entry rates are relatively insensitive to errors in the ground-surface pressure field that are on the order of those presented in Figure 3.8. We therefore conclude that, for a simple house geometry, the k-ε turbulence model predicts mean ground-surface pressure fields that are sufficiently accurate to study the steady-state transport of soil gas and radon in the presence of steady wind. Because the wind-induced ground-surface pressures influence soil-gas contaminant entry to a large extent, transient winds and more complicated geometries (e.g., multiple houses and multi-story buildings) continue to be of research interest.

Acknowledgments- The authors wish to thank Adil Sharag-Eldin for his help with the wind-tunnel experiments, Fred Bauman for helpful conversations and his review of the manuscript, and Ken Revzan and Iain Walker for their review of the manuscript. This work was supported by the Assistant Secretary for Conservation and Renewable Energy, Office of Building Technologies, Building Systems and Materials Division and

by the Director, Office of Energy, Office of Health and Environmental Research, Human Health and Assessments Division and Pollutant Characterization and Safety Research Division of the U.S. Department of Energy under Contract No. DE-AC03-76SF00098. Additional support was provided by the National Science Foundation through grant BCS-9057298. A software license grant from FLUENT Inc. helped support the computational aspects of the work.

3.7 References

Amtec Engineering I. (1993) Tecplot User's Manual, Bellevue, WA.

Anderson D. A., Tannehill J. C., and Pletcher R. H. (1984) *Computational Fluid Mechanics and Heat Transfer,* McGraw-Hill, New York, NY.

Bauman F. S., Ernest D. R., and Arens E. A. (1988) ASEAN natural ventilation study: Wind pressure distributions on long building rows in urban surroundings, report CEDR-03-88, Center for Environmental Design Research, University of California, Berkeley, Berkeley, CA.

Castro I. P. and Robins A. G. (1977) The flow around a surface-mounted cube in uniform and turbulent streams, *J. Fluid Mech.* **79**, 307-335.

DSMA Atcon Ltd. (1985) A computer study of soil gas movement into buildings, report 1389/1333, Department of Health and Welfare, Ottawa, Canada.

Ernest D. (1991) Predicting wind-induced indoor air motion, occupant comfort, and cooling loads in naturally ventilated buildings, Ph.D. Thesis, Dept. of Architecture, U.C. Berkeley, Berkeley, CA.

ESDU (1985) Characteristics of atmospheric turbulence near the ground, Part II, Item Number 85020, Engineering Sciences Data Unit, London, England.

Ferziger J. (1993) Simulation of complex turbulent flows: Recent advances and prospects in wind engineering, *J. Wind Eng. Ind. Aerodyn.* **46 & 47**, 195-212.

Feustel H. E. and Sherman M. H. (1989) A simplified model for predicting air flow in multizone structures, *Energy Build.* **13**, 217-230.

FLUENT (1993) v4.2, Fluent Incorporated, Centerra Resource Park, 10 Cavendish Court, Lebanon, NH.

Gadgil A. (1992) Models of radon entry, *Radiation Protection Dosimetry* **45**, 373-380.

Hoxey R. P. and Richards P. J. (1993) Flow patterns and pressure field around a full-scale building, *J. Wind Eng. Ind. Aerodyn.* **50**, 203-212.

Levitan M. L. (1993) Analysis of reference pressure systems used in field measurements of wind loads, Ph.D. Thesis, Texas Tech University, Lubbock, TX.

Murakami S. (1993) Comparison of various turbulence models applied to a bluff body, *J. Wind Eng. Ind. Aerodyn.* **46 & 47**, 21-36.

Nazaroff W. W. (1992) Radon transport from soil to air, *Reviews of Geophysics* **30**, 137-160.

Nazaroff W. W., Feustel H., Nero A. V., Revzan K. L., Grimsrud D. T., Essling M. A., and Toohey R. E. (1985) Radon transport into a detached one-story house with a basement, *Atmos. Environ.* **19**, 31-43.

NOAA (1980) Local climatological data, annual summaries for 1980, Part II - NEB-WYO, National Climatic Center, National Oceanic and Atmospheric Administration, Asheville, NC.

Okada H. and Ha Y. C. (1992) Comparison of wind tunnel and full-scale pressure measurement tests on the Texas Tech building, *J. Wind Eng. Ind. Aerodyn.* **43**, 1601-1612.

Patankar S. V. (1980) *Numerical Heat Transfer and Fluid Flow,* Hemisphere Publishing, New York, NY.

Patterson D. A. and Apelt C. J. (1990) Simulation of flow past a cube in a turbulent boundary layer, *J. Wind Eng. Ind. Aerodyn.* **35**, 149-176.

Sakamoto H. and Mikio A. (1982) Flow around a cubic body immersed in a turbulent boundary layer, *J. Wind Eng. Ind. Aerodyn.* **9**, 275-293.

Seinfeld J. H. (1986) *Atmospheric Chemistry and Physics of Air Pollution,* John Wiley, New York, NY.

Sherman M. H. (1992) Simplified modeling for infiltration and radon entry, report LBL-33962, Lawrence Berkeley National Laboratory, Berkeley, CA.

Stathopoulos T. and Zhou Y. S. (1993) Numerical simulation of wind-induced pressures on buildings of various geometries, *J. Wind Eng. Ind. Aerodyn.* **46 & 47**, 419-430.

Surry D. (1991) Pressure measurements on the Texas Tech building - wind tunnel measurements and comparisons with full scale, *J. Wind Eng. Ind. Aerodyn.* **38**, 235-247.

Turk B. H., Prill R. J., Grimsrud D. R., Moed B. A., and Sextro R. G. (1990) Characterizing the occurrence, sources and variability of radon in Pacific Northwest homes, *J. Air Waste Mange. Assoc.* **40**, 498-506.

Zhang Y. Q., Huber A. H., Arya S. P. S., and Snyder W. H. (1993) Numerical simulation to determine the effects of incident wind shear and turbulence level on the flow around a building, *J. Wind Eng. Ind. Aerodyn.* **46 & 47**, 129-134.

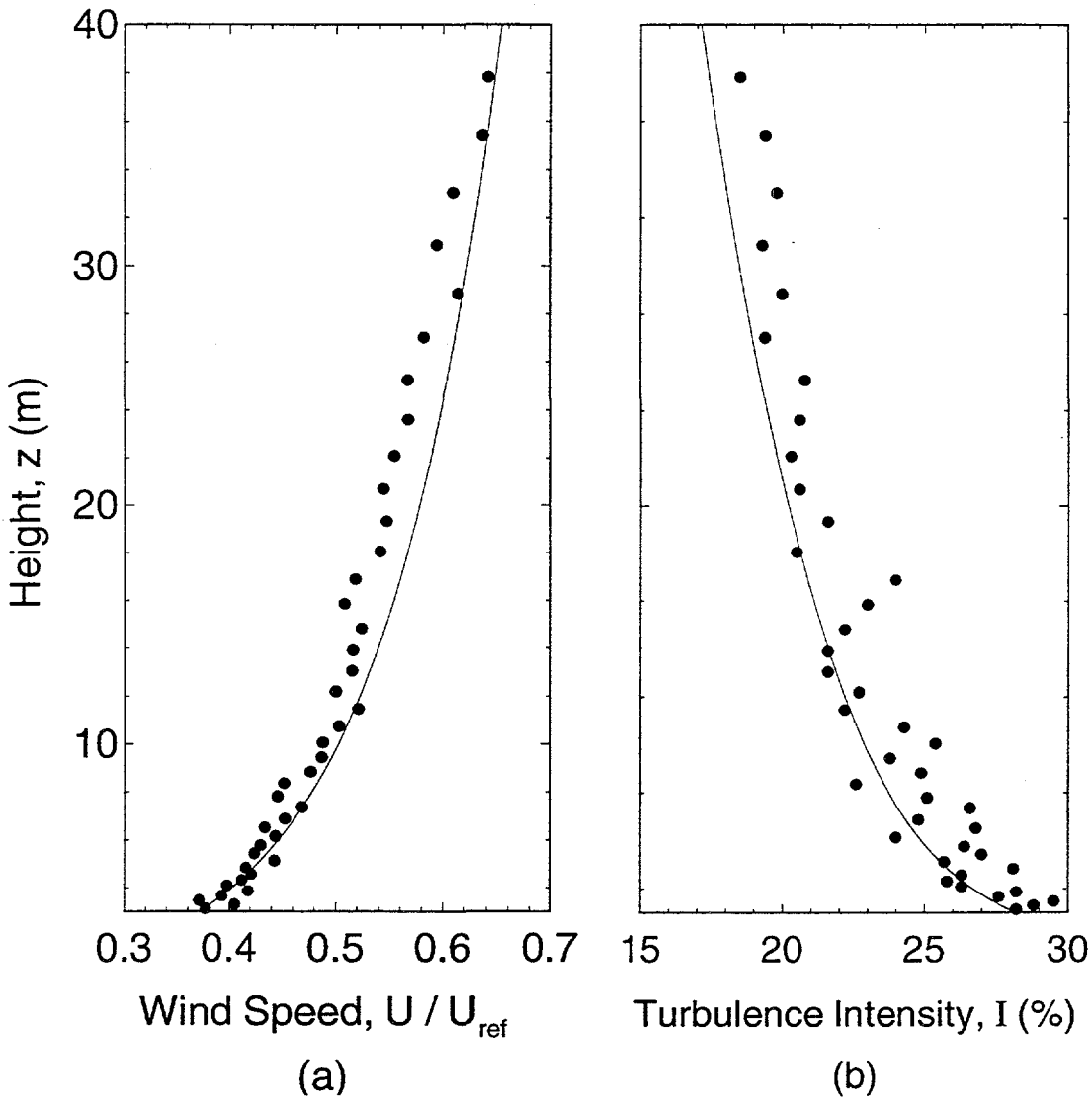

Figure 3.1. Experimental and analytical horizontal wind velocity (a) and turbulence intensity (b), as a function of height above the ground for the "countryside" boundary layer. The solid line in (a) was calculated with equation (3.1) and in (b) from ESDU (1985) correlations.

bpa/windtunnel/fig3-1.dxy
bpa/windtunnel/bl1-intensity

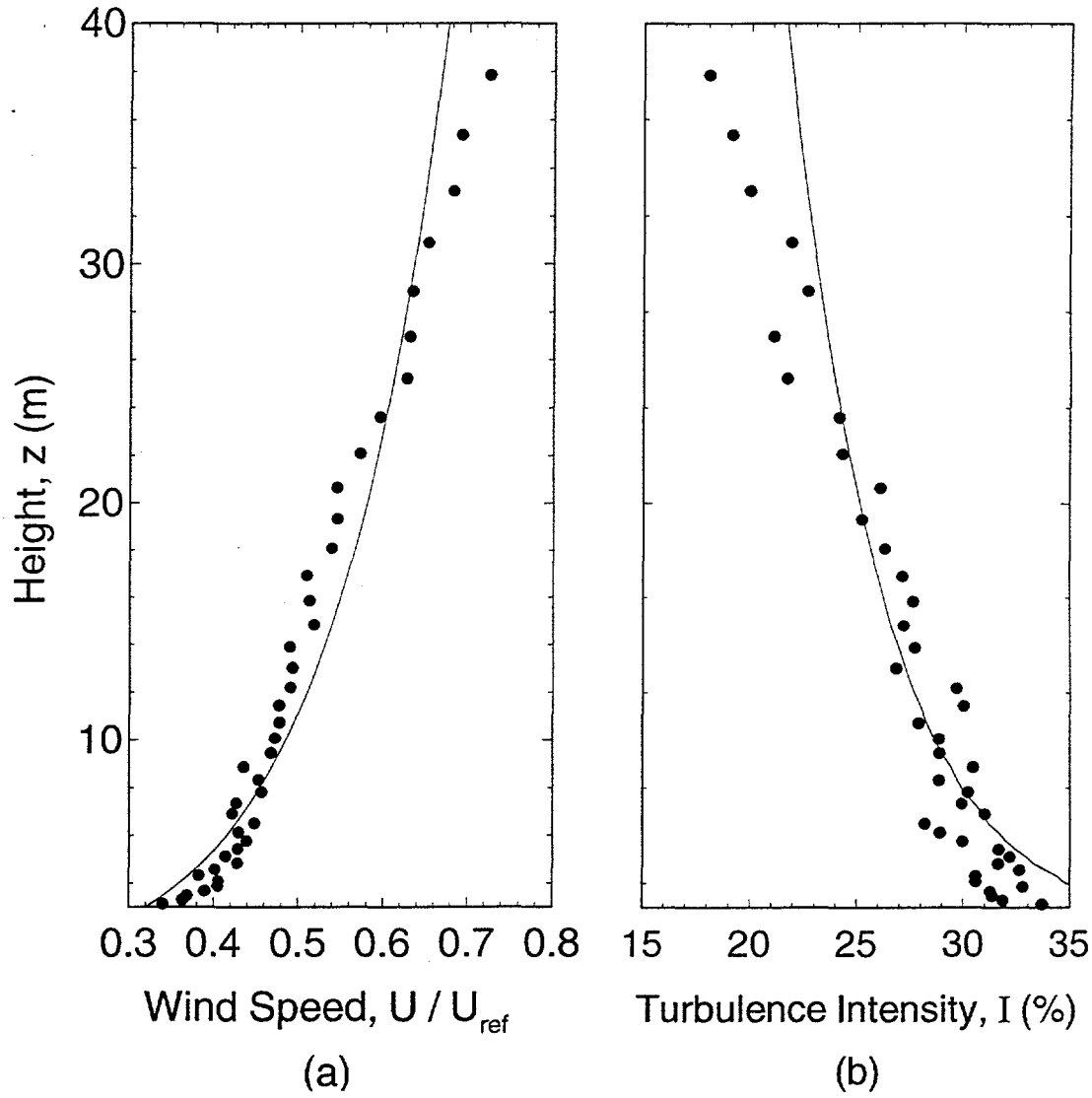

Figure 3.2. Experimental and analytical horizontal wind velocity (a) and turbulence intensity (b), as a function of height above the ground for the "suburban" boundary layer. The solid line in (a) was calculated with equation (3.1) and in (b) from ESDU (1985) correlations.

bpa/windtunnel/fig3-2.lay
bpa/windtunnel/bl2-intensity

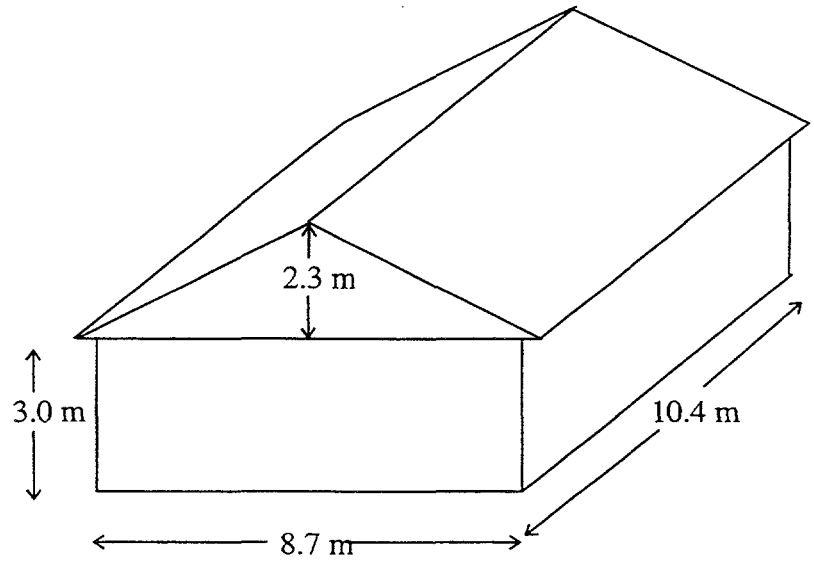

Figure 3.3. The wind tunnel building geometry (1:61 geometrical scale). The sketch is not drawn to scale.

c:\thesis\fig3_3.doc

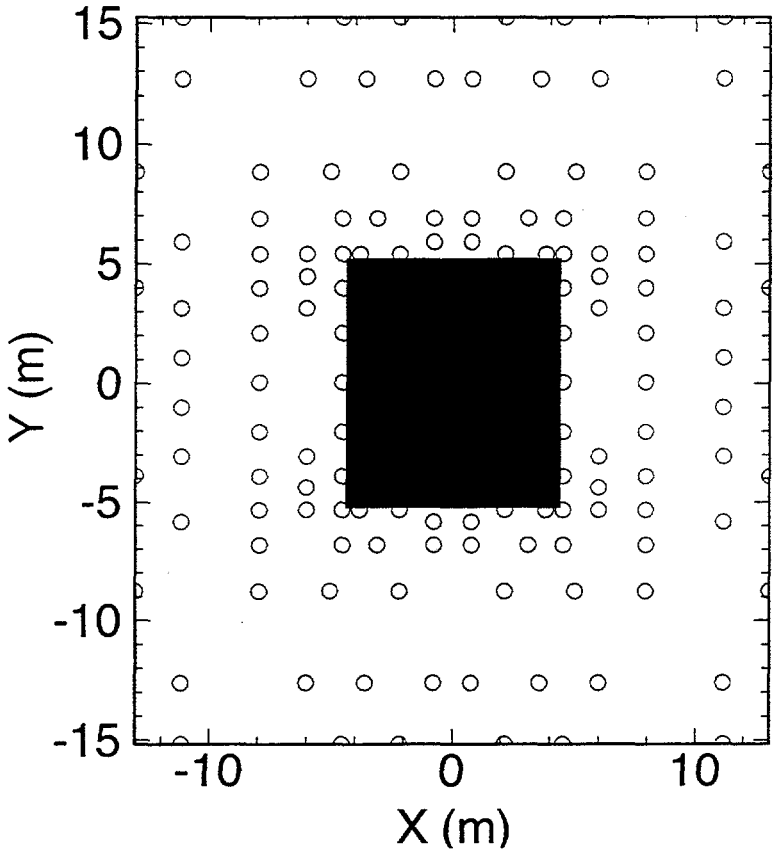

Figure 3.4. Ground-surface pressure tap locations for the wind-tunnel experiment.

user5/bpa/windtunnel/fig3-4.lay

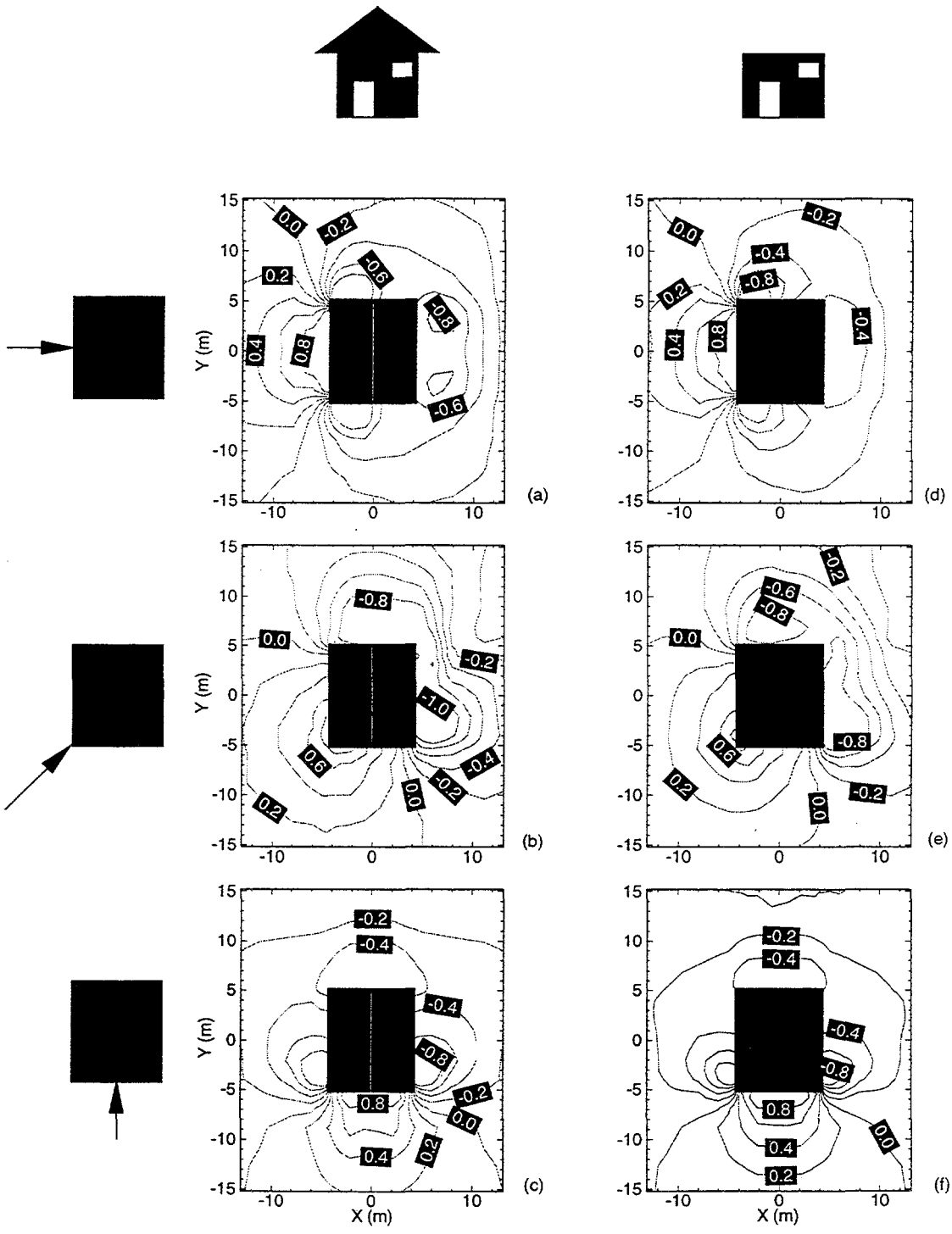

Figure 3.5. Wind tunnel mean ground-surface pressure coefficients for the "countryside" boundary layer. Shown are results for the house with a gable and flat roof at three incident wind angles. The contour interval is 0.2.

/bpa/windtunnel/fig3-5.lay

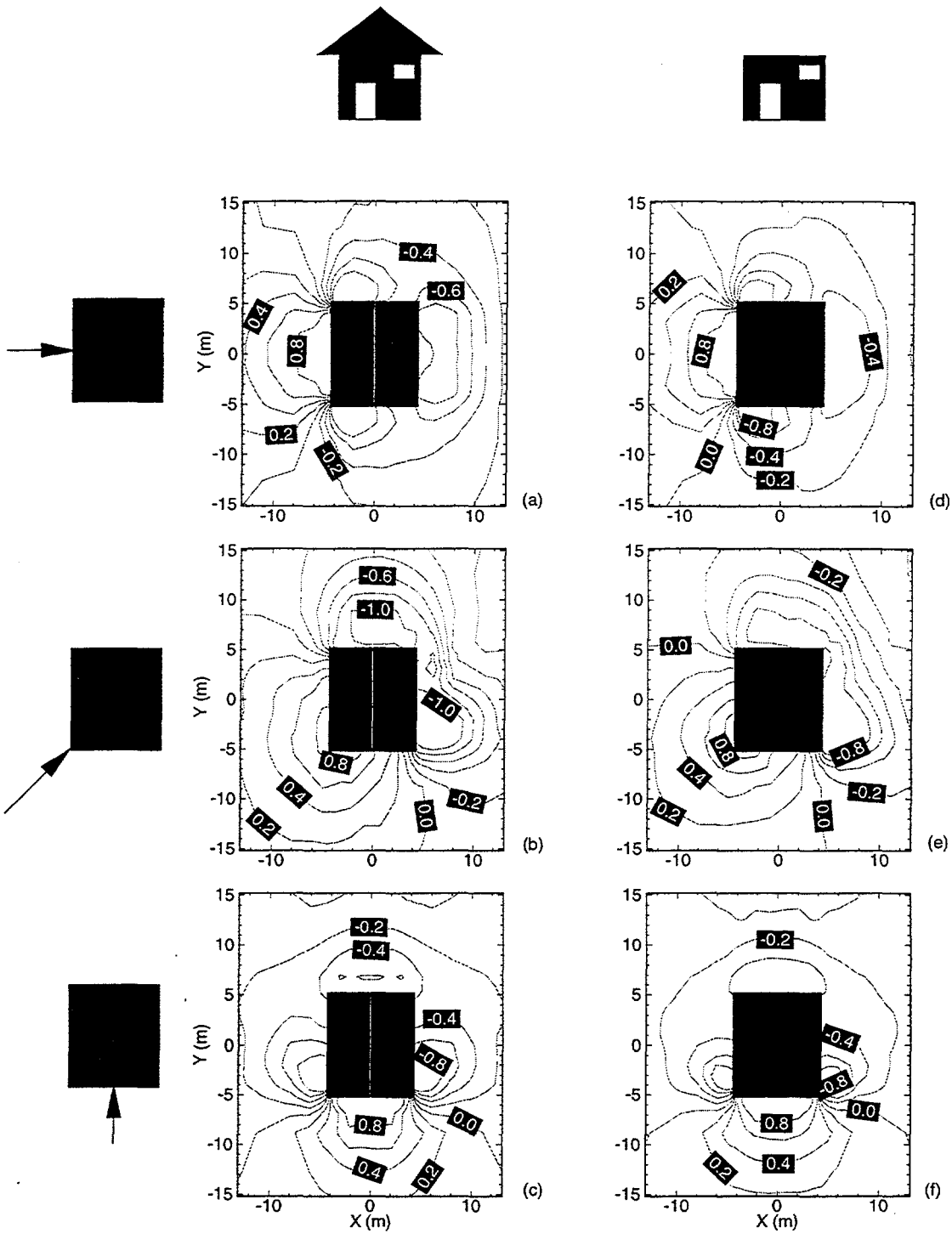

Figure 3.6. Wind tunnel mean ground-surface pressure coefficients for the "suburban" boundary layer. Shown are results for the house with a gable and flat roof at three incident wind angles. The contour interval is 0.2.

/bpa/windtunnel/fig3-6.lay

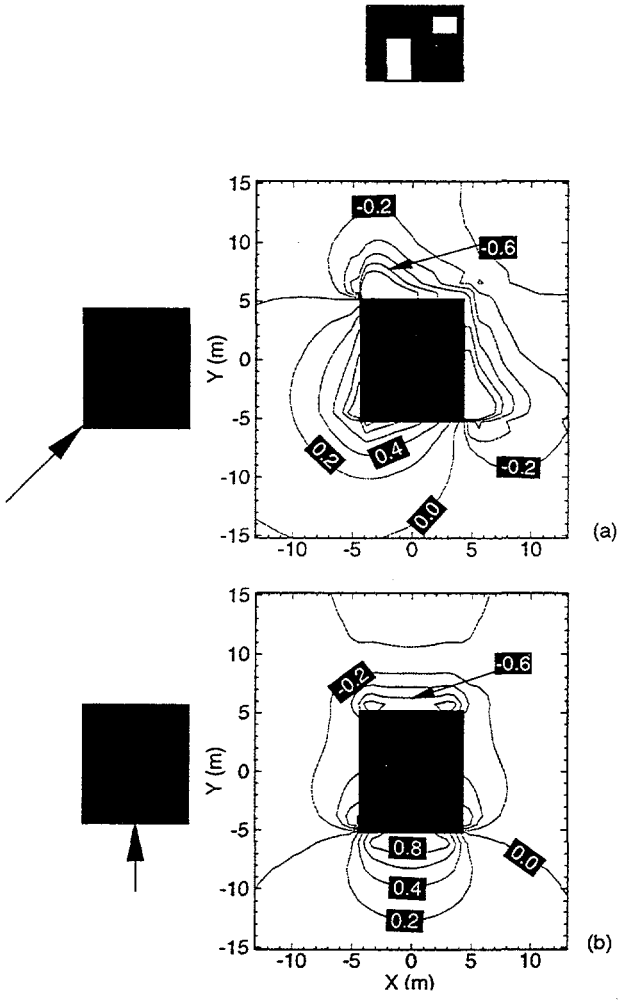

Figure 3.7. Numerical simulation mean ground-surface pressure coefficients for the "countryside" boundary layer. Shown are results for the house with a roof at two incident wind angles. The contour interval is 0.2.

user5/bpa/fluent/fig3-7.lay

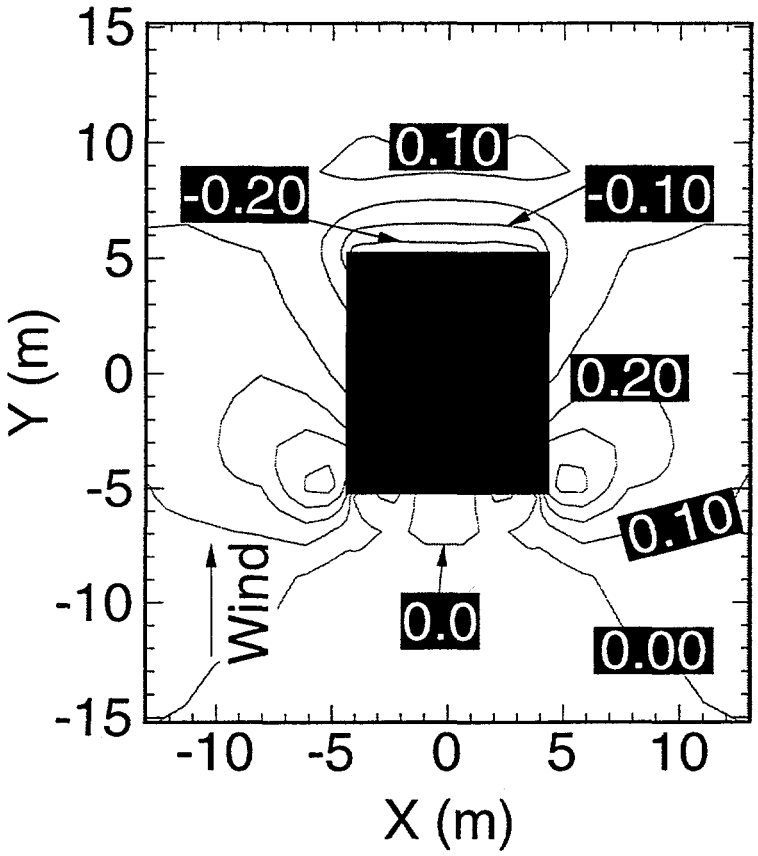

Figure 3.8. Contour plot of the error (numerical simulation value minus wind tunnel value) in mean ground-surface pressure coefficient for the "countryside" boundary layer incident perpendicular to the 8.7 m side of the house. The contour interval is 0.1.

user5/riley/bpa/compare-windtunnel-fluent/fig3-8.lay

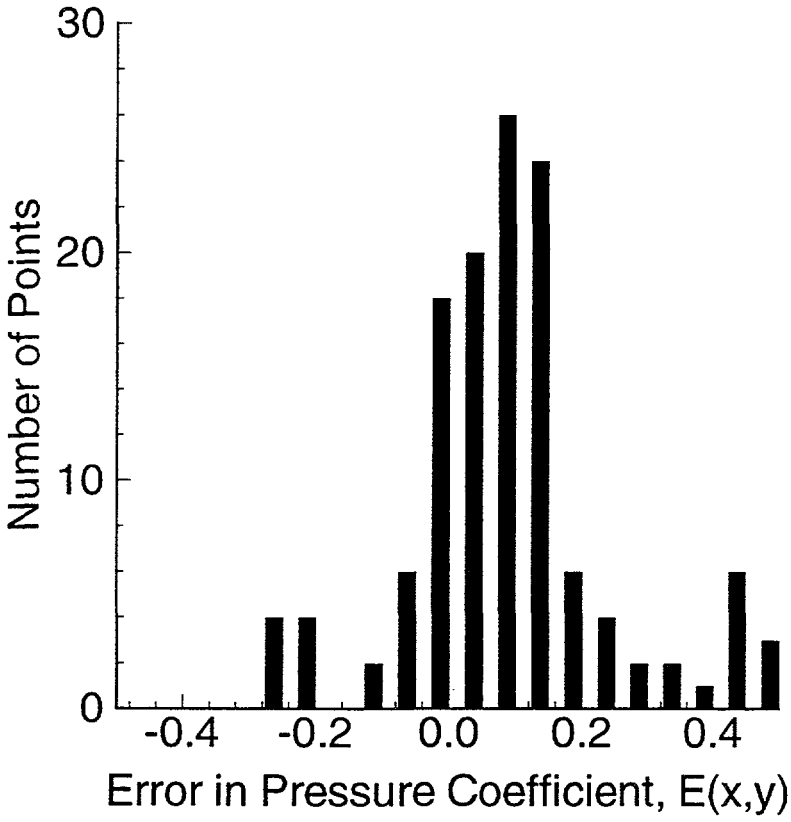

Figure 3.9. Distribution of error (numerical simulation value minus wind tunnel value) in mean ground-surface pressure coefficient for the "countryside" boundary layer incident perpendicular to the 8.7 m side of the house.

bpa/compare-windtunnel-fluent/fig3-9.lay

CHAPTER 4

THE EFFECT OF STEADY WINDS ON RADON-222 ENTRY FROM SOIL INTO HOUSES*

4.1 Abstract

Wind affects the radon-222 entry rate from soil into buildings and the resulting indoor concentrations. To investigate this phenomenon, we employ a previously tested three-dimensional numerical model of soil-gas flow around houses, a commercial computational fluid dynamics code, an established model for determining ventilation rates in the presence of wind, and new wind-tunnel results for the ground-surface pressure field caused by wind. These tools and data, applied under steady-state conditions to a prototypical residential building, allow us (1) to determine the complex soil-gas flow patterns that result from the presence of wind-generated ground-surface pressures, (2) to evaluate the effect of these flows on the radon concentration in the soil, and (3) to calculate the effect of steady wind on the radon entry rate and indoor concentration. For a broad range of soil permeabilities, two wind speeds, and two wind directions, we quantify the "flushing" effect of wind on the radon concentration

---

* This chapter is based on a paper: Riley W. J., Gadgil A. J., Bonnefous Y. C., and Nazaroff W. W. (1996) The effect of steady winds on Rn-222 entry from soil into houses, *Atmos. Environ.* **30**, 1167-1176.

field in the soil surrounding a house, and the consequent sharp decrease in radon entry rates. Experimental measurements of the time-dependent radon concentration in soil gas beneath houses substantiate the prediction of wind-induced flushing. Comparisons are made to model predictions obtained while ignoring the effect of the wind-generated ground-surface pressures. These investigations lead to the conclusion that wind-generated ground-surface pressures play a significant role in determining radon entry rates into residential buildings.

4.2 Nomenclature

A_i	cross-sectional area of a portion of the footer-slab crack (m^2)
A_l	effective leakage area (m^2)
A_w	surface-area element of the house's exterior wall (m^2)
$c_p(x,y)$	ground-surface pressure coefficient at location (x,y) (-)
c	Forchheimer term ($s\ m^{-1}$)
C	radon soil-gas concentration ($Bq\ m^{-3}$)
C_{in}	indoor radon concentration normalized with respect to C_∞ (-)
C_{char}	spatial average of the radon soil-gas concentration normalized with respect to C_∞ (-)
C_∞	deep-soil radon concentration in the soil gas ($Bq\ m^{-3}$)
D	diffusivity of radon through bulk soil ($m^2\ s^{-1}$)
D_w	product of the wall permeability times the wall area ($m^3\ s^{-1}\ Pa^{-n}$)
E	normalized radon entry rate into the basement ($m^3\ s^{-1}$)
f_w	local terrain constant (-)
k	soil permeability (m^2)
n	flow exponent (-)
p_G	soil-gas gage, or disturbance, pressure (Pa)
$p_{gs}(x,y)$	ground-surface pressure at location (x,y) (Pa)
p_∞	free-stream air pressure (Pa)

p_i	pressure inside the building (Pa)
p_w	exterior pressure on an element of the house wall (Pa)
ΔP	pressure difference across a section of the house wall (Pa)
Q	ventilation flow rate ($m^3\ s^{-1}$)
Q_i	air flow rate into or out of the building through a section of the exterior wall ($m^3\ s^{-1}$)
Q_{sg}	soil-gas flow rate into the house ($m^3\ s^{-1}$)
$Q_{s,uv}$	ventilation flow from the stack effect and unbalanced ventilation ($m^3\ s^{-1}$)
S	production rate of radon in the soil gas (Bq $m^{-3}\ s^{-1}$)
V_{eh}	wind speed at eave height (m s^{-1})
$\vec{v}$	soil-gas velocity vector (m s^{-1})

Greek letters

α	empirical constant used in the footer-slab crack model ($m^3\ s\ kg^{-1}$)
β	empirical constant used in the footer-slab crack model (s m^{-1})
ε	porosity of the soil (-)
λ	radon-222 radioactive decay constant ($2.1\times10^{-6}\ s^{-1}$)
μ	dynamic viscosity of air (kg $m^{-1}\ s^{-1}$)
ρ	air density (kg m^{-3})

Note: (-) indicates a nondimensional variable.

4.3 **Introduction**

Advective entry of radon-bearing soil gas is the dominant source of indoor radon in most homes with elevated concentrations (Nazaroff, 1992). In buildings with basements, a small depressurization is sufficient to drive soil gas through cracks in the substructure (such as the joints between the footer and basement slab running along the periphery of the basement). Wind is unique among the causes of this depressurization since it also alters the pressure profile on the ground-surface adjacent to the building. This wind-induced ground-surface pressure field influences soil-gas flow, thereby altering the radon concentration in the soil gas surrounding the building. As summarized below, evidence suggesting that wind can play a role in determining the amount of radon that enters a house has been presented elsewhere. Little has been published, however, with the intent of quantifying this role and understanding the mechanisms involved.

Passive or low-energy radon mitigation systems can also be influenced by wind (Fisk et al., 1995). The effects are especially pronounced when a direct connection between the atmosphere and sub-slab gravel layer is present. Design of these systems will need to account for the effect of wind on both the soil-gas concentrations and the method of coupling the gravel layer to the outdoors.

A striking example of the effects of wind on radon entry rates and indoor concentrations was presented by Turk et al. (1990). Figure 4.1 reproduces their data for a house in the Pacific Northwest showing a strong inverse correlation between wind speed and indoor radon concentration. Although some of the decrease in the indoor

radon concentration with increasing wind speed is due to increased ventilation, this factor is not large enough to account for the full reduction shown. A concurrent reduction in the radon entry rate must also have occurred. The authors hypothesized that the wind ventilated the soil surrounding the house, thus reducing the soil-gas radon available for entry into the building. In the *Results* section of this chapter we present direct experimental evidence of soil-gas flushing at several test houses in New Jersey, and indicate that this depletion follows the trends predicted in our numerical simulations.

Nazaroff et al. (1985) instrumented a house in Illinois to monitor the effects of various environmental factors on radon entry rates. They concluded that when the indoor-outdoor temperature difference was small, high wind speeds were associated with higher radon entry rates, and conversely, when this temperature difference was large, low wind speeds produced higher radon entry rates. They also noticed a correlation between high wind speeds and decreased radon concentrations in the soil gas, possibly as a result of the flushing of radon from the soil gas. Their observations did not lead to conclusive elucidation of the mechanisms responsible for these relationships.

Arnold (1990) conducted an experiment with a three-dimensional scale model of a house, and imposed on the ground surface a simplified version of the wind-induced ground-surface pressure distribution reported by DSMA Atcon Ltd. (1985). Resulting perturbations of the pressure field in the porous medium used to represent the soil were then measured. However, radon concentrations in the ersatz soil were not measured,

and therefore the effect of wind on radon entry rates into the basement was not determined. Ward et al. (1993), in their experimental study of a small building structure, observed a correlation between wind speed and the pressure difference between indoor air and the soil gas. However, the above-ground structure in these experiments is not geometrically similar to a real house. It is therefore difficult to extend these correlations to full scale houses, which are affected by both wind-induced depressurization and the ground-surface pressure field.

DSMA Atcon Ltd. (1985) reported a numerical investigation of the effects of wind speed and direction on radon entry rates using a finite-element model of a simple building. Ground pressure data generated in a small wind tunnel and meteorological data from a summer and winter period in Toronto were used as input to the simulations. Their simulations predicted that both wind speed and wind direction affect the radon entry rate into a building, but they found no general correlation among these factors. Sherman (1992) developed a simplified model of a house to quantify the effects of several factors, including wind, on radon entry. Sherman assumed that the wind did not deplete the soil gas of radon, but did increase the ventilation rate and basement depressurization. He concluded that the stack effect is much more effective at inducing radon entry than is the wind effect. Owczarski et al. (1991) performed a numerical study of the effects of wind and reported expected reductions in the soil-gas radon concentration below a slab-on-grade house with increasing wind speed. However, that study ignored crucial details of building structure (e.g., existence of footers), did not consider the full two-dimensional nature of the wind-generated

ground-surface pressure field, used arbitrary values for wind-generated ground-surface pressures, and considered only Darcy flow through the soil and gravel layer.

Taken in combination, these efforts do not yield a comprehensive picture of how wind affects radon entry rates and indoor concentrations. We aim to improve our understanding by reporting on a detailed investigation of wind-induced radon entry into a prototypical residential building under steady-state conditions. This study particularly emphasizes two issues: the effect of wind-induced ground-surface pressures on the soil-gas radon concentration near a house, and the interplay between ventilation and radon entry in affecting indoor concentrations when both are driven by wind. To pursue these objectives, we employ a largely numerical approach, combining three modeling tools with the wind tunnel data from Chapter 3 of the ground-surface pressure field induced by wind blowing on a building. The modeling tools comprise (1) a previously tested, three-dimensional finite-difference model, known as Non-Darcy STAR (NDSTAR), of soil-gas flow and radon concentrations around buildings (Gadgil et al., 1991; Bonnefous et al., 1992); (2) a commercial computational fluid dynamics code, FLUENT (FLUENT, 1993); and (3) a model for determining the house ventilation rate in the presence of wind (Sherman, 1992). We also present previously acquired but unpublished experimental data that qualitatively substantiates key model predictions. Although the methods employed are general, the modeling results reported in this paper apply specifically to radon-222, the radioisotope responsible for the dominant portion of human radiation exposure.

4.4 Methods

4.4.1 Overview

The simulation of the wind's interaction with the building and surrounding soil was carried out in a five-step process. First, results from wind tunnel experiments (Chapter 3) were used to compute the wind-generated ground-surface pressure field around the house. Second, the wind-induced depressurization in the house was calculated from FLUENT's predictions of the distribution of pressures on the exposed walls. Third, the pressure and velocity fields in the soil gas surrounding the house and in the sub-slab gravel layer were computed using NDSTAR. Fourth, the soil-gas radon concentration field was determined and a radon entry rate into the house was calculated. Finally, the indoor radon concentration was computed using a predicted wind-induced enhancement of the building's ventilation rate. This five-step exercise, which is described in more detail below, was carried out for a range of soil permeabilities, two wind speeds, and two wind directions.

A central approximation in this chapter is that wind establishes a steady-state ground-surface pressure field, depressurization of the house, and flow of soil gas and radon. In reality, both wind speed and direction vary with time. Over the range of soil permeabilities we consider here, the soil-gas pressure field will reach a steady state after a perturbation with a characteristic time of seconds to minutes (Nazaroff et al., 1988). The soil-gas concentration field will reach a steady state with a characteristic time that is the smaller of (1) the time soil gas takes to travel from the soil surface to

the basement (on the order of hours to months, depending on the soil permeability), and (2) the time required for the radon concentration to reach a steady value as a result of its radioactive generation and decay (several days).

Macrometeorological wind fluctuations typically have peaks in the wind energy distribution at periods on the order of days. In contrast, small-scale wind fluctuations have significant energy at periods on the order of a minute (Van der Hoven, 1957). For the macrometeorological region of the wind spectrum, the soil-gas pressure field is likely to reach steady state. However, because the time required for the radon concentration field to equilibrate can be large, the assumption of a steady soil-gas concentration field is not strictly appropriate, even for large scale wind fluctuations. Still, the assumption of steady state captures some of the key features of the problem, and is therefore useful as an important step towards full understanding of the effects of wind on radon entry into homes. The effects of transient winds on soil-gas transport and radon entry into buildings are explored in Chapter 7.

4.4.2 House Substructure and Soil Characteristics

The house geometry was chosen to represent a typical single-family structure in size and aspect ratio, but not intended to characterize a statistically "normal" home. The building has a plan area of 8.7 m x 10.4 m; the basement and footers represent standard construction practice and are depicted in Figure 4.2 (a). A 1 mm L-shaped crack provides the route for advective entry of radon into the basement. Advective flow through this channel is modeled with the equation (Baker et al., 1987)

$$\vec{\nabla} p_G = \alpha(1 + \beta|\vec{v}|)\vec{v} \tag{4.1}$$

where p_G is the soil-gas gage, or disturbance, pressure (Pa), α and β are empirically determined constants that are functions of the crack geometry, and $\vec{v}$ is the soil-gas velocity vector (m s^{-1}). For this study α is 860 kg m^{-3} s^{-1} and β is 0.035 s m^{-1} (Gadgil et al., 1991).

We varied the gas-phase permeability of the soil surrounding the house from 1×10^{-11} m^2 to 1×10^{-8} m^2. The lower bound was chosen because wind does not significantly affect soil-gas radon concentrations below this value. The upper bound is a permeability above which no houses are expected to be found (Nazaroff, 1992). The permeability of the gravel placed under the basement slab is taken as 3×10^{-7} m^2, corresponding approximately to a 4.5 cm round gravel (Gadgil et al., 1991).

4.4.3 Wind-Induced Ground-Surface Pressure Field

The pressure field established around a house in the presence of wind was determined by conducting scale experiments in the U.C. Berkeley Architecture Department's wind tunnel facility (see Bauman et al. (1988) for a description of the wind tunnel; see Chapter 3 for details regarding these experiments). For the results presented here, the house is a box of scaled dimension 8.7 m × 10.4 m × 3 m. The ground-surface pressure coefficient, $c_p(x, y)$, is defined as

$$c_p(x,y) = \frac{p_{gs}(x,y) - p_\infty}{\frac{1}{2}\rho V_{eh}^{\ 2}} \tag{4.2}$$

where $p_{gs}(x,y)$ is the ground-surface pressure (Pa) at location (x,y), p_∞ is the free-stream pressure (Pa), ρ is the air density (kg m^{-3}), and V_{eh} is the free-stream wind speed at an eave height of 3 m (m s^{-1}). Castro and Robins (1977) demonstrated that, for wind speeds above about 0.5 m s^{-1}, the pressure coefficient field field around the building does not depend on wind speed. Figures 4.3 (a) and 4.3 (b) present the ground-surface pressure coefficient field for the case of wind incident perpendicular to the short side of the house and incident at 45° to the side of the house, respectively.

Eave-height wind speeds of 0, 3.6, and 8.3 m s^{-1} are used in combination with equation (4.2) and the results presented in Figure 4.3 to define the ground-surface pressure field for the simulations. The non-zero wind speeds correspond to the 50th and 95th percentile wind speeds, respectively, over a period of approximately 25 years in Spokane, Washington (NOAA, 1980). This location was chosen because radon entry and mitigation has been investigated in several houses in the area (Turk et al., 1990). The 3.6 and 8.3 m s^{-1} wind speeds are values which have been scaled to eave height by assuming the measurements were taken in the "countryside" boundary layer, a structure which corresponds well to conditions around most measuring stations. For comparison, the average wind speed in the U.S. is 4.1 m s^{-1}.

4.4.4 Wind-Induced Indoor Depressurization

The depressurization of the house air can be caused by several factors. We consider only wind-induced depressurization in order to focus attention on the effects of wind on the radon entry rate. Physically, this situation would occur under steady wind conditions when the indoor-outdoor temperature difference is small and no mechanical ventilation or heating equipment is operating. To highlight the importance of including the wind-induced ground-surface pressures, we have performed analogous simulations (same house geometry and range of soil permeabilities) with the ground surface at atmospheric pressure and a basement depressurization of -11 Pa. This is the basement depressurization that we estimate is caused by an 8.3 m s^{-1} wind, as described below.

The indoor depressurization is computed by balancing the total flow into and out of the building (Mowris and Fisk, 1988)

$$Q_i = D_w(\Delta P)^n \tag{4.3}$$

where Q_i is the air flow rate into or out of the building through the section of the exterior wall being considered (m^3 s^{-1}), D_w is the product of the average wall permeability times the area of that section of the wall (m^3 s^{-1} Pa^{-n}), ΔP is the pressure difference across that section of the wall (Pa), and n is a flow exponent (-). The flow exponent depends on the character of the flow through the cracks: it is 1.0 when flow resistance is dominated by viscous forces, and 0.5 when flow resistance is dominated by

inertial forces. A typical value, integrated over all the cracks in a house, is 0.66 (Sherman et al., 1984). Equation (4.3) and the requirement that the air mass in the building remains constant gives

$$\sum_{surfaces}(A_w)*\text{sign}(p_w - p_i)*(p_w - p_i)^n = 0 \tag{4.4}$$

where A_w is the surface area of an element of the exterior wall (m^2), p_w is the exterior pressure on that element of the wall (Pa), and p_i is the pressure inside the building (Pa). In deriving equation (4.4) we have assumed an equal distribution of leakage area around the house (i.e., D_w is independent of position), a flow exponent that is independent of position, and that the building has no mechanical supply or exhaust.

We used FLUENT to determine p_w by solving the conservation equations for mass and momentum in the air flow around the house. FLUENT uses a control-volume based, finite-difference discretization technique, and we used the k-ε model to simulate turbulence. The computational grid included open space a distance of six house dimensions from the building in both horizontal directions, a vertical dimension of 61 m, and was divided into 100,000 control volumes. The building's walls were modeled as smooth surfaces. We have assumed that the house is isolated from other buildings, and that the atmospheric boundary layer corresponds to what might be expected on the outskirts of a small town (see Chapter 3 for other details of this simulation).

Equation (4.4) is solved iteratively once the values for p_w are determined. With the wind perpendicular to the short side of the house, the interior depressurization is predicted to be -11 Pa for a wind speed of 8.3 m s^{-1}, and -2.0 Pa for a wind speed of 3.6 m s^{-1}.

Because the predicted values of p_i are subject to inaccuracies inherent in the FLUENT simulation, we also computed the building depressurization by the method of Feustel (1985). For the wind speeds given above, we calculate building depressurizations of -13 and -2.4 Pa, respectively. These values are both within 20% of the values computed using FLUENT.

4.4.5 Soil-Gas Pressure and Velocity Fields

The soil-gas pressure, velocity, and concentration fields were computed in a soil block that measures 30.4 m × 26.2 m horizontally, and extends 11.9 m below the soil surface (Figure 4.2 (b)). There are 40,716 node points in this volume. The exterior surfaces of the soil block are taken to be Neumann boundaries (no flow), as are all interfaces where the soil meets the basement. The Neumann boundary at the bottom of the computational space is equivalent to assuming that an impermeable layer exists at this depth (e.g., water table). Dirichlet boundaries (fixed pressure) are imposed on the ground surface and along the crack that connects the sub-slab gravel layer with the basement.

The pressure and velocity fields in the soil gas are solved simultaneously using the three-dimensional finite-difference software package NDSTAR (Gadgil et al., 1991;

Bonnefous et al., 1992). This package can model both Darcy and non-Darcy flow of soil gas, as appropriate, in regions of gravel and soil. The non-Darcy flow is modeled with the Darcy-Forchheimer equation (Forchheimer, 1901):

$$\vec{\nabla} p_G = -\frac{\mu}{k}(1 + c|\vec{v}|)\vec{v} \tag{4.5}$$

where p_G is the soil-gas gage, or disturbance, pressure (Pa), k is the soil permeability (m^2), μ is the dynamic viscosity (kg m^{-1} s^{-1}), and c is the Forchheimer term (s m^{-1}). Gadgil et al. (1991) describe the experimental procedure used to determine the Forchheimer term; Table 4.1 presents the values of c used here as a function of soil permeability. For the simulations presented here, the soil-gas flow is always Darcian; the Forchheimer term therefore does not significantly affect the simulation results.

Since the disturbance pressure is always small relative to atmospheric pressure, the soil gas is treated as incompressible. Therefore, the continuity equation becomes:

$$\vec{\nabla} \cdot \vec{v} = 0 \tag{4.6}$$

The model assumes that each zone of soil is homogeneous and isotropic, the concrete basement walls and floor are impermeable to soil-gas flow (except through the cracks), and the effect of buoyancy on soil-gas flow is negligible. A modified SIMPLE algorithm (Patankar, 1980) is used to discretize equations (4.5) and (4.6), and the pressure and velocity fields are calculated on staggered grids using an alternate direction implicit method. The solution procedure is terminated when the computed

pressure at each point changes fractionally by less than 1×10^{-6} over successive iterations.

4.4.6 Soil-Gas Concentration Field

Given the soil-gas velocity field, the radon concentration is calculated from the steady-state radon mass balance equation

$$\vec{\nabla}\cdot\left(D\vec{\nabla}C\right)-\vec{\nabla}\cdot(\vec{v}C)+\varepsilon(S-\lambda C)=0 \tag{4.7}$$

where C is the radon concentration in the soil gas (Bq m^{-3}), S is the emanation rate of radon from soil grains into the soil gas (Bq m^{-3} s^{-1}), λ is the radon decay constant (s^{-1}), and ε is the porosity of the soil (-). D is the diffusivity of radon through bulk soil (10^{-6} m^2 s^{-1}). D represents the ratio of the radon flux per total surface area to the pore concentration gradient over the distance between two points in the soil, divided by the tortuosity. In contrast to the pressure and velocity field computations, the ground surface here is represented by a mixed boundary condition because there may be areas (i.e. on the leeward side of the house) where the magnitudes of the advective and diffusive radon flux out of the ground are comparable.

The normalized radon entry rate into the basement is then calculated by summing the flux into the crack over the cross-sectional area of the crack

$$E=\frac{\sum_i C\cdot\vec{v}\cdot A_i}{C_\infty} \tag{4.8}$$

where E is the normalized radon entry rate into the basement ($m^3\ s^{-1}$), A_i is the cross-sectional area (m^2) of the portion of the crack under consideration, C and $\bar{v}$ are evaluated at the opening of the crack in the gravel layer, and C_∞ is the radon concentration in the soil gas far below the surface ($Bq\ m^{-3}$).

4.4.7 *Indoor Radon Concentration*

The normalized, steady-state indoor radon concentration is calculated from the normalized radon entry rate and an estimate of the house's ventilation rate. We use the LBL infiltration model (Sherman, 1992) to estimate the ventilation flow rate, Q ($m^3\ s^{-1}$), in the presence of wind:

$$Q = \left[A_l^{\,2} f_w^{\,2} V_{eh}^{\,2} + Q_{sg}^{\,2} + Q_{s,uv}^{\,2} \right]^{0.5} \tag{4.9}$$

where A_l is an effective leakage area (m^2), f_w is a wind parameter equal to 0.23, corresponding to a lightly shielded building (Mowris and Fisk, 1988), Q_{sg} is the soil-gas flow rate into the house ($m^3\ s^{-1}$), and $Q_{s,uv}$ is the ventilation flow ($m^3\ s^{-1}$) from the stack effect and unbalanced ventilation. Note that for cases with wind, $Q_{s,uv}$ is set to zero, and for cases without wind, V_{eh} is set to zero. We use an effective leakage area of $6.1 \times 10^{-2}\ m^2$. This number was reported by Palmiter and Brown (1989) in their study of Northwest houses as an average value for homes without ducted heating systems.

Table 4.2 lists the four simulation cases we examined and indicates for each the basement depressurization, house air-exchange rate, and whether wind-induced ground-surface pressures are included.

The normalized indoor radon concentration, C_{in}, is calculated as

$$C_{in} = \frac{E}{Q} \tag{4.10}$$

The dimensional indoor radon concentration equals the product of C_{in} and C_{∞}. A typical value for C_{∞} is 30 kBq m^{-3} (Nazaroff, 1992).

4.5 Results and Discussion

4.5.1 Radon and Soil-Gas Entry Rates

Figure 4.4 (b) shows predicted normalized radon entry rates as a function of soil permeability for wind speeds of 3.6 and 8.3 m s^{-1} at a wind incidence angle of 0°, and for a wind speed of 8.3 m s^{-1} at a wind incidence angle of 45°. We plot the results for Case 1 on a separate graph (Figure 4.4 (a)) to emphasize that here the ground surface is at atmospheric pressure, although the basement depressurization remains -11 Pa.

The simulation predictions with a uniform ground-surface pressure (Case 1) follow a commonly observed pattern over a wide range of house geometries (e.g., Revzan and Fisk, 1992). For soil permeabilities less than about 1×10^{-10} m^2 the radon

entry rate increases linearly as soil permeability increases. However, as the soil permeability increases above this value, the radon entry rate begins to level off. The lower resistance to soil-gas flow accompanying the increase in soil permeability causes more of the pressure drop between the basement and the soil surface to occur across the footer-slab crack. The result is a lower driving force for soil-gas movement and hence radon entry. For larger crack sizes, the flow of soil gas into the basement can continue to increase with increasing soil permeability (Mowris and Fisk, 1988). In this case, the depletion of radon in the soil gas adjacent to the crack can also be a factor in limiting the radon entry rate at high soil permeabilities (Nazaroff and Sextro, 1989).

The predictions that include wind-induced ground-surface pressures (Cases 2-4) show a remarkably different dependence on soil permeability. For these cases, the radon entry rate peaks at a soil permeability approximately in the range $(1\text{-}3)\times10^{-10}$ m^2; further increases in soil permeability lead to substantially lower entry rates. Even at a permeability of 10^{-11} m^2, the radon entry rate is significantly affected when the ground-surface pressure field is included, as can be seen by comparing Case 1 results with the others.

Simulations were also performed with the higher basement depressurizations obtained using the technique of Feustel (1985): -13 Pa for a wind speed of 8.3 m s^{-1} and -2.4 Pa for a wind speed of 3.6 m s^{-1}. The shape of the curves were similar to those shown in Figure 4.4, demonstrating that the qualitative effect of wind on the radon entry rate is not a sensitive function of basement depressurization.

The predicted soil-gas flow rate into the basement is shown in Figure 4.5 (a) for Case 1, and Figure 4.5 (b) for Cases 2, 3, and 4. For all soil permeabilities the soil-gas entry rate is predicted to be less when the wind is blowing than when it is not. Wind pressurizes the soil surface on one side and depressurizes it on three sides of the building with respect to the free-stream pressure. This effect reduces the soil-gas entry rate because the net area-weighted pressure difference between the basement and the ground surface is reduced. Nevertheless, the trend of the soil-gas entry rate versus soil permeability curve is similar to the case without wind.

4.5.2 Wind-Induced Flushing of Soil-Gas Radon

A detailed examination of the simulation results reveals the underlying reason for the sharp drop in radon entry rate with increasing soil permeability when the house is exposed to wind. The bulk soil-gas flow under the house that is driven by wind-induced ground-surface pressures increases dramatically as the soil permeability increases. In this flow, air enters the ground on the windward side of the house, and soil gas exits the ground surface on the other three sides of the building. The result is a significant flushing of radon from the soil gas beneath the house, and, as a consequence, a diminished source for radon entry into the basement. In addition, because of the complex distribution of pressure on the ground surface, there are unanticipated soil-gas flow patterns on the leeward side of the house.

Figure 4.6 (a) shows normalized soil-gas radon concentrations in a vertical plane bisecting the soil block parallel to both the long side of the house and the

8.3 m s^{-1} wind. The dominant flow paths for the soil gas start from the soil surface on the left, proceed under the house, and exit from the soil surface on the right. For comparison, Figure 4.6 (b) shows the analogous contours of soil-gas radon concentration for the case without wind. The extent to which the wind flushes radon from soil gas is illustrated by comparing Figures 4.6 (a) and 4.6 (b). It is apparent that, in the presence of wind, increasing soil permeability leads to sharply depressed levels of soil-gas radon in the vicinity of the footer-slab crack.

To quantify this effect, we define a characteristic soil-gas radon concentration, C_{char} , to represent the radon source available for entry into the basement. C_{char} is calculated by taking the area-weighted average of the normalized radon concentration in a plane surface bounded by the lower interior edges of the footers. Figure 4.7 presents this parameter for the same four cases considered in Figure 4.4. When there is no wind, C_{char} is not a sensitive function of soil permeability (Figure 4.7 (a)), and the result is a radon entry rate that generally follows the soil-gas flow rate into the basement. However, in the presence of wind, C_{char} decreases sharply with increasing soil permeability (Figure 4.7 (b)), leading to a decreasing radon entry rate. To summarize, the higher the soil permeability, the larger the extent of soil-gas flushing in the presence of a steady wind. The result is a lower available radon source, and therefore a lower radon entry rate.

Figure 4.8 shows soil-gas streamlines for an 8.3 m s^{-1} wind and a soil permeability of 3×10^{-9} m^2 in the same vertical plane used in Figure 4.6. Notice the

significant flow of soil gas that enters the gravel layer on the windward side of the house, moves through the gravel layer, and then exits on the leeward side. The high permeability gravel layer offers a preferred short-circuit path between the windward and leeward sides of the house. The second interesting feature of the flow occurs in the soil region on the leeward side of the house, where soil gas moves back toward the house. This peculiarity results because the leeward ground-surface pressure far from the house is larger than the pressure near the house (see Figure 4.3 (a)). Although the magnitude of the flow depends on soil permeability, the qualitative features shown here are fairly constant over the range of soil permeabilities and wind speeds examined.

4.5.3 *Indoor Radon Concentration*

The normalized indoor radon concentration, C_{in} , is plotted as a function of wind speed and soil permeability in Figure 4.9. Notice that the indoor radon concentration curves are similar in form to the radon entry rate curves shown in Figure 4.4. Figures 4.4 and 4.9 suggest that a house exposed to a sustained wind will experience a substantial decrease in radon entry rate and indoor concentration, and that this decrease is a result not only of the increase in ventilation associated with the wind, but also of the concurrent flushing of radon from the soil gas in the vicinity of the house.

4.5.4 Experimental Evidence of Soil-Gas Flushing

One of the key predictions of this study is that the radon concentration in soil gas near a house can be depleted by wind-induced flushing. To explore whether this predicted behavior occurs in reality, we examined previously acquired data from an investigation of radon entry and mitigation in New Jersey (Turk et al., 1991). In that study, seven houses were instrumented to determine the effectiveness of five different radon control techniques. For several of these houses, control periods occurred during which no mitigation system was operating and indoor and outdoor temperatures, sub-slab soil-gas radon concentrations, and wind speeds were monitored simultaneously. The sub-slab radon measurements were taken approximately in the center of the slab near the interface between the gravel and soil. We examined the data from three houses: LBL09, LBL10, and LBL14. Ten periods were identified during which the wind speed was low for several hours, then increased and remained high for several hours, and the indoor-outdoor temperature difference was relatively stable. The change in soil-gas radon concentration over each of these periods was determined. For nine of the ten periods the soil-gas radon concentration was observed to diminish in response to increasing wind. Of the nine cases showing a decrease in soil-gas radon concentration, the range of ratios of soil-gas radon concentrations during the high and low wind conditions is 0.1 to 0.7. The smallest values of this ratio generally occur for the largest high wind speeds. Figure 4.10 shows two periods from one house that are illustrative of the effects of wind on the soil-gas radon concentration. Table 4.3

presents the wind speeds and soil-gas radon concentrations (computed as a two-hour average) immediately before (low wind) and during (high wind) the ten episodes in the three houses.

Several assumptions employed in the model calculations are not met in these experiments: steady wind speed and direction, steady indoor-outdoor temperature difference, and a steady wind direction of 0 or 45°. In addition, the modeled house geometry is different than all three of these houses, and the soil-gas radon concentrations and small-scale soil permeability measurements are made at only one or two locations near the house. Therefore, these experiments cannot be used to quantitatively validate our modeling results. They do, however, support a key qualitative finding: wind can reduce soil-gas radon concentrations in the vicinity of a house.

4.6 Conclusions

Wind has a significant effect on radon entry rates and indoor concentrations in houses with basements. In addition to the well-established results that wind increases the building's ventilation rate and relative depressurization, soil-gas flow generated by wind-induced ground-surface pressures flushes radon from the soil near the house. The concentration of radon in the soil gas being drawn into the basement is thereby reduced; the result is a substantially lower radon entry rate. Since real houses are regularly exposed to wind, this effect must be included if radon entry is to be properly modeled.

The effect of ignoring wind-induced ground-surface pressures is illustrated by comparing the radon entry rates and indoor concentrations for Cases 1 and 2 (Figures 4.4 and 4.9). In the absence of wind-induced ground-surface pressures (Case 1), the radon entry rate and indoor concentration increase by an order of magnitude as the soil permeability increases from 10^{-11} to 10^{-8} m^2. However, including the effects of wind on ground-surface pressures (Case 2) reduces the predicted radon entry rate relative to Case 1 by a factor ranging from 3 at a permeability of 10^{-11} m^2 to 1000 at a permeability of 10^{-8} m^2. The predicted indoor concentrations differ between Cases 1 and 2 by the same factors. Therefore, predictions concerning the effect of wind on indoor radon concentrations must include ground-surface pressures to avoid substantial errors, especially in regions having high soil permeability.

In addition to the cases presented here, we also conducted simulations with other ground-surface pressure fields (based on DSMA Atcon Ltd.'s (1985) wind tunnel results and numerical simulation results from FLUENT), basement depressurizations, wind speeds, and wind angles. The effect of wind on the radon entry rate was found to be qualitatively the same as in the cases summarized here. We therefore conclude that, for this house geometry, the observed trends are robust.

The effects of a time-varying wind velocity on radon entry rates and indoor concentrations remain to be explored. Chapter 6 describes the development of the transient simulation tool, RapidSTART, that is used in Chapter 7 to simulate several fluctuating wind cases. An understanding of the effects of transient winds on radon entry is also expected to be important in the design of passive or low-energy mitigation

systems where a direct connection between the atmosphere and the sub-slab gravel layer may be present (Fisk et al., 1995).

Further work is also required to determine the effect of wind on the radon entry rate into houses with different geometries (e.g., L-shaped or split-level homes) and high-rise buildings. Such buildings may respond differently than predicted here because of differences in the wind-induced ground-surface pressure field.

In summary, we have found the effects of a steady wind on radon entry rates and indoor radon concentrations to be substantial. Accounting only for the influence of wind on building depressurization and ventilation is insufficient to predict the total effect of wind on indoor radon concentrations. The concurrent flushing of radon from the soil gas that is driven by wind-generated ground-surface pressures must also be considered. Further study of the effects of wind on radon entry (i.e. considering transient winds and different building geometries) is necessary to complete our understanding of this phenomenon and enable us to design effective passive radon mitigation systems.

Acknowledgments-This work was supported by the Assistant Secretary for Conservation and Renewable Energy, Office of Building Technologies, Building Systems and Materials Division and by the Director, Office of Energy, Office of Health and Environmental Research, Human Health and Assessments Division and Pollutant Characterization and Safety Research Division of the U.S. Department of Energy under Contract No. DE-AC03-76SF00098. Additional support was provided by the National

Science Foundation through grant BCS-9057298. The authors thank Bill Fisk for many helpful conversations. Also, the authors thank Phil Price, Ken Revzan, and Rich Sextro for their thorough review of the manuscript. A software license grant from FLUENT Inc. helped support the computational aspects of the work.

4.7 References

Arnold L. J. (1990) A scale model study of the effects of meteorological, soil, and house parameters on soil gas pressures, *Health Phys.* **58**, 559-573.

Baker P. H., Sharples S., and Ward I. C. (1987) Air flow through cracks, *Building and Environment* **4**, 293-304.

Bauman F. S., Ernest D. R., and Arens E. A. (1988) ASEAN natural ventilation study: Wind pressure distributions on long building rows in urban surroundings, report CEDR-03-88, Center for Environmental Design Research, University of California, Berkeley, Berkeley, CA.

Bonnefous Y. C., Gadgil A. J., Fisk W. J., Prill R. J., and Nematollahi A. R. (1992) Field study and numerical simulation of subslab ventilation systems, *Environ. Sci. Technol.* **26**, 1752-1759.

Castro I. P. and Robins A. G. (1977) The flow around a surface-mounted cube in uniform and turbulent streams, *J. Fluid Mech.* **79**, 307-335.

DSMA Atcon Ltd. (1985) A computer study of soil gas movement into buildings, report 1389/1333, Department of Health and Welfare, Ottawa, Canada.

Feustel H. E. (1985) Development of a simplified multizone infiltration model, report LBL-19005, Lawrence Berkeley Laboratory, Berkeley, CA.

Fisk W. J., Prill R. J., Wooley J., Bonnefous Y. C., Gadgil A. J., and Riley W. J. (1995) New methods of energy efficient radon mitigation, *Health Phys.* **68**, 689-698.

FLUENT (1993) v4.2, Fluent Incorporated, Centerra Resource Park, 10 Cavendish Court, Lebanon, NH.

Forchheimer P. H. (1901) *Z. Ver. Dtsch. Ing.* **45**, 1782-1788.

Gadgil A. J., Bonnefous Y. C., Fisk W. J., Prill R. J., and Nematollahi A. (1991) Influence of subslab aggregate permeability on SSV performance, report LBL-31160, Lawrence Berkeley National Laboratory, Berkeley, CA.

Mowris R. J. and Fisk W. J. (1988) Modeling the effects of exhaust ventilation on ^{222}Rn entry rates and indoor ^{222}Rn concentrations, *Health Phys.* **54**, 491-501.

Nazaroff W. W. (1992) Radon transport from soil to air, *Reviews of Geophysics* **30**, 137-160.

Nazaroff W. W., Feustel H., Nero A. V., Revzan K. L., Grimsrud D. T., Essling M. A., and Toohey R. E. (1985) Radon transport into a detached one-story house with a basement, *Atmos. Environ.* **19**, 31-43.

Nazaroff W. W., Moed B. A., and Sextro R. G. (1988) Soil as a source of indoor radon: Generation, migration, and entry, In Nazaroff W. W. and Nero A. V. (Ed.) *Radon and Its Decay Products in Indoor Air*, John Wiley and Sons, New York, 57-112.

Nazaroff W. W. and Sextro R. G. (1989) Technique for measuring the indoor ^{222}Rn potential of soil, *Environ. Sci. Technol.* **23**, 451-458.

NOAA (1980) Local climatological data, annual summaries for 1980, Part II - NEB-WYO, National Climatic Center, National Oceanic and Atmospheric Administration, Asheville, NC.

Owczarski P. C., Holford D. J., Burk K. W., Freeman H. D., and Gee G. W. (1991) Effect of winds in reducing sub-slab radon concentrations under houses laid over gravel beds, Proc. of The 1991 International Symposium on Radon and Radon Reduction Technology, Philadelphia, PA, USEPA, Air and Energy Environmental Research Laboratory, Research Triangle Park, NC.

Palmiter L. and Brown I. (1989) Northwest residential infiltration study, Volume I: Analysis and results, DOE/BP-34625-1, Prepared for the Bonneville Power Admin., U.S. Dept. of Energy, Portland, OR.

Patankar S. V. (1980) *Numerical Heat Transfer and Fluid Flow,* Hemisphere Publishing, New York, NY.

Sherman M. H. (1992) Simplified modeling for infiltration and radon entry, report LBL-33962, Lawrence Berkeley National Laboratory, Berkeley, CA.

Sherman M. H., Wilson D. J., and Kiel D. E. (1984) Variability in residential air leakage, Proc. of Symposium on Measured Air Leakage Performance of Buildings, Philadelphia, PA, The American Society for Testing and Materials.

Turk B. H., Prill R. J., Fisk W. J., Grimsrud D. T., and Sextro R. G. (1991) Effectiveness of radon control techniques in fifteen homes, *J. Air Waste Mange. Assoc.* **41**, 723-734.

Turk B. H., Prill R. J., Grimsrud D. R., Moed B. A., and Sextro R. G. (1990) Characterizing the occurrence, sources and variability of radon in Pacific Northwest homes, *J. Air Waste Mange. Assoc.* **40**, 498-506.

Van der Hoven I. (1957) Power spectrum of horizontal wind speed in the frequency range from 0.0007 to 900 cycles per hour, *J. Meteor.* **14**, 160-164.

Ward D. C., Borak T. B., and Gadd M. S. (1993) Characterization of Rn-222 entry into a basement structure surrounded by low-permeability soil, *Health Phys.* **65**, 1-11.

Table 4.1. The Forchheimer term as a function of soil permeability.

Soil Permeability, k (m^2)	Forchheimer term, c ($s\ m^{-1}$)
10^{-11}	0.095
10^{-10}	0.31
10^{-9}	0.97
10^{-8}	4.0

Table 4.2. Wind conditions, basement depressurization, and air-exchange rate for the four simulation cases.

Case	*Wind Conditions*	*Basement Depressurization (Pa)*	*Air-Exchange Rate (h^{-1})*	*Wind-induced ground-surface pressures*
1	none	-11	1.5	no
2	8.3 m s^{-1} at 0°	-11	1.5	yes
3	8.3 m s^{-1} at 45°	-11	1.5	yes
4	3.6 m s^{-1} at 0°	-2.0	0.65	yes

Table 4.3. Change in soil-gas radon concentration as a result of wind. Data culled from the LBL study of houses in New Jersey, reported in Turk et al. (1991).

	Low Wind				High Wind				
House ID	*Date*	*Beginning Time*[a]	*Mean Wind* ($m\ s^{-1}$)	*Mean Soil-Gas concentration* ($kBq\ m^{-3}$)	*Date*	*Beginning Time*[a]	*Mean Wind* ($m\ s^{-1}$)	*Mean Soil-Gas concentration* ($kBq\ m^{-3}$)	*Ratio*[b]
LBL09	22 Nov. 1986	1900	0.3	300	23 Nov. 1986	0200	3.5	220	0.7
	24 Nov. 1986	0400	1.3	240	24 Nov. 1986	1300	4.6	150	0.6
	28 Nov. 1986	1900	3.6	290	29 Nov. 1986	0100	8.2	74	0.3
LBL10	9 Jan. 1987	1700	1.7	380	10 Jan. 1987	0300	5.1	150	0.4
	27 Jan. 1987	0400	3.4	290	27 Jan. 1987	1400	6.8	160	0.6
LBL14	29 Nov. 1986	0900	2.6	81	29 Nov. 1986	1400	5.5	160	2
	12 Dec. 1986	0800	3.2	93	12 Dec. 1986	1200	10	56	0.6
	16 Dec. 1986	1800	0.9	100	17 Dec. 1986	0600	6.2	54	0.5
	21 Jan. 1987	0900	1.7	100	21 Jan. 1987	1600	8.2	44	0.4
	24 Jan. 1987	1700	4.8	140	25 Jan. 1987	0200	9.8	15	0.1

[a] Beginning of two-hour averaging period.

[b] Ratio of mean soil-gas concentration under high-wind conditions to that under low-wind conditions.

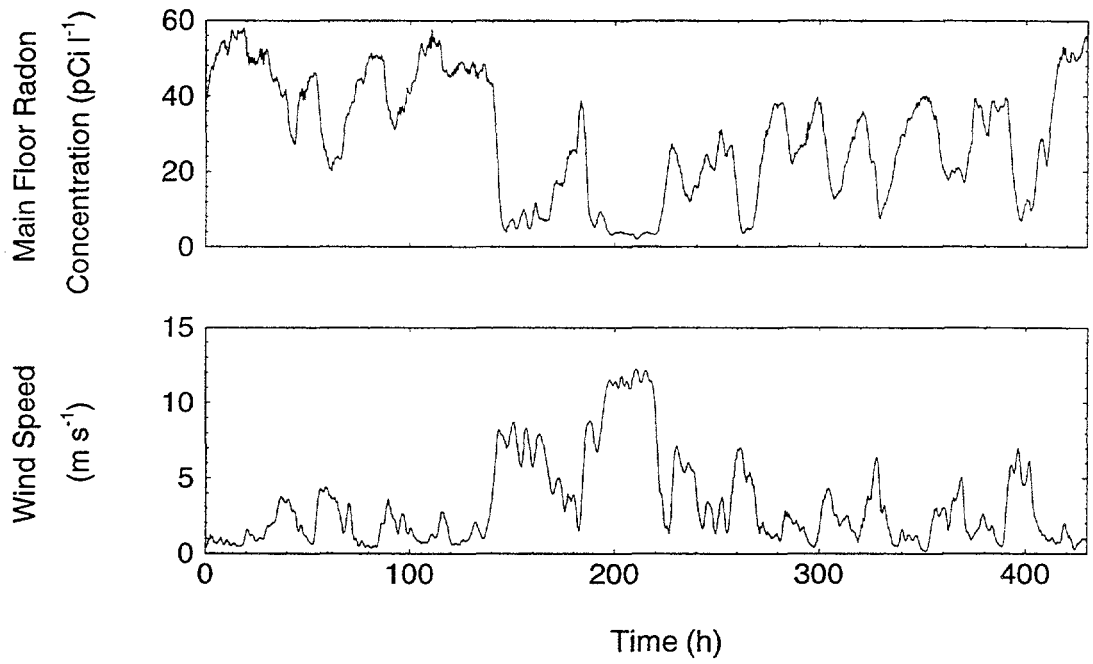

Figure 4.1. Indoor radon concentration and wind speed measured over a three-week period at ESP111 (Spokane, WA) from the study by Turk et al., (1990). Note the inverse correlation between wind speed and indoor concentration, and the magnitude of the reduction in indoor concentration during the periods of high wind speeds. The data were collected between November 23 and December 11, 1985.

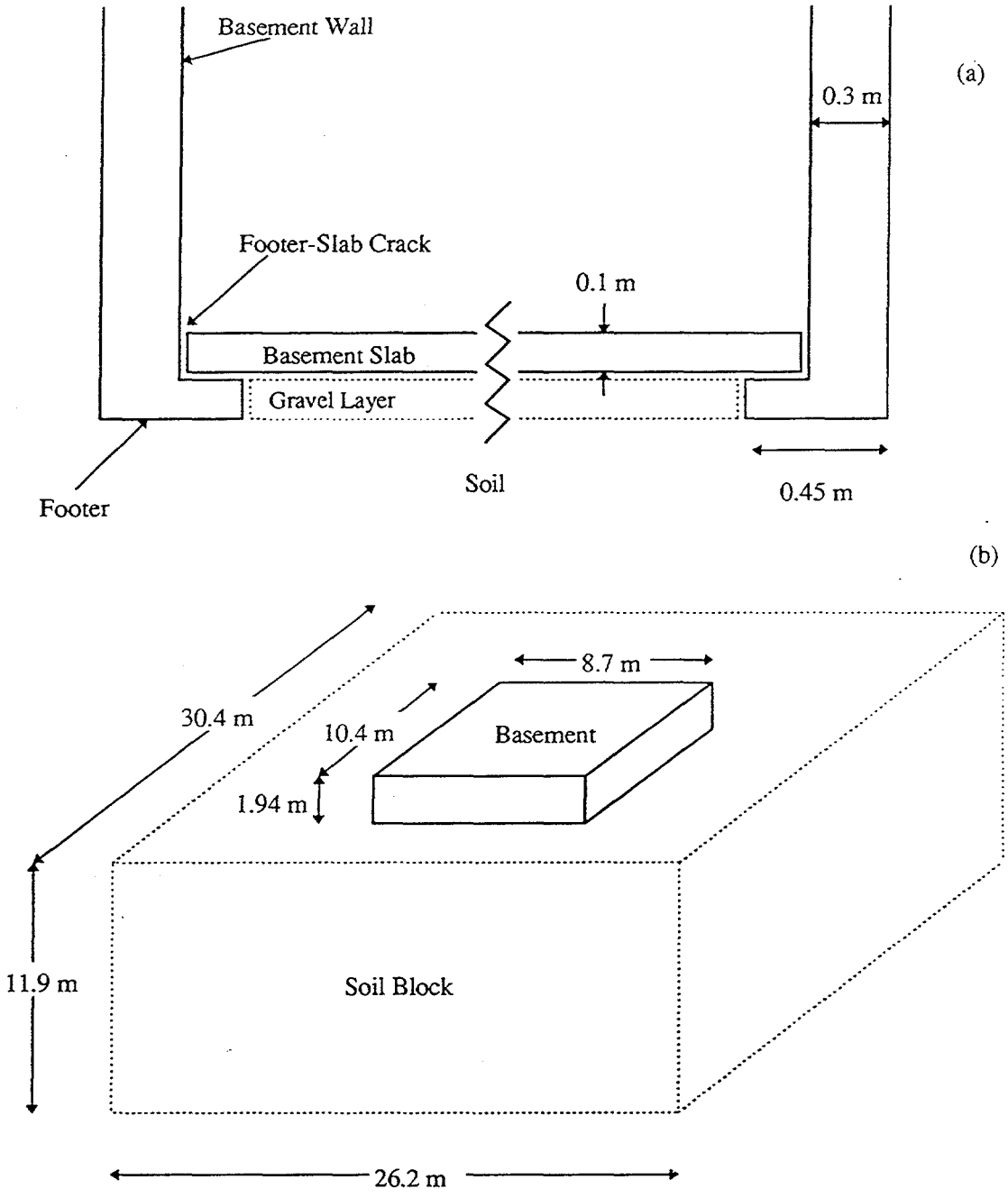

Figure 4.2. Geometry of the substructure of the house (a) and the computational space (b). The diagrams are not to scale.

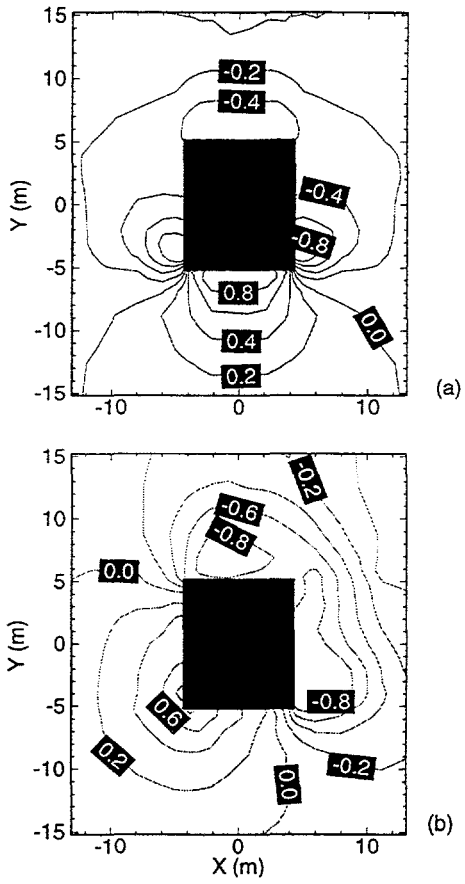

Figure 4.3. Contour plot of the ground-surface pressure coefficient (plan view) for wind incident at an angle of 0° (a) and 45° (b) to the house. The pressure coefficient is the fraction of the eave-height (3 m) dynamic pressure of the wind that is felt on the ground surface. See Chapter 3, Figure 3.5.

/bpa/windtunnel/fig4-3.lay

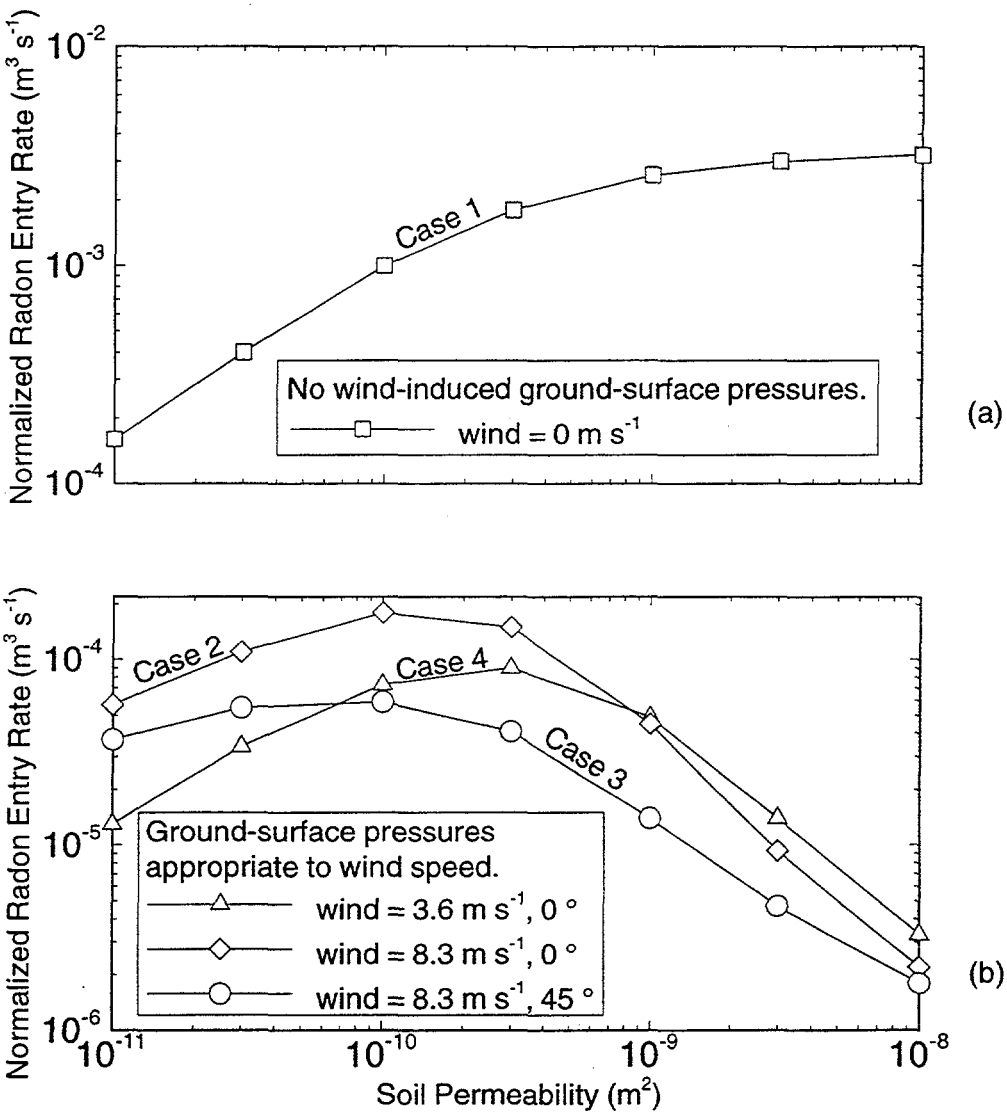

Figure 4.4. Normalized radon entry rate from soil gas into the basement as a function of soil permeability. The radon entry rate is normalized with respect to the deep-soil gas-phase radon concentration. The gravel permeability is 3×10^{-7} m^2. The basement depressurization for no wind (i.e., no wind-induced ground-surface pressures) is set at -11 Pa, for the 3.6 m s^{-1} wind it is -2.0 Pa, and for the 8.3 m s^{-1} wind it is -11 Pa. Note the different y-axis scales for Figures 4.4 (a) and 4.4 (b).

bpa/fulthouse/fig4-4.lay

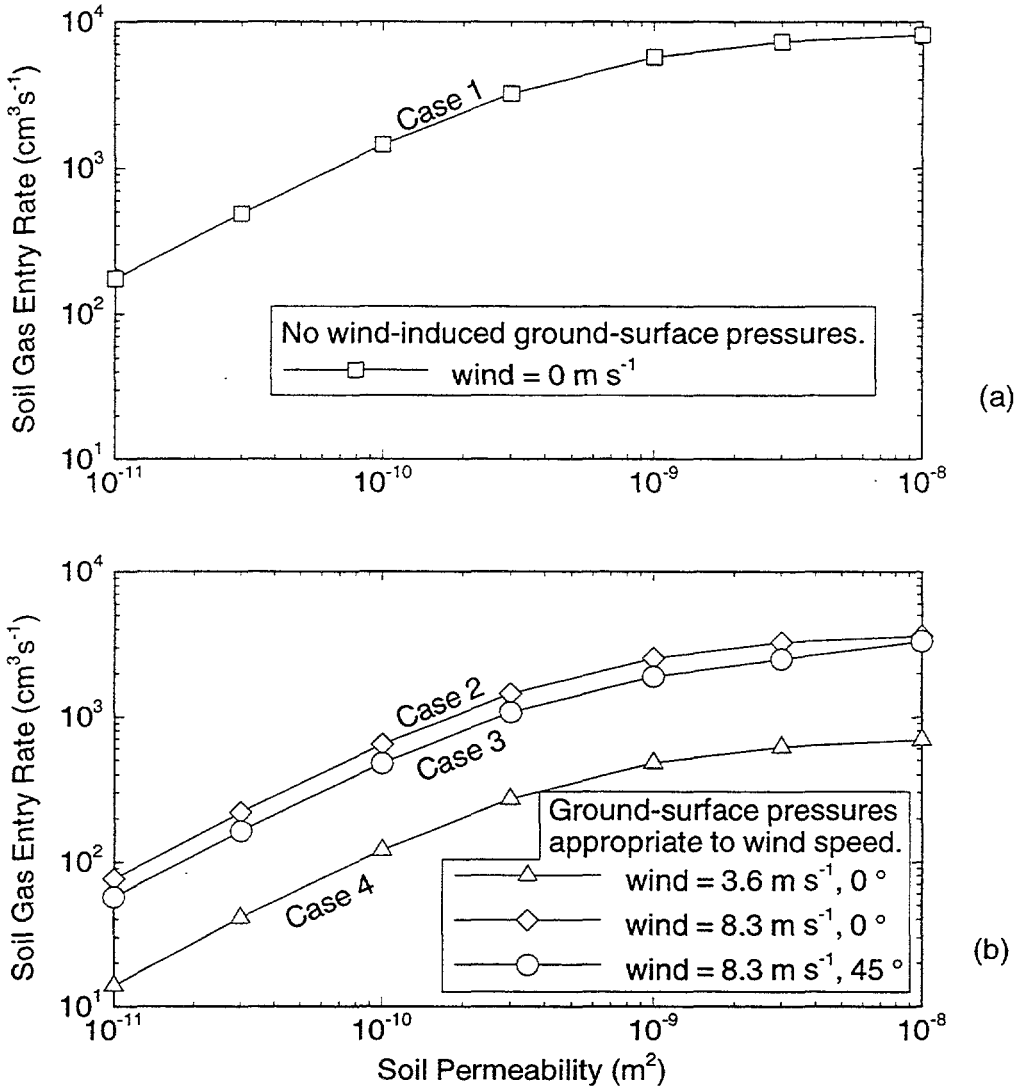

Figure 4.5. Soil-gas entry rate into the basement as a function of soil permeability. The gravel permeability is 3×10^{-7} m^2. The basement depressurization for no wind (i.e., no wind-induced ground-surface pressures) is set at -11 Pa, for the 3.6 m s^{-1} wind it is -2.0 Pa, and for the 8.3 m s^{-1} wind it is -11 Pa.

user5/riley/bpa/fullhouse/fig4-5.lay

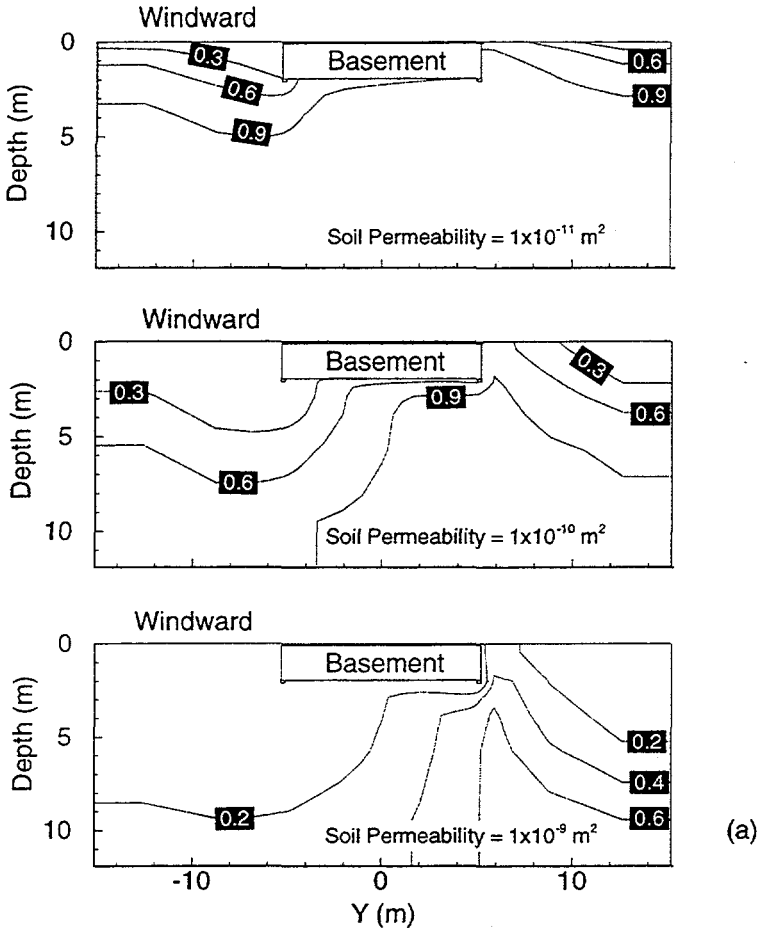

Figure 4.6. Contour plots of soil-gas radon concentration at several soil permeabilities for the case of (a) an 8.3 m s^{-1} wind and (b) no wind. The concentration is normalized with respect to the deep-soil gas-phase radon concentration. Figures represent concentrations in a vertical plane bisecting the basement parallel to the long side of the house and the wind. As the soil permeability increases, the radon concentration in the soil gas adjacent to the slab decreases. Note the magnitude of the reduction in soil-gas radon concentration for the case with wind compared to the case with no wind. The basement depressurization is -11 Pa for both cases.

/user5/riley/bpa/fullhouse/fig4-6a.lay

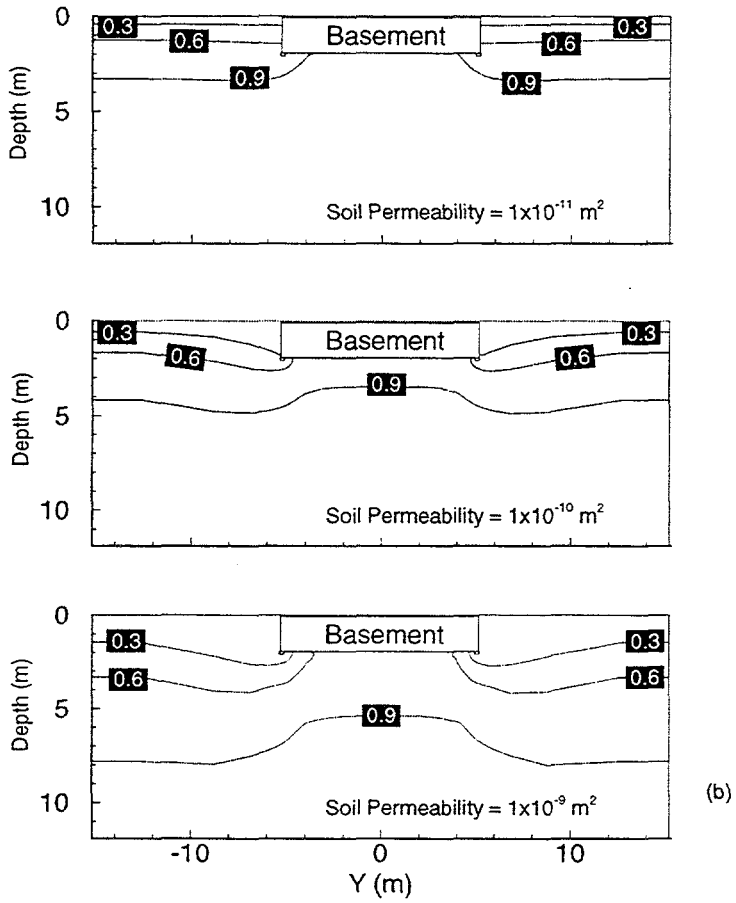

Figure 4.6. Continued.

/bpa/fullhouse/fig4-6b.lay

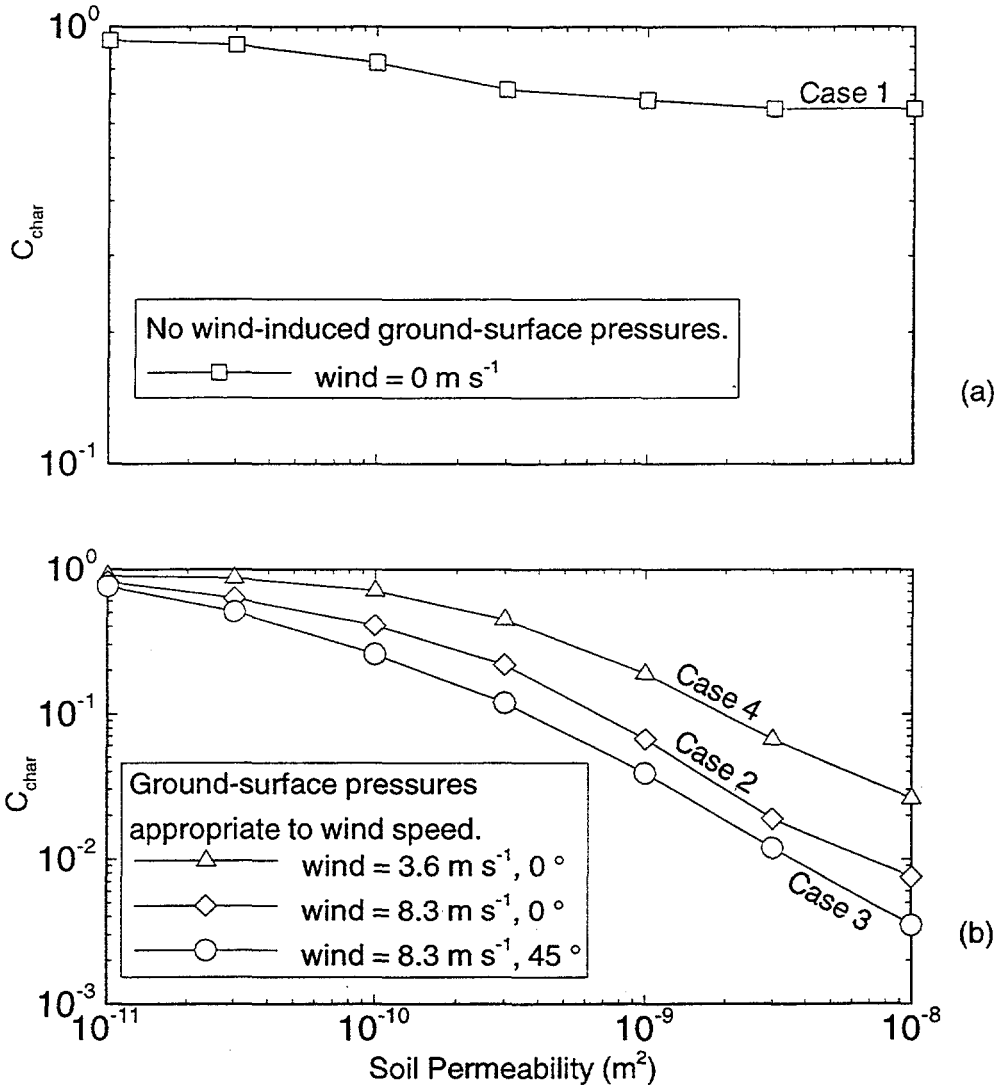

Figure 4.7. Average radon soil-gas concentration at a horizontal plane located at the bottom of the footers, and bounded by the footers. The concentration is normalized with respect to the deep-soil gas-phase radon concentration. The basement depressurization for no wind (i.e., no wind-induced ground-surface pressures) is set at -11 Pa, for the 3.6 m s^{-1} wind it is -2.0 Pa, and for the 8.3 m s^{-1} wind it is -11 Pa.

/boa/fulthouse/fig4-7.fav

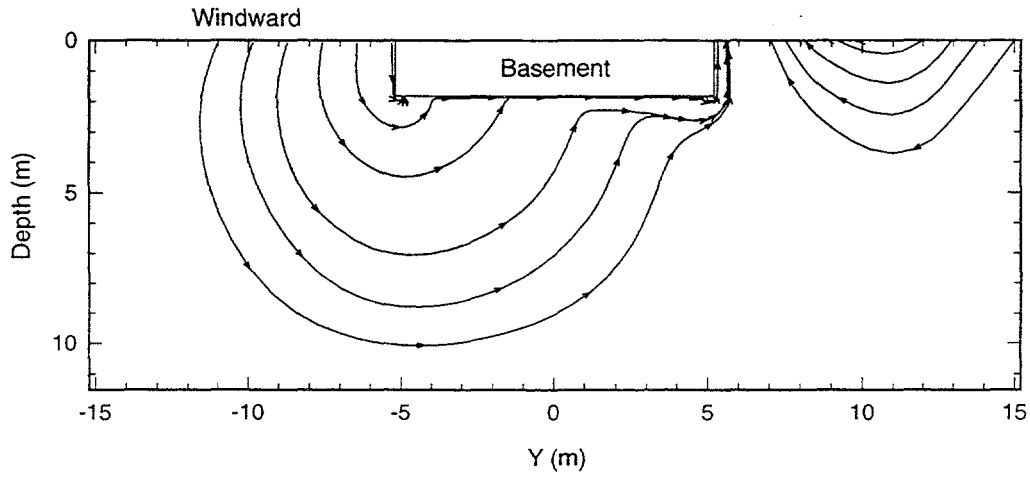

Figure 4.8. Streamlines of gas flow through the soil and gravel layer. The wind speed is 8.3 m s^{-1}, the soil permeability is $3x10^{-9}$ m^2, and the gravel permeability is $3x10^{-7}$ m^2.

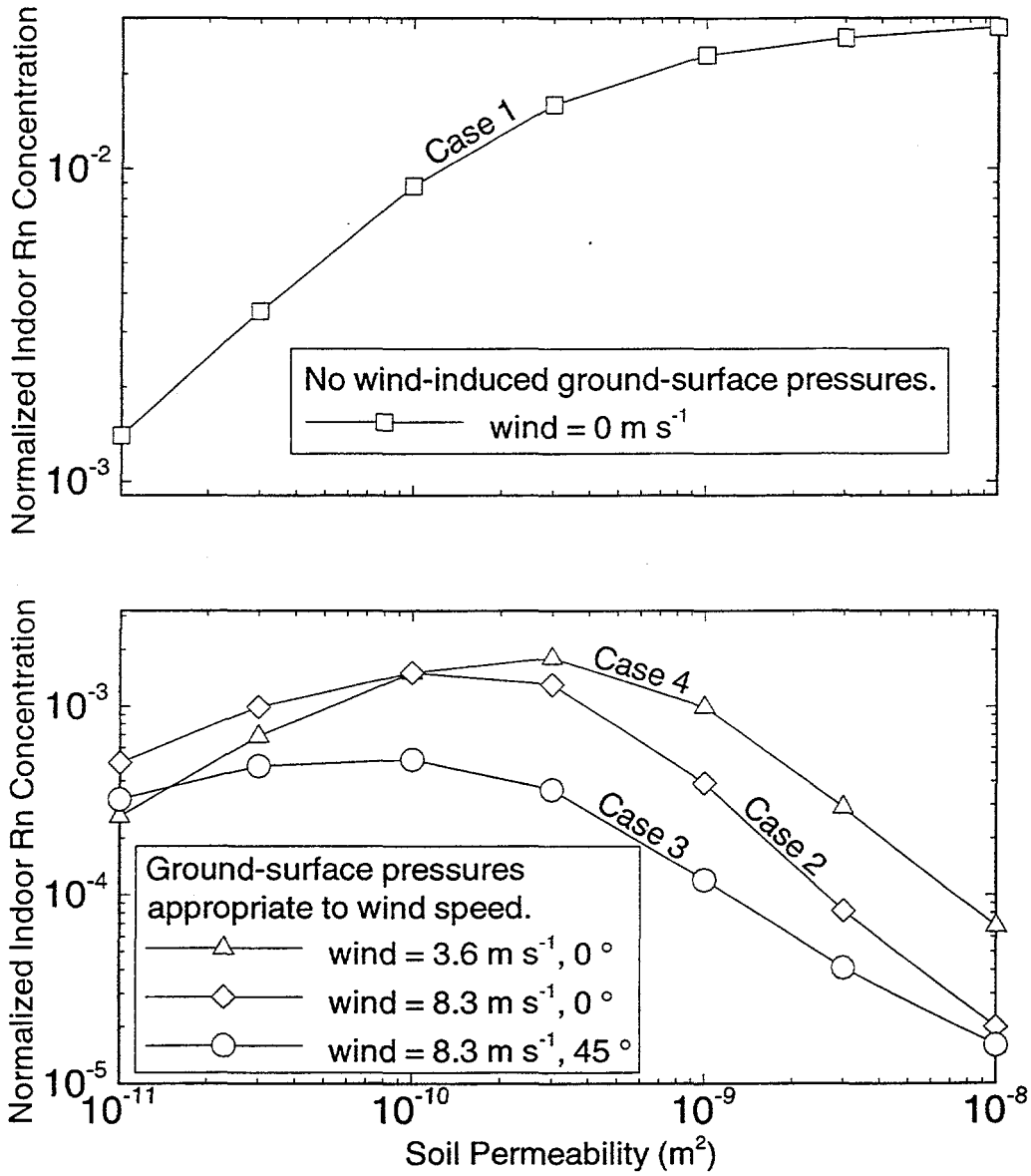

Figure 4.9. Normalized indoor radon concentration as a function of wind speed and soil permeability. The basement depressurization for no wind (i.e. no wind-induced ground-surface pressures) is set at -11 Pa, for the 3.6 m s^{-1} wind it is -2.0 Pa, and for the 8.3 m s^{-1} wind it is -11 Pa.

user5/riley/bpa/fullhouse/fig4-9.lay

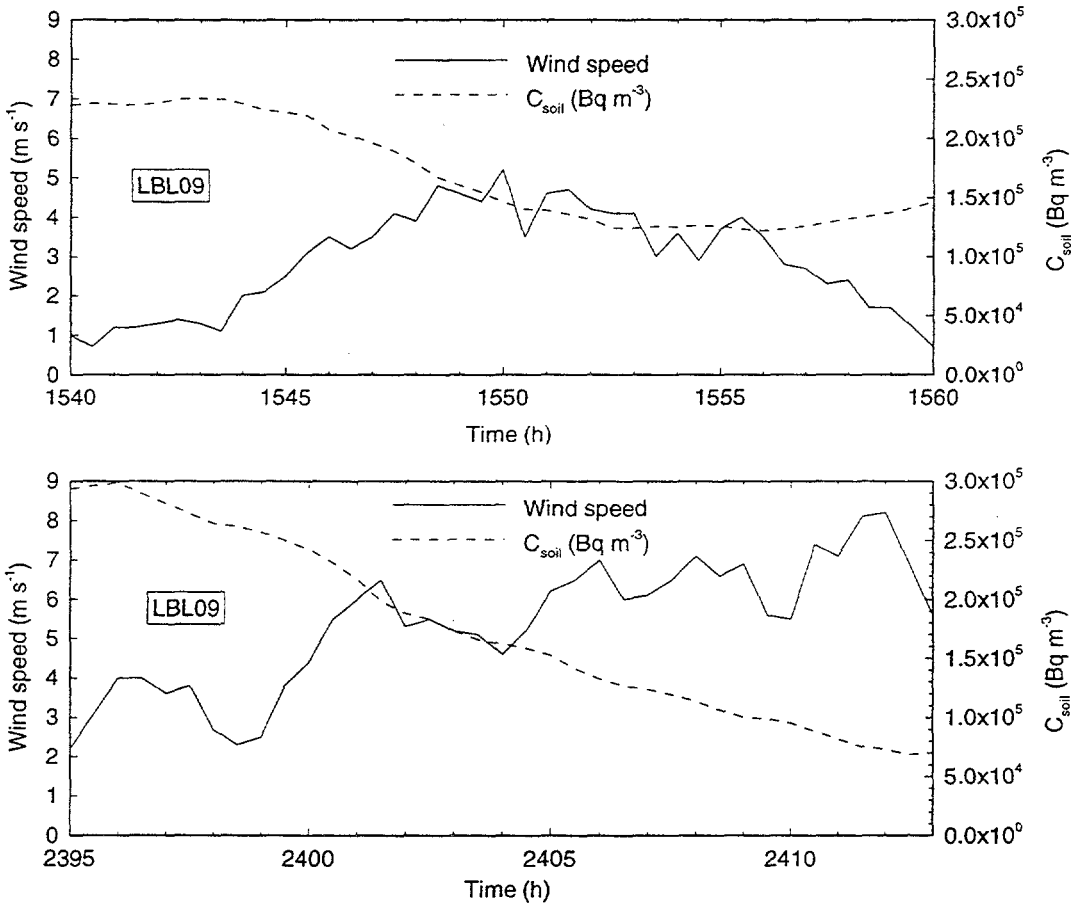

Figure 4.10. Wind speed and soil-gas radon concentration for two time periods at house LBL09 (Morristown, NJ) (Turk et al., 1991). Wind-driven soil-gas flow flushes radon from the area adjacent to the house.

CHAPTER 5

THE DEVELOPMENT AND VALIDATION OF START: A TRANSIENT, FINITE-DIFFERENCE, SOIL-GAS AND RADON TRANSPORT MODEL

5.1 Abstract

This chapter describes the development and validation of START, a transient, three-dimensional, non-Darcy, finite-difference model designed to simulate soil-gas and radon transport in the soil surrounding a building. The methods used to discretize and solve the equations governing soil-gas and radon flow are presented. Boundary conditions can be prescribed to examine the effects on radon transport of fluctuating winds, fluctuating barometric pressures, active or passive mitigation systems, and steady basement depressurizations.

We compare START's simulation predictions to four analytical solutions of one-dimensional flow through a soil column and experimental results from a well-characterized basement structure. The four analytical solutions correspond to four sets of boundary conditions chosen to test various components of START's solution technique: (1) the transient pressure field in a soil column with one end of the column subject to a sinusoidal pressure and the other end held at a constant pressure; (2) the convergence to a steady-state solution of the concentration profile in a soil column for various Peclet numbers; (3) the transient solution to the concentration profile in a soil column with no radon source or radioactive decay and a constant pressure drop across

the column (the Ogata solution); and (4) the transient solution to the concentration profile in a soil column with radioactive decay, no radon source, and a constant pressure drop across the column. We also compare START's simulation predictions to experimental measurements of soil-gas and radon entry into an experimental structure. The START simulations match both the analytical solutions and experimental data well. Because of computational limitations, we cannot use START directly to simulate radon entry into buildings in response to time-varying winds. Instead, we employ START as a preprocessor to generate unit-step responses for the RapidSTART model (see Chapters 6 and 7).

5.2 Nomenclature

A , B	constants (-)
c	Forchheimer term (s m^{-1})
c_c	characteristic Forchheimer term (s m^{-1})
C	soil-gas radon concentration (Bq m^{-3})
$\overline{C}$	Laplace transform of $C(x,t)$ with respect to time
C_c	characteristic deep-soil radon concentration (Bq m^{-3})
D	bulk diffusion constant for radon in soil gas (m^2 s^{-1})
D_c	characteristic bulk diffusion constant for radon in the soil-gas (m^2 s^{-1})
f, F	arbitrary functions of time and the Laplace variable, respectively (-)
g	acceleration of gravity (9.8 m s^{-2})
i , **j**, **k**	unit vectors in the three Cartesian directions (m)
k	soil permeability (m^2)
k_c	characteristic soil permeability (m^2)
l	length of the column (-)
$\mathcal{L}^{-1}$	inverse Laplace function (-)
L_c	characteristic length (m)
m	constant (-)
M	molecular weight (kg m^{-3})
n	dummy variable of summation (-)

N_c	nondimensionalizing parameter (-)
p	soil-gas pressure (Pa)
Pe_G	grid Peclet number (-)
p_A	reference atmospheric pressure (Pa)
p_c	characteristic gage pressure (Pa)
p_G	disturbance, or gage, pressure (Pa)
q	Laplace variable corresponding to t (-)
r	Laplace variable corresponding to x (-)
R	universal gas constant (8.314 J mol^{-1} K^{-1})
r_1, r_2	roots of the Laplace transformed equation (-)
s	linear transform of the Laplace variable q
S	production rate of radon in the soil pores (Bq m^{-3} s^{-1})
S_c	characteristic production rate of radon in the soil pores (Bq m^{-3} s^{-1})
t	time (s)
t'	inverse Laplace variable corresponding to s (-)
T	air temperature (K)
t_c	characteristic time (s)
$\vec{u}$	Darcy velocity (m s^{-1})
u, v, w	components of the Darcy velocity $\vec{u}$ (m s^{-1})
u_c	characteristic soil-gas velocity (m s^{-1})

Δx	grid spacing (-)
x, y, z	coordinate axis positions (m)

Greek letters

α	constant (-)
δ	pressure diffusivity (-)
ε	air-filled porosity (-)
λ	dummy variable of integration (-)
λ_{Rn}	radon decay constant (2.098×10^{-6} s^{-1})
κ	constant (-)
ρ	air density (kg m^{-3})
μ	dynamic viscosity (kg m^{-1} s^{-1})
μ_c	characteristic dynamic viscosity (kg m^{-1} s^{-1})
ω	frequency of the varying pressure boundary condition (-)
$\vec{\nabla}$	gradient operator (m^{-1})

Notes:
1. (-) indicates a nondimensional variable.
2. We use dimensional and nondimensional versions of many of the variables in this chapter; the text makes the distinction clear.
3. The appendix (Section 5.8) has a nomenclature table for variables that appear solely in that section.

5.3 Introduction

Three-dimensional numerical models of soil-gas and radon transport can be powerful tools for exploring the relationships between radon entry into buildings and environmental and structural factors. In the past, the majority of these transport models have focused on steady-state conditions. However, many of the environmental factors known to be important in steady state have strong fluctuating components. Wind fits this profile; the power in high frequency wind-speed fluctuations can be a significant fraction of wind's total power. Also, the wind direction can vary over a wide range on relatively short time scales. Until this work, however, no simulation tool had been developed to model the impacts of fluctuating winds on radon entry. We therefore developed START, a three-dimensional, finite-difference, transient soil-gas and radon transport model. In this chapter, we present the equations used to compute the soil-gas pressure and concentration fields, and analytical and experimental validation tests of the model.

The earliest numerical models of soil-gas and radon entry into houses simulated only advective transport in a uniform, isotropic soil (DSMA Atcon Ltd., 1983; Eaton and Scott, 1984; DSMA Atcon Ltd., 1985). Loureiro (1990) developed a steady-state model that allowed for variable soil characteristics and radon diffusion. Bonnefous et al. (1992), in their study of active mitigation systems, extended Loureiro's model by including non-Darcy flow. In an experimental study, the model accurately predicted the pressure field in the soil surrounding a real house equipped with an operating SSV

system (Bonnefous, 1994). Revzan et al. (1991) built a two-dimensional, steady model based on Darcy's law that takes advantage of geometrical symmetry to significantly reduce the model's complexity and runtime. RN3D, a transient finite-element model developed by Holford et al. (1993), can also be used to simulate two-, and simple three-dimensional geometries. Gadgil (1992) presents a review of existing models of radon entry, and discusses their strengths and limitations.

Section 5.4 describes the equations and methods START employs to simulate soil-gas and radon transport in soils surrounding a building. The radon entry rate into the building is determined in three steps. First, the model determines the soil-gas pressure and velocity fields. Second, using the velocity field, the soil-gas radon concentration field is computed. Third, START calculates the radon entry rate by integrating the flux of radon into the footer-slab crack around the periphery of the basement. Sections 5.4.1 and 5.4.2 present the equations governing the subsurface transport of soil gas around the house. Section 5.4.3 describes the radon mass balance equation, which is used to determine the soil-gas radon concentration field. An appendix to this chapter (Section 5.8) presents the methods used to numerically solve these transport equations using a finite-difference approach.

To validate START, we compare simulation predictions to four analytical solutions of soil-gas and radon flow through a one-dimensional soil column. Section 5.5.1 presents a comparison of the simulated and analytical solutions of the soil-gas pressure field in a soil column subject to a periodically fluctuating pressure boundary condition. Sections 5.5.2 - 5.5.4 present validation tests of START's transient

concentration field solution. The first of these tests verifies that START converges to the correct steady-state concentration profile in the soil column. The second test compares START predictions to the Ogata solution. Third, we derive the transient analytical solution of radon flow through a soil column including radioactive decay, a constant pressure drop across the column, and no radon source. These four analytical tests are performed over a range of parameters that bound conditions found around typical single-family homes.

As a final validation test, Section 5.6 presents a comparison between START's simulation predictions and experimental measurements from the Small Structures Facility in the Santa Cruz Mountains (Robinson and Sextro, 1995). The experiment considered here simultaneously measured the fluctuating atmospheric pressure and the resulting soil-gas and radon entry rates into the basement.

The complexity of the physical system and the required spatial and temporal discretization make the START simulations of wind-induced radon entry very computationally intensive. To simulate radon entry in response to transient winds, START is used to compute the soil-gas pressure field's unit-step response. RapidSTART, the novel simulation technique described in Chapters 6 and 7, uses this unit-step response as input.

5.4 Soil-Gas and Radon Flow Equations

This section describes the equations used to represent transient soil-gas and radon flow in the soil around a house. START first computes the soil-gas pressure and

velocity fields by combining the continuity and Darcy-Forchheimer equations with user-specified pressure boundary conditions. The radon mass balance equation and the soil-gas velocity field define the soil-gas radon concentration field.

5.4.1 Continuity Equation

The continuity equation expresses fluid (i.e., soil-gas) mass conservation in the soil (Loureiro, 1987)

$$\varepsilon \frac{\partial \rho}{\partial t} + \vec{\nabla} \bullet (\rho \vec{u}) = 0 \tag{5.1}$$

where t is time (s); ε is the constant air-filled porosity (-); ρ is the air density (kg m^{-3}); and $\vec{\nabla}$ is the gradient operator:

$$\vec{\nabla} = \frac{\partial}{\partial x}\mathbf{i} + \frac{\partial}{\partial y}\mathbf{j} + \frac{\partial}{\partial z}\mathbf{k} \tag{5.2}$$

where x, y, and z are positions in the three coordinate directions (m); and $\mathbf{i}$, $\mathbf{j}$, and $\mathbf{k}$ are unit vectors in the three coordinate directions.

The ideal gas law accurately links the soil-gas density and pressure under typical environmental conditions:

$$\rho = \frac{p}{RT} M \tag{5.3}$$

where p is the soil-gas pressure (Pa), R is the universal gas constant (8.314 J mol^{-1} K^{-1}), M is the molecular weight of air (kg m^{-3}), and T is the air temperature (K). We can represent the soil-gas pressure as

$$p = p_A + p_G + \rho g z \tag{5.4}$$

where p_A is the constant reference atmospheric pressure (Pa), p_G is the disturbance, or gage, pressure (Pa), and $\rho g z$ is the hydrostatic pressure (Pa). Substituting equations (5.3) and (5.4) into equation (5.1) gives

$$\varepsilon \frac{\partial (p_A + p_G + \rho g z)}{\partial t} + \vec{\nabla} \bullet \left[(p_A + p_G + \rho g z)\vec{u} \right] = 0 \tag{5.5}$$

To simplify the first term in equation (5.5) we assume the reference pressure, p_A, remains constant in time, so $\frac{\partial p_A}{\partial t} = 0$. Also, because composition and temperature change slowly, the time rate of change of the hydrostatic pressure is much less than the time rate of change of the disturbance pressure. The second term in equation (5.5) can be simplified by assuming, first, that p_A (~ 10^5 Pa) is much larger than either p_G or $\rho g z$. The maximum expected value of p_G, which could occur under high wind conditions, is 50 Pa. The maximum expected value of $\rho g z$ in this system is 100 Pa. Second, p_A is constant in space, and can therefore be moved outside of the gradient operator. With these simplifications, equation (5.5) can be rewritten as

$$\varepsilon \frac{\partial p_G}{\partial t} + p_A \vec{\nabla} \bullet \vec{u} = 0 \tag{5.6}$$

Equation (5.6) can be expanded as

$$\varepsilon \frac{\partial p_G}{\partial t} + p_A \left\{ \frac{\partial u}{\partial x} + \frac{\partial v}{\partial y} + \frac{\partial w}{\partial z} \right\} = 0 \tag{5.7}$$

where u, v, and w are the three components of the Darcy velocity $\vec{u}$ (m s^{-1}). The following substitutions nondimensionalize equation (5.7):

$$p'_G = \frac{p_G}{p_c} \tag{5.8}$$

$$p'_A = \frac{p_A}{p_c} \tag{5.9}$$

$$t' = \frac{t}{t_c} \tag{5.10}$$

$$x' = \frac{x}{L_c} \tag{5.11}$$

$$y' = \frac{y}{L_c} \tag{5.12}$$

$$z' = \frac{z}{L_c} \tag{5.13}$$

$$\vec{u}' = \frac{\vec{u}}{u_c} \tag{5.14}$$

where the superscript $'$ indicates the corresponding nondimensional variable, and the subscript c indicates a nondimensionalizing parameter. This set of nondimensionalizing parameters yields a convenient form of the governing equation, even though it exceeds the minimum required by the Buckingham Pi Theorem (i.e., three parameters spanning {M, L, T}). Table 5.1 gives the values for these nondimensionalizing parameters.

Substituting equations (5.8) - (5.14) into equation (5.7) yields

$$\varepsilon \frac{\partial p_G'}{\partial t'} + p_A' \left\{ \frac{\partial u'}{\partial x'} + \frac{\partial v'}{\partial y'} + \frac{\partial w'}{\partial z'} \right\} = 0 \tag{5.15}$$

To simplify the notation, we drop the superscripts in equation (5.15) for the remainder of this dissertation, although the terms remain nondimensional.

5.4.2 The Darcy-Forchheimer Equation

To compute the pressure field in the soil surrounding the house, the soil-gas velocities must be related to the soil-gas pressures. Since important cases exist (e.g.,

SSV system operation) where Darcy's law fails, we use the Darcy-Forchheimer equation (Forchheimer, 1901; Mele and Joseph, 1985) to establish this relationship

$$\vec{\nabla} p = -\frac{\mu}{k}(1 + c|\vec{u}|)\vec{u} + \rho g \mathbf{k} \tag{5.16}$$

where μ is the dynamic viscosity (kg m^{-1} s^{-1}), k is the soil permeability (m^2), $\mathbf{k}$ is a unit vector pointing in the direction of gravity, and c is the Forchheimer term (s m^{-1}). Table 4.1 presents the Forchheimer terms used here as a function of the soil permeability. Substituting equation (5.4) into equation (5.16) and recognizing that p_A is constant in space gives

$$\vec{\nabla} p_G = -\frac{\mu}{k}(1 + c|\vec{u}|)\vec{u} \tag{5.17}$$

Equation (5.17) can be written in dimensionless form

$$\vec{\nabla}' p_G' = -\frac{N_c \mu'}{k'}(1 + c'|\vec{u}'|)\vec{u}' \tag{5.18}$$

where

$$N_c = \frac{L_c u_c \mu_c}{k_c p_c} \tag{5.19}$$

and the nondimensionalizing parameters are given in Table 5.1. The new dimensionless variables are

$$\vec{\nabla}' = L_c \vec{\nabla} \tag{5.20}$$

$$\mu' = \frac{\mu}{\mu_c} \tag{5.21}$$

$$k' = \frac{k}{k_c} \tag{5.22}$$

$$c' = \frac{c}{c_c} \tag{5.23}$$

To simplify the notation, the $'$ superscript will be dropped from the terms in equation (5.18), although the equation remains nondimensional.

5.4.3 The Radon Mass Balance Equation

The mass balance equation for radon in the soil gas is (Loureiro, 1987)

$$\frac{\partial}{\partial t}(C\varepsilon) = \vec{\nabla} \bullet (D\vec{\nabla}C) - \vec{\nabla} \bullet (\vec{u}C) + \varepsilon(S - \lambda_{Rn}C) \tag{5.24}$$

where C is the soil-gas radon concentration (Bq m^{-3}), S is the radon source term (Bq m^{-3} s^{-1}), and λ_{Rn} is the radon decay constant (2.098×10^{-6} s^{-1}). D is the bulk diffusion constant for radon in soil gas (m^2 s^{-1}), and represents the ratio of the total radon flux (mass per total cross-sectional area) to the pore concentration gradient (over

the actual distance between two points in the soil), divided by the tortuosity. In addition to the parameters previously introduced in Table 5.1, the following parameters are used to nondimensionalize equation (5.24):

$$S' = \frac{S}{S_c} \tag{5.25}$$

$$C' = \frac{C}{C_c} \tag{5.26}$$

$$D' = \frac{D}{D_c} \tag{5.27}$$

The values of the nondimensionalizing parameters are given in Table 5.1.

Applying equations (5.10) - (5.14) and (5.25) - (5.27) to equation (5.24) yields

$$\frac{\partial}{\partial t'}(C'\varepsilon) = \vec{\nabla}' \bullet (D'\vec{\nabla}'C') - \vec{\nabla}' \bullet (\vec{u}'C') + \varepsilon(S' - C') \tag{5.28}$$

where $\vec{\nabla}'$ is the nondimensional gradient operator

$$\vec{\nabla}' = \frac{\partial}{\partial x'}\mathbf{i} + \frac{\partial}{\partial y'}\mathbf{j} + \frac{\partial}{\partial z'}\mathbf{k} \tag{5.29}$$

To simplify the notation, the $'$ superscript will be dropped from the terms in the radon material balance equation, although the equation remains nondimensional.

5.5 Validation of START

At the most general level, validating a numerical model involves two stages. First, the model should be able to reproduce analytical solutions to a range of problems representative of potential applications. Many factors can affect a soil-gas transport model's accuracy at this stage: the resolution of the spatial and temporal discretization, the approximations made in discretizing the derivatives in the equations (i.e., the Taylor series expansions), the linearization of nonlinear terms, and the methods chosen to approximate variable profiles across control volumes (e.g., upwind schemes).

Secondly, the model's predictions should match results from experiments that mimic as closely as possible scenarios under which the model will be applied. In the context of soil-gas and radon transport modeling, several levels of validation are commonly employed. For example, comparisons to soil-column experiments, small-scale experimental structures, and real house experiments provide successively stricter tests for the model. Many factors can affect the model's predictive ability in these simulations: the accuracy of the characterization of system properties (e.g., soil permeability, porosity, or footer-slab crack properties), the accuracy of the geometrical representation of the structure, and computer resource limitations that preclude inclusion of all the details of the system.

The criteria for success at either of these stages should depend on the intended application of the model. In general, though, the requirements for the first stage (analytical tests) are much stricter than for the second (experimental tests). Without

some success matching analytical solutions, any success at the experimental validation stage is likely serendipitous.

If the model is to be used for prediction in a specific situation, the criteria for success at the experimental validation stage must be fairly stringent. However, if the model is to be used in an exploratory fashion, that is, to elucidate qualitative features of the problem, the simulation results need not precisely match measurements from specific experiments. Capturing the qualitative features of the experimental results may suffice (again, depending on the context). A good example of this type of modeling application can be seen in the preliminary design of a passive radon mitigation system (Fisk et al., 1995). The investigation focused on very broad questions, and therefore did not require the use of a model that had been tested and validated at the particular house under consideration. This dissertation uses the START and RapidSTART models in a similar context by examining general features of wind's interactions with soils and buildings. As we show, however, START and RapidSTART perform very well at both the analytical and experimental validation stages. In Section 5.5.1 we present four comparisons of START's predictions to analytical solutions. Section 5.5.2 describes a comparison of START predictions to results from an experiment at the Small Structures Facility. We label these tests as "validation scenarios" 1 - 5, as summarized in Table 5.2.

5.5.1 Analytical Validation of START

This section presents comparisons between START simulation predictions and four analytical solutions of soil-gas and radon flow through a one-dimensional soil column. Because general analytical solutions do not exist for the soil-gas flow field when the soil-gas pressure and velocity are not linearly related, we have assumed Darcy flow conditions for the solutions presented here. This assumption does not represent a significant restriction, since the soil-gas velocity field established in the presence of wind will be within the Darcy regime throughout the soil block and gravel layer.

The soil-gas pressure and velocity fields can be represented by combining the continuity equation (equation (5.15)) with Darcy's law to give (Garbesi, 1994)

$$\frac{\partial p_G}{\partial t} = \delta \frac{\partial^2 p_G}{\partial x^2} \tag{5.30}$$

where $\delta = \frac{k p_A}{\varepsilon \mu}$. The parameter δ represents a pressure diffusivity, and will be used later to define a characteristic time for a pressure pulse to travel through the soil block.

5.5.1.1 Pressure Field Validation (Validation Scenario 1)

START's pressure field solution was tested by comparing simulation results to analytical solutions of the soil-gas pressure field in a soil column subject to a sinusoidal pressure at one end and constant pressure at the other end. For this scenario, the boundary and initial conditions for equation (5.30) are

$$p_G(0,t) = \sin(\omega t) \qquad t > 0 \tag{5.31}$$

$$p_G(l,t) = 0 \qquad t > 0 \tag{5.32}$$

$$p_G(x,0) = 0 \qquad 0 \le x \le l \tag{5.33}$$

where $p_G(x,t)$ is the disturbance pressure at position x and time t, l is the length of the column, and ω is the frequency of the fluctuating pressure boundary condition. For the validation tests presented the pressure at $x = 0$ is driven at a frequency of 0.105 s^{-1} (equivalent to a period of 60 s), and l is 2 m.

Carslaw and Jaeger (1959, page 104) give the solution to equation (5.30), with the boundary conditions specified by equations (5.31) through (5.33), as

$$p_G(x,t) = \frac{2\delta\pi}{l^2}\sum_{n=1}^{\infty} n \exp\left(-\frac{\delta n^2\pi^2 t}{l^2}\right)\sin\left(\frac{n\pi x}{l}\right)\int_0^t \exp\left(\frac{\delta n^2\pi^2\lambda}{l^2}\right)\sin(\omega\lambda)d\lambda \tag{5.34}$$

where n is a dummy variable of summation, and λ is a dummy variable of integration.

START simulation results were compared to this analytical solution at soil permeabilities of 10^{-9}, 10^{-11}, and 10^{-13} m^2. Figures 5.1 - 5.3 show the pressure profile in the column and the corresponding error in the numerical solution. All three simulations use a 1 s time step.

The pressure at a point in the soil column 0.375 m from the fluctuating end was also used as a comparison for evaluating the pressure field calculated by START.

Figures 5.4 and 5.5 present this comparison for soil permeabilities of 10^{-8} and 10^{-12} m^2, respectively. Although difficult to distinguish, each figure presents the analytical and START solutions for the soil-gas pressure as a function of time. START matched the analytical solutions very well in each of these tests.

5.5.1.2 Steady-State Convergence Verification (Validation Scenario 2)

This section presents a test to determine whether START converges to the correct steady-state concentration field for a constant soil-gas flow through the soil column. The simulations begin with initial conditions of no soil-gas flow and no soil-gas radon throughout the column. Subsequently, both generation and decay of radon occur within the soil column. At time $t = 0$ the pressure drop across the column is raised to a specified value. START simulates the transient response of the system until the radon concentration field reaches steady state. The steady-state concentration profile computed by START is compared to the steady-state analytical solution.

The tests are performed over a range of pressure drops across the column that generate realistic grid Peclet numbers, Pe_G (-), defined as

$$Pe_G = \frac{u\Delta x}{D} \tag{5.35}$$

where Δx is the grid spacing (m) in the column. The grid Peclet number indicates the relative importance of radon transport via advection and diffusion. Testing START

over a range of Pe_G demonstrates the robustness of the radon concentration solution procedure.

The nondimensional steady-state radon mass-balance equation (refer to equation (5.28))

$$\vec{\nabla} \cdot (D\vec{\nabla}C) - \vec{\nabla} \cdot (\vec{u}C) + \varepsilon(S - C) = 0 \tag{5.36}$$

defines the steady-state analytical radon concentration field. The boundary and initial conditions for the START simulations and analytical solutions are

$$C(0,t) = 0 \qquad t > 0 \tag{5.37}$$

$$\frac{\partial C(\infty,t)}{\partial x} = 0 \qquad t > 0 \tag{5.38}$$

$$C(x,0) = 0 \qquad 0 \le x \le \infty \tag{5.39}$$

where $C(x,t)$ is the nondimensional soil-gas radon concentration at the position x and time t. With the boundary conditions given by equations (5.37) and (5.38), equation (5.36) is solved to give the steady-state analytical solution

$$C(x,\infty) = S\left(1 - e^{mx}\right) \tag{5.40}$$

where

$$m = \frac{u - \sqrt{u^2 + 4D\varepsilon}}{2D} \tag{5.41}$$

For the START simulations, the column is taken to be 10 m long and the soil permeability is 10^{-11} m^2. This column length guarantees that the boundary condition described by equation (5.38) is effectively satisfied. Grid Peclet numbers of 0, 0.22, and 1.1 define the soil-gas velocity through the column for the three simulations. After the pressure boundary conditions were established, the concentration field grew from zero to the steady-state results shown in Figure 5.6. START matched the analytical solutions very well for all three flow conditions.

5.5.1.3 Comparison to the Ogata Solution (Validation Scenario 3)

The Ogata (1970) solution refers to the transient concentration profile of a non-radioactive, chemically non-reactive contaminant in an infinitely long soil column. The following conditions apply: no contaminant source within the soil, no contaminant initially in the soil column, a constant source of contaminant at the inlet, and a steady soil-gas velocity. Under these conditions, the nondimensional transient mass balance equation (equation (5.28)) becomes

$$\frac{\partial}{\partial t}(\varepsilon C) = D\frac{\partial^2 C}{\partial x^2} - u\frac{\partial C}{\partial x} \tag{5.42}$$

and the boundary and initial conditions are

$$C(0,t) = 1 \qquad t > 0 \tag{5.43}$$

$$C(\infty,t) = 0 \qquad t > 0 \tag{5.44}$$

$$C(x,0) = 0 \qquad 0 \le x \le \infty \tag{5.45}$$

The analytical solution to equation (5.42) subject to these boundary conditions is

$$C(x,t) = \frac{1}{2}\left[\operatorname{erfc}\left(\frac{x-ut}{2\sqrt{Dt}}\right) + \exp\left(\frac{ux}{D}\right)\operatorname{erfc}\left(\frac{x+ut}{2\sqrt{Dt}}\right)\right] \tag{5.46}$$

Figure 5.7 presents comparisons between START's simulations and the Ogata solution for the case of a 5 Pa pressure difference imposed across a 30 m long column, a soil permeability of 10^{-11} m^2, and a time step of 10 hours. START's predictions matched the analytical solutions very well.

5.5.1.4 Ogata Solution Plus Radioactive Decay (Validation Scenario 4)

This section presents a final test of START's soil-gas radon concentration solution. The boundary conditions here are identical to those of the Ogata solution (validation scenario 3), but validation scenario 4 includes radioactive decay within the soil column. The applicable nondimensional, transient, radon mass balance equation is (refer to equation (5.28))

$$\frac{\partial}{\partial t}(\varepsilon C) = D\frac{\partial^2 C}{\partial x^2} - u\frac{\partial C}{\partial x} - \varepsilon C \tag{5.47}$$

Equations (5.43) - (5.45) define the boundary and initial conditions for this scenario.

We solve equation (5.47) by applying, sequentially, Laplace transforms in time and space. Applying the Laplace transform in time to equation (5.47) yields

$$\varepsilon q\overline{C} = D\frac{\partial^2 \overline{C}}{\partial x^2} - u\frac{\partial \overline{C}}{\partial x} - \varepsilon \overline{C} \tag{5.48}$$

where $\overline{C}$ is the Laplace transform of C, and q is the Laplace variable corresponding to a derivative in t. The Laplace transforms of the boundary conditions are

$$\overline{C}(0,t) = \frac{1}{q} \tag{5.49}$$

$$\overline{C}(\infty,t) = 0 \tag{5.50}$$

Taking the spatial Laplace transform of equation (5.48) yields

$$Dr^2 - ur - \varepsilon - \varepsilon q = 0 \tag{5.51}$$

where r is the Laplace variable corresponding to a derivative in x. The solution to equation (5.48) is

$$\overline{C} = Ae^{r_1 x} + Be^{r_2 x} \tag{5.52}$$

where A and B are constants, and r_1 and r_2 are roots of equation (5.51), in particular,

$$r_1,\ r_2 = \frac{u \pm \sqrt{u^2 + 4D\varepsilon(1+q)}}{2D} \tag{5.53}$$

We assign r_1 to the negative root and r_2 to the positive root. The second boundary condition (equation (5.50)) implies that $B = 0$. The first boundary condition (equation (5.49)) implies

$$A = \frac{1}{q} \tag{5.54}$$

Therefore, the temporal Laplace-transformed concentration equation is

$$\overline{C} = \frac{e^{r_1 x}}{q} = \frac{1}{q}\exp\left(\frac{ux}{2D}\right)\exp\left\{-\sqrt{\frac{u^2 + 4D\varepsilon(1+q)}{4D^2}}x\right\} \tag{5.55}$$

The following substitutions facilitate performing the inverse temporal Laplace transform of equation (5.55):

$$\kappa = 4D^2 \tag{5.56}$$

$$\alpha = u^2 + 4D\varepsilon \tag{5.57}$$

$$s = \alpha + 4D\varepsilon q \tag{5.58}$$

where s is a linear transform of the Laplace variable q, and κ and α are constants.

Substituting equations (5.56) - (5.58) into equation (5.55) yields

$$\overline{C} = \exp\left(\frac{ux}{2D}\right)\frac{4D\varepsilon}{s-\alpha}\exp\left\{-\sqrt{\frac{s}{\kappa}}x\right\} \tag{5.59}$$

Carslaw and Jaeger (1959, pg. 495) present the inverse Laplace transform as

$$\mathcal{L}^{-1}\left\{\frac{\exp\left(-\sqrt{\frac{s}{\kappa}}x\right)}{s-\alpha}\right\} = \frac{1}{2}\exp(\alpha t')\exp\left(-x\sqrt{\frac{\alpha}{\kappa}}\right)\operatorname{erfc}\left[\frac{x}{2\sqrt{\kappa t'}}-\sqrt{\alpha t'}\right]+ \tag{5.60}$$

$$\frac{1}{2}\exp(\alpha t')\exp\left(x\sqrt{\frac{\alpha}{\kappa}}\right)\operatorname{erfc}\left[\frac{x}{2\sqrt{\kappa t'}}+\sqrt{\alpha t'}\right]$$

where t' is the inverse Laplace variable corresponding to s and $\mathcal{L}^{-1}$ represents the inverse Laplace operator. Therefore

$$C(x,t') = 4D\varepsilon\exp\left(\frac{ux}{2D}\right)\frac{1}{2}\exp(\alpha t')* \tag{5.61}$$

$$\left\{\begin{array}{l}\exp\left(-x\sqrt{\frac{\alpha}{\kappa}}\right)\operatorname{erfc}\left[\frac{x}{2\sqrt{\kappa t'}}-\sqrt{\alpha t'}\right]+\\ \exp\left(x\sqrt{\frac{\alpha}{\kappa}}\right)\operatorname{erfc}\left[\frac{x}{2\sqrt{\kappa t'}}+\sqrt{\alpha t'}\right]\end{array}\right\}$$

To transform back to the original time variable (t), we use (Abramowitz and Stegun, 1964, page 1021; Boyce and DiPrima, 1977, page 401)

$$\mathcal{L}^{-1}\left\{F\left(\frac{s-\alpha}{4D\varepsilon}\right)\right\} = \mathcal{L}^{-1}\{F(q)\} = \frac{1}{4D\varepsilon}\exp(-\alpha t')f\left(\frac{t}{4D\varepsilon}\right) \tag{5.62}$$

In this application, f represents C in equation (5.61). Applying equation (5.62) to equation (5.61) gives the concentration in the column as a function of position and time:

$$C(x,t) = \frac{1}{2}\exp\left(\frac{ux}{2D}\right)* \left\{\begin{array}{l} \exp\left(-x\sqrt{\frac{\alpha}{\kappa}}\right)\operatorname{erfc}\left[\frac{x}{2\sqrt{\kappa\frac{t}{4D\varepsilon}}} - \sqrt{\alpha\frac{t}{4D\varepsilon}}\right] + \\ \exp\left(x\sqrt{\frac{\alpha}{\kappa}}\right)\operatorname{erfc}\left[\frac{x}{2\sqrt{\kappa\frac{t}{4D\varepsilon}}} + \sqrt{\alpha\frac{t}{4D\varepsilon}}\right] \end{array}\right\} \tag{5.63}$$

Figure 5.8 presents the comparison between the START predictions and the analytical solution, equation (5.63), at times of 100, 200, and 300 hours. The START predictions match the analytical solutions very well.

5.5.2 Experimental Validation of START (Validation Scenario 5)

In this section, we use START to predict soil-gas and radon entry rates into an experimental basement located at the Small Structures Facility in the Santa Cruz Mountains. The simulation predictions are compared to measurements from an

experiment designed to study the impacts of fluctuating atmospheric pressures on radon entry rates (see Robinson et al. (1995) for details of this experiment).

Fisk et al. (1992) describe the basement structure, instrumentation, and soil properties at the facility; we summarize the key features briefly here. The experimental structure has a basement depth of 2.25 m and a horizontal cross-section of 1.17 × 1.75 m (Figure 5.9). Soil-gas and radon enter through a 4 cm diameter hole in the center of the floor slab. This geometry insures that a sufficient amount of soil gas will move past a flow meter to obtain accurate measurements. Very little of the structure protrudes above ground in order to minimize the effects of wind on the structure's depressurization and ventilation rate.

We took advantage of the symmetry of the structure and modeled one quadrant of the soil and basement system. The uniform bulk soil permeability, gravel permeability, and air-filled porosity were taken to be 3×10^{-11} m^2, 2×10^{-8} m^2, and 0.4, respectively (Garbesi, 1994). We use a deep-soil radon concentration of 115,000 Bq m^{-3}, corresponding to the mean of about 50 measurements taken at the site. In the START simulation, 13,800 control volumes define the soil block and basement structure, and the time step is 60 s. The simulation begins with soil-gas pressure and radon concentration fields that correspond to the steady-state solution for zero disturbance pressure at the ground surface and basement crack.

Figure 5.10 shows the simulation predictions and the experimental results for both soil-gas and radon entry into the basement. The error in the average radon entry

rate over the two hour simulation is 3%. We hypothesize that the small time lags between the simulation and experimental entry rates are a result of the relatively large simulation time step.

For comparison, Garbesi (1994) modeled the radon entry rate into a similar basement structure. She demonstrated that a modified version of the steady-state model developed by Loureiro et al. (1990) underestimated the average radon entry rate by a factor of about 1.5. That level of error was a marked improvement over previous modeling attempts, which typically underpredicted radon entry by a factor of 7 to 10.

The START simulation shown in Figure 5.10 represents the first time a numerical model has predicted, on either a long-term average or transient basis, the soil-gas and radon entry rate into a real structure with such a high level of accuracy. The ability to accurately predict both the average and transient radon entry rates represents a strong validation of START's predictive ability.

5.6 Conclusions

This chapter has presented the development and validation of START, a transient, three-dimensional, soil-gas and radon transport model. The equations used to describe soil-gas and radon transport in soil surrounding a building have been presented. The discretization of the equations, and their implementation in the model, are described in an appendix to this chapter (Section 5.8).

We compared simulation predictions from START to four analytical solutions of soil-gas and radon flow through a one-dimensional column. These four tests

approximately span the range of environmental conditions under which START will be used to simulate soil-gas and radon transport in the presence of fluctuating winds. START predicted the soil-gas flows and radon concentrations in the soil column for the four validation cases very accurately. We also compared START predictions to experimental results from a thoroughly-characterized basement at the Small Structures Facility. START's prediction of the average radon entry rate over a two-hour period was within 3% of the measured value. This experimental validation demonstrates that START can accurately predict transient, three-dimensional soil-gas and radon transport and radon entry rates into real structures.

START simulations of transient soil-gas flow in the presence of fluctuating winds are very computationally intensive. Consequently, we use START to generate unit-step responses, which are required inputs to RapidSTART, the novel modeling technique described in Chapters 6 and 7.

5.7 References

Abramowitz E. M. and Stegun I. E. (1964) *Handbook of mathematical functions with formulas, graphs, and mathematical tables,* U.S. Govt. Print. Off., Washington D.C.

Bonnefous Y. C. (1994) Etude numerique des systemes de ventilation du sol pour diminuer la concentration en radon dans l'habitat, Ph.D. Thesis, report LBL-34244, Lawrence Berkeley National Laboratory, Berkeley, CA.

Bonnefous Y. C., Gadgil A. J., Fisk W. J., Prill R. J., and Nematollahi A. R. (1992) Field study and numerical simulation of subslab ventilation systems, *Environ. Sci. Technol.* **26**, 1752-1759.

Boyce W. E. and DiPrima R. C. (1977) *Elementary Differential Equations and Boundary Value Problems,* John Wiley and Sons, New York, NY.

Carslaw H. S. and Jaeger J. C. (1959) *Conduction of Heat in Solids,* Clarendon Press, Oxford.

DSMA Atcon Ltd. (1983) Review of existing information and evaluation for possibilities of research and development of instrumentation to determine future levels of radon at a proposed building site, report INFO-0096, Atomic Energy Control Board, Ottawa, Canada.

DSMA Atcon Ltd. (1985) A computer study of soil gas movement into buildings, report 1389/1333, Department of Health and Welfare, Ottawa, Canada.

Eaton R. S. and Scott A. G. (1984) Understanding radon transport into houses, *Radiat. Prot. Dosim.* **7**, 251-253.

Fisk W. J., Modera M. P., Sextro R. G., Garbesi K., Wollenberg H. A., Narasimhan T. N., Nuzum T., and Tsang Y. W. (1992) Radon entry into basements: Approach, experimental structures, and instrumentation of the small structures project, report LBL-31864, Lawrence Berkeley National Laboratory, Berkeley CA.

Fisk W. J., Prill R. J., Wooley J., Bonnefous Y. C., Gadgil A. J., and Riley W. J. (1995) New methods of energy efficient radon mitigation, *Health Phys.* **68**, 689-698.

Forchheimer P. H. (1901) *Z. Ver. Dtsch. Ing.* **45**, 1782-1788.

Gadgil A. (1992) Models of radon entry, *Radiation Protection Dosimetry* **45**, 373-380.

Garbesi K. (1994) Toward resolving model-measurement discrepancies of radon entry into houses, Ph.D. Thesis, report LBL-34244, Lawrence Berkeley National Laboratory, Berkeley, CA.

Holford D., Schery S. D., Wilson J. L., and Phillips F. M. (1993) Modeling radon transport in dry, cracked soil, *J. Geophys. Res.* **98**, 567-580.

Loureiro C. O. (1987) Simulation of the steady-state transport of radon from soil into houses with basements under constant negative pressure, Ph.D. Thesis, report LBL-24378, Lawrence Berkeley National Laboratory, Berkeley, CA.

Loureiro C. O., Abriola L. M., Martin J. E., and Sextro R. G. (1990) Three-dimensional simulation of radon transport into houses with basements under constant negative pressure, *Environ. Sci. Technol.* **24**, 1338-1348.

Mele D. A. and Joseph D. D. (1985) Effects of quadratic drag on convection in a saturated porous medium, *Phys. Fluids* **28**, 995-997.

Ogata A. (1970) Theory of dispersion in a granular medium, Professional Paper 411-I, United States Geological Survey, Washington, D.C.

Revzan K. L., Fisk W. J., and Gadgil A. J. (1991) Modeling radon entry into houses with basements: Model description and verification, *Indoor Air* **1**, 173-189.

Robinson A. L. and Sextro R. G. (1995) Direct measurements of soil-gas entry into an experimental basement driven by atmospheric pressure fluctuations, *Geophysical Research Letters* **22**, 1929-1932.

Robinson A. L., Sextro R. G., and Fisk W. J. (1995) Soil-gas entry into houses driven by atmospheric pressure fluctuations, part 1 --- Measurements, spectral analysis, and model comparison, report LBL-38232, Lawrence Berkeley National Laboratory, Berkeley CA.

Table 5.1. Nondimensionalizing parameters for the soil-gas pressure, velocity, and concentration equations. This method of nondimensionalizing the equations was inherited from Loureiro (1987); ideally, a minimum set of nondimensionalizing parameters should be used.

Parameter	Description	Value
p_c	Characteristic gage pressure	1 Pa
t_c	Characteristic time $\left(=\frac{1}{\lambda_{Rn}}\right)$	4.7664×10^{5} s
L_c	Characteristic length $\left(=\sqrt{\frac{D_c}{\lambda_{Rn}}}\right)$	0.690 m
u_c	Characteristic velocity $\left(=\sqrt{D_c\lambda_{Rn}}\right)$	1.45×10^{-6} m s^{-1}
D_c	Diffusion coefficient for radon in the soil gas	1×10^{-6} m^2 s^{-1}
μ_c	Characteristic air viscosity	1.8×10^{-5} kg m^{-1} s^{-1}
k_c	Characteristic soil permeability	10^{-10} m^2
c_c	Characteristic Forchheimer term $\left(=\frac{1}{u_c}\right)$	6.90×10^{5} s m^{-1}
S_c	Characteristic production rate of radon	4.11×10^{-2} Bq m^{-3} s^{-1}
C_c	Characteristic deep-soil radon concentration	1.96×10^{4} Bq m^{-3}

Table 5.2. The analytical and experimental validation tests of START.

Validation Scenario	Description	Section	Figure(s)
1	Pressure field validation	5.5.1.1	5.1 - 5.5
2	Steady-state concentration profile convergence validation	5.5.1.2	5.6
3	Comparison to the Ogata solution	5.5.1.3	5.7
4	Ogata solution with radioactive decay	5.5.1.4	5.8
5	Comparison to experimental results from the Small Structures Facility	5.5.2	5.10

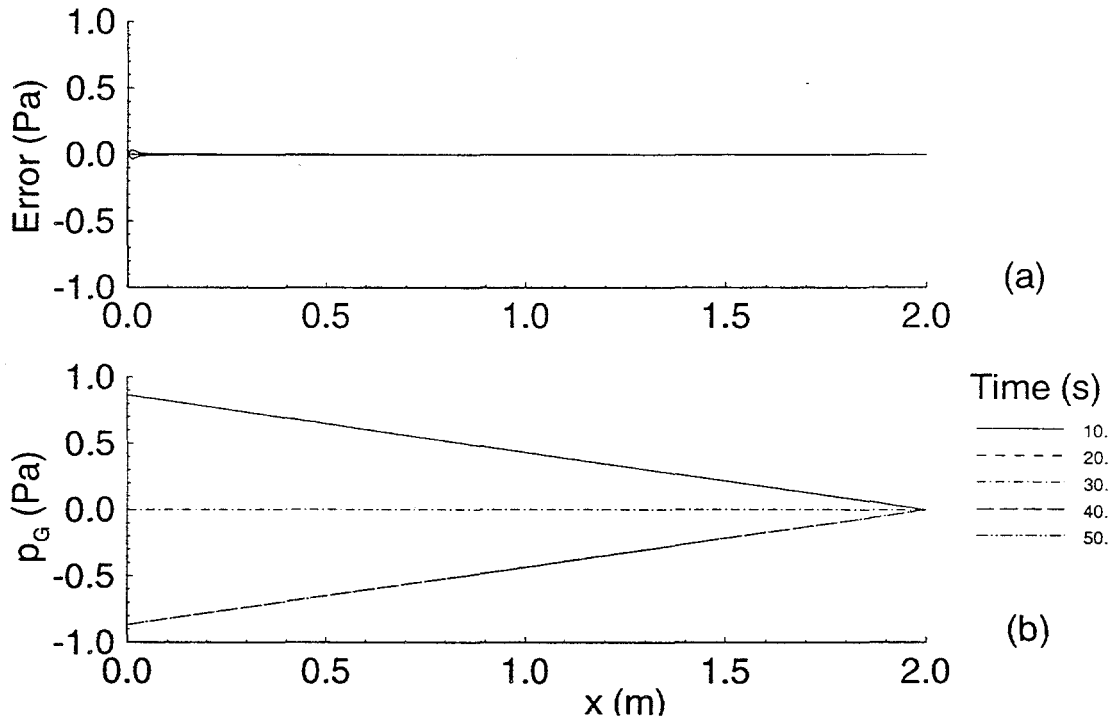

Figure 5.1. Comparison of START to the analytical solution for a fluctuating pressure boundary condition (validation scenario 1). The soil permeability is 10^{-9} m^2. The error shown (a) is the difference between the analytical solution and START's prediction. The soil-gas pressure in the column is shown in (b). Two pairs of the five lines in (b) are coincident.

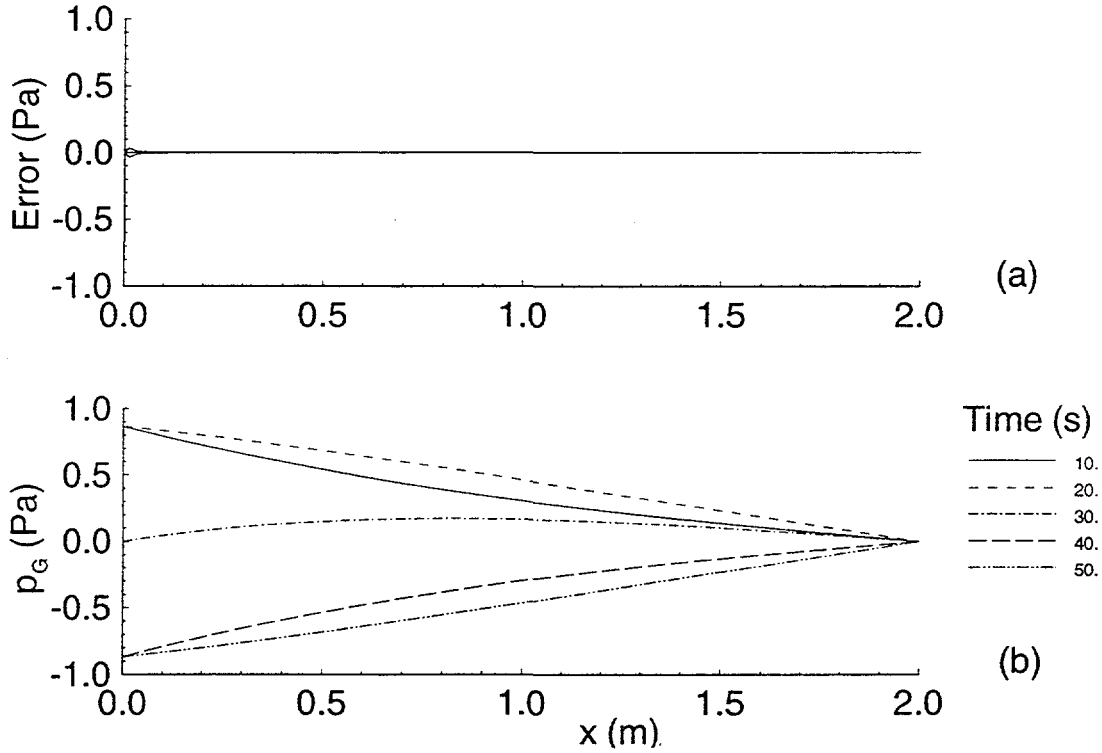

Figure 5.2. Comparison of START to the analytical solution for a fluctuating pressure boundary condition (validation scenario 1). The soil permeability is 10^{-11} m^2. The error shown (a) is the difference between the analytical solution and START's prediction. The soil-gas pressure in the column is shown in (b).

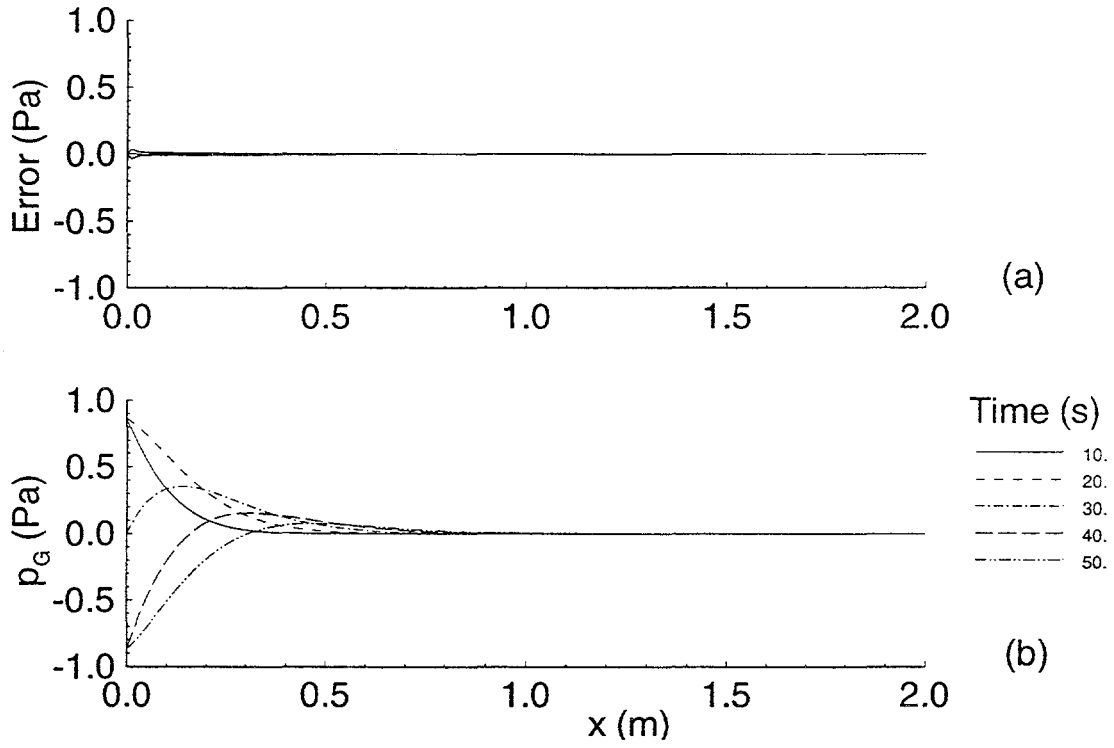

Figure 5.3. Comparison of START to the analytical solution for a fluctuating pressure boundary condition (validation scenario 1). The soil permeability is 10^{-13} m^2. The error shown (a) is the difference between the analytical solution and START's prediction. The soil-gas pressure in the column is shown in (b).

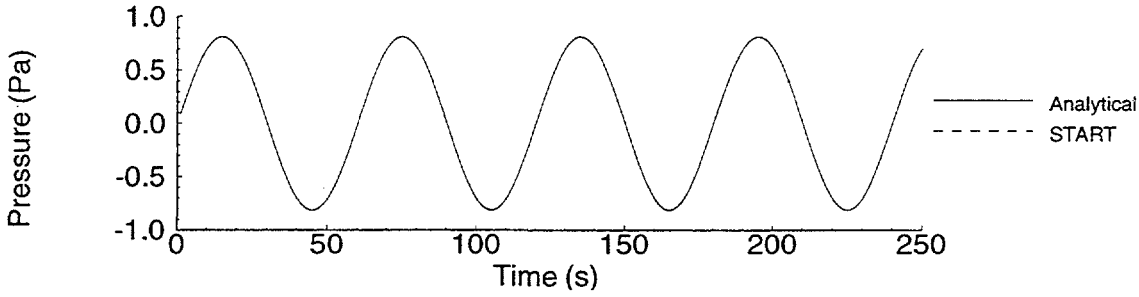

Figure 5.4. Comparison of the soil-gas pressure at 37.5 cm in the soil column (validation scenario 1). The analytical and START solutions are shown. The soil permeability is 10^{-8} m^2.

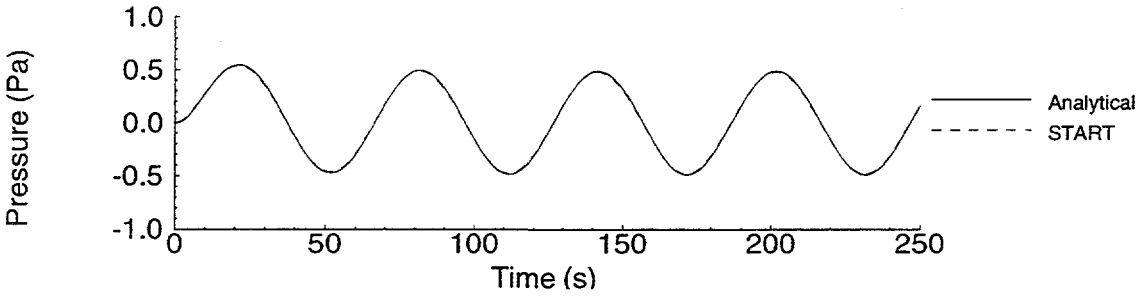

Figure 5.5. Comparison of the soil-gas pressure at 37.5 cm in the soil column (validation scenario 1). The analytical and START solutions are shown. The soil permeability is 10^{-12} m^2.

/transient/duhamel/fig6-4-5.lay
/transient/duhamel/analytical-fd-k8.out
/transient/duhamel/analytical-fd-k12.out

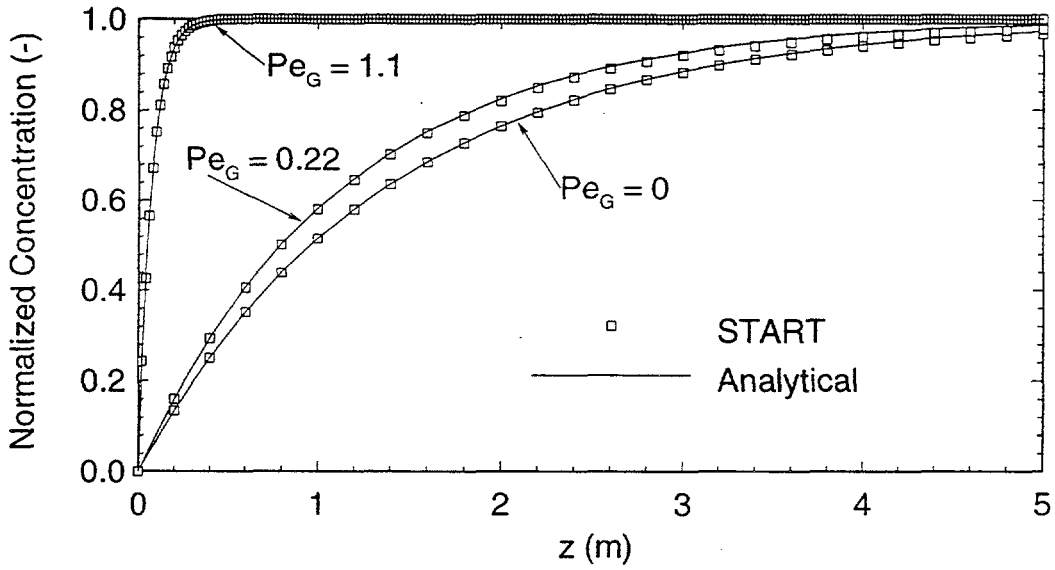

Figure 5.6. Comparison of START to analytical solutions for steady-state radon transport in a long column (validation scenario 2). The soil permeability is 1×10^{-11} m^2, and several grid Peclet numbers are shown.

/transient/fig6-6.lay
/transient/analytical-ss.out

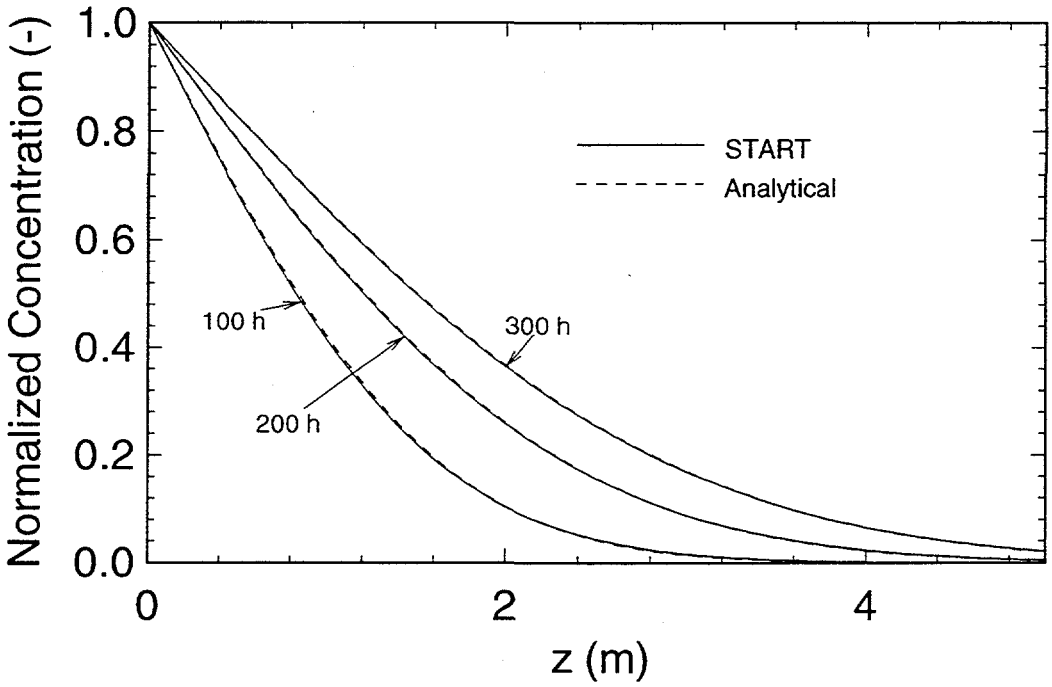

Figure 5.7. Comparison of START to the Ogata analytical solution (validation scenario 3). The soil permeability is $k=10^{-11}$ m^2, and a pressure drop of 5 Pa has been applied across the 30 m column.

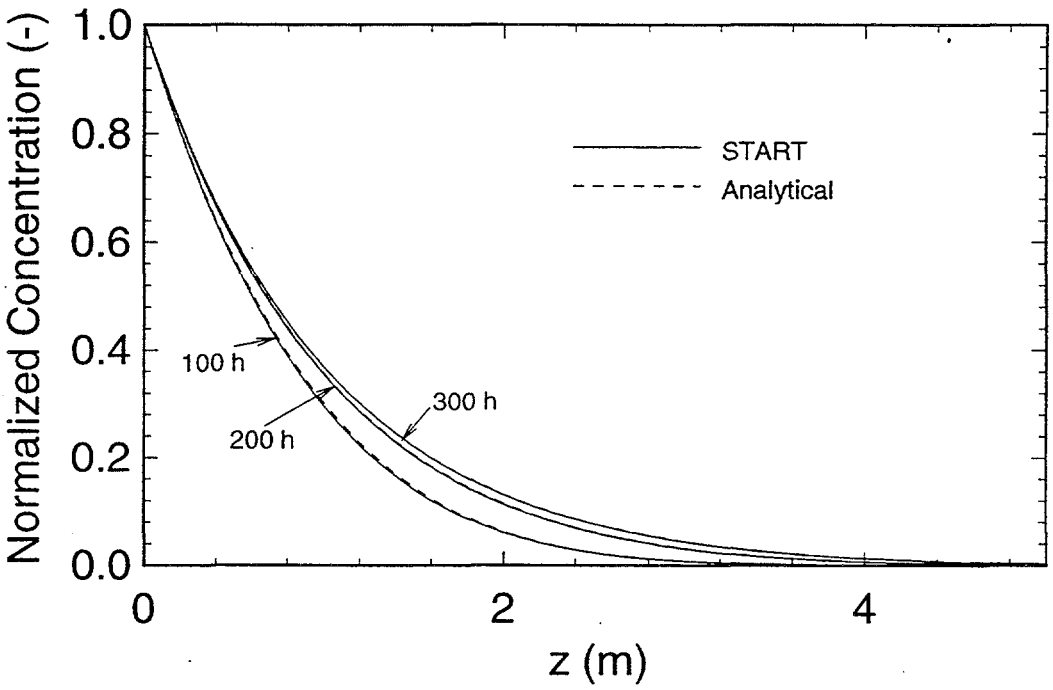

Figure 5.8. Comparison of START to the analytical solution for radon flow through the column, no radon source in the soil, and a constant source of radon at the inlet. Radioactive decay is included. The soil permeability is 10^{-11} m^2, and a pressure drop of 5 Pa has been applied across the 30 m column.

/transient/no-source.lay
/transient/analytical-no-source.out

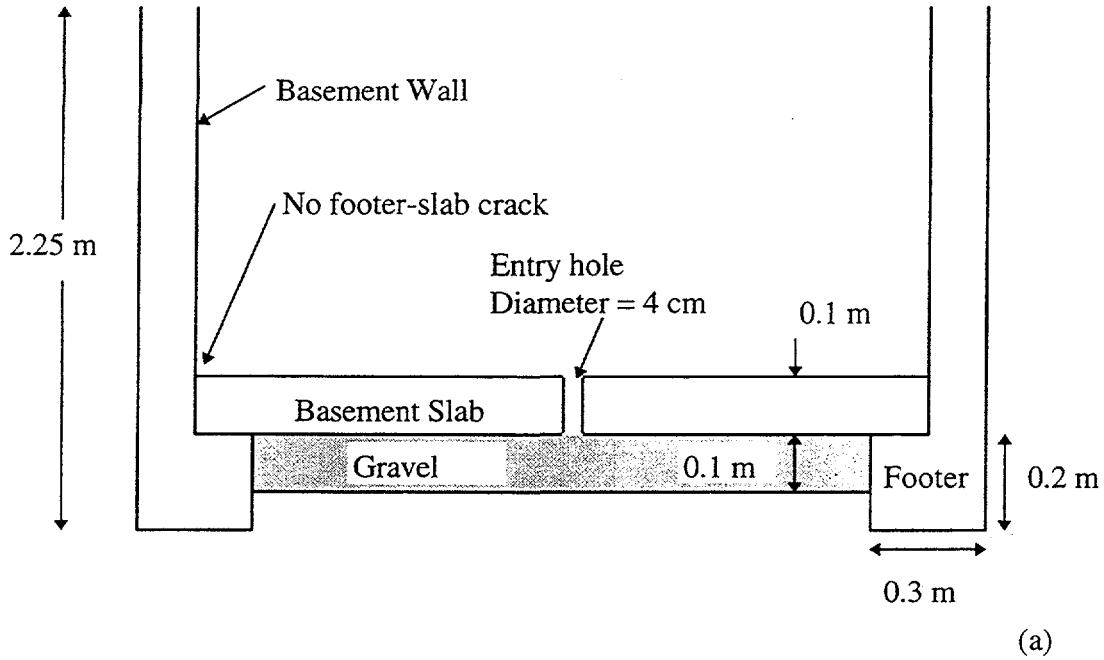

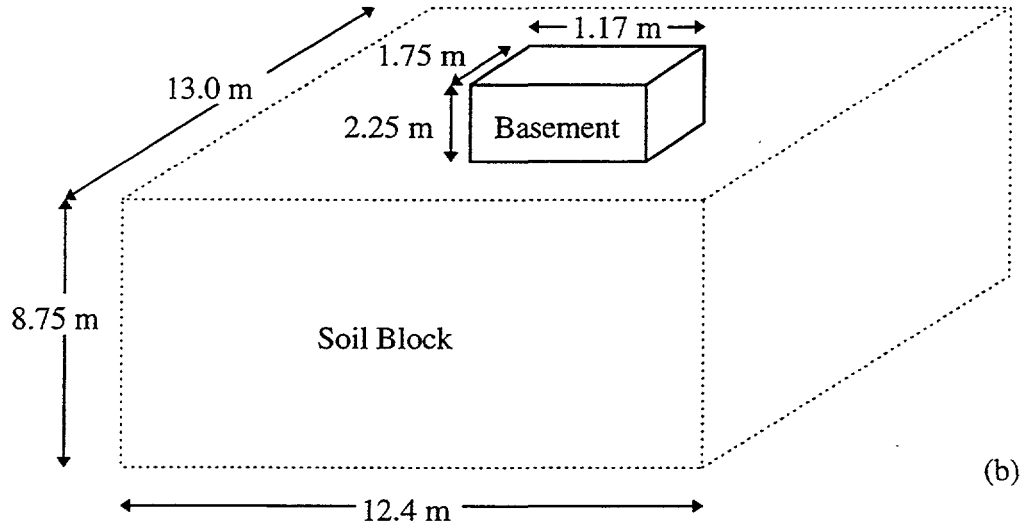

Figure 5.9. The geometry of the Small Structures basement used in the simulations.

c:/thesis/fig5_10.doc

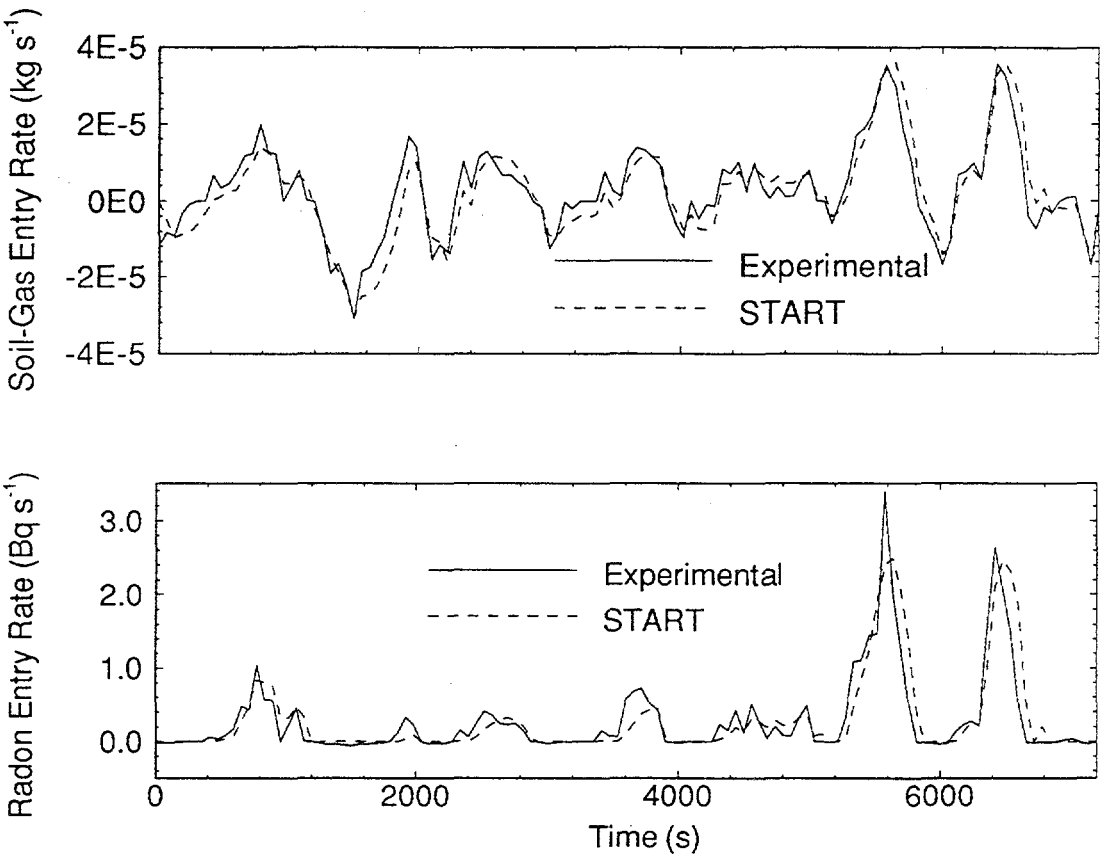

Figure 5.10. Comparison of START to results from the Small Structures experiment (validation scenario 5).

/allen/riley/mass-radon.lay

5.8 Appendix I: Numerical Solution of the Soil-Gas Pressure, Velocity, and Radon Concentration Equations

5.8.1 Introduction

This appendix describes the discretization and implementation into START of the subsurface soil-gas and radon transport equations. Sections 5.8.3 - 5.8.5 present the discretized equations used to compute the soil-gas pressure and velocity fields. We base the discretization on the time-dependent continuity and Darcy-Forchheimer equations (equations (5.15) and (5.18), respectively). Section 5.8.6 describes the discretization of the equations used to determine the soil-gas radon concentration field. Sections 5.8.5 and 5.8.6 also discuss the implementation of the discretized equations into START.

5.8.2 Additional Nomenclature

a_P, a_E, a_W, a_N, a_S, a_B, a_T	constants used to solve for the pressure field (-)
B	constant used to solve for the concentration field (-)
b_P, b_E, b_W, b_N, b_S, b_B, b_T	constants used to solve for the concentration field (-)
c_P, c_E	Forchheimer term (-) evaluated at P and E, respectively

C_P, C_E, C_W, C_N, C_S, C_B, C_T	radon concentration (-) at the indicated node for the current time
d	constant used to solve for the pressure field (-)
D_e, D_w, D_n, D_s, D_b, D_t	radon diffusion coefficients (-) at the indicated control-volume interfaces
F_e, F_w, F_n, F_s, F_b, F_t	soil-gas flow rates (-) through the indicated control-volume interfaces
f_P	constant used to solve for the soil-gas velocity (-)
G_e, G_w, G_n, G_s, G_b, G_t	conductances (-) evaluated at the indicated control-volume interfaces
J_x, J_y, J_z	radon fluxes (-) in the x, y, and z directions, respectively
J_e, J_w, J_n, J_s, J_b, J_t	integrated radon fluxes (-) through the indicated interfaces
k_e, k_w, k_n, k_s, k_b, k_t	calculated soil permeabilities (-) at the indicated interfaces
k_P, k_E	soil permeabilities (-) at node points P and E, respectively
p_e	disturbance pressure (-) at the control-volume interface e
p_P, p_E, p_W, p_N, p_S, p_B, p_T	current-time-step disturbance pressures (-) at the indicated nodes
P_e, P_w, P_n, P_s, P_b, P_t	Peclet numbers (-) evaluated at the indicated control-volume interfaces
S_P	radon source strength at P (-)

s_P, s_E	magnitudes of the Darcy velocities (-) at the nodes P and E, respectively
Δt	time step (-)
u_e, u_w	x-component Darcy velocities (-) at the indicated interfaces
v_n, v_s	y-component Darcy velocities (-) at the indicated interfaces
w_b, w_t	z-component Darcy velocities (-) at the indicated interfaces
X	constant used in the pressure calculations (-)
Δx_P, Δx_E, Δx_W, Δy_P, Δy_N, Δy_S, Δz_P, Δz_B, Δz_T	x-, y-, and z-dimensions (-) of the indicated control volumes
$(\delta x)_e$, $(\delta x)_w$, $(\delta y)_n$, $(\delta y)_s$, $(\delta z)_b$, $(\delta z)_t$	distances between nodes (-) adjacent to the indicated interfaces

Notes: 1. (-) indicates a nondimensional variable.

2. This nomenclature table does not list all the variables used in this appendix; some of the variables are defined in the nomenclature table for Chapter 5, and the following symbols are used to modify the variables defined above:

   a. An overbar $(\bar{x})$ indicates the current-iteration value of the variable.

   b. A double prime (x'') indicates a correction for the next iteration of the variable.

c. An overdot $(\dot{x})$ indicates the previous-time-step value of the variable.

5.8.3 Discretization of the Continuity Equation

We employ a spatial discretization of the continuity equation (equation (5.15)) similar to that described in Bonnefous (1994). The temporal discretization is fully implicit; in particular, START evaluates all of the soil-gas velocities (and the corresponding disturbance pressures) in equation (5.15) at the current time step. Figure 5A.1 illustrates the spatial distribution of nodes and control-volume interfaces about a generic control volume centered at the point P. For example, in the x-direction, the node toward increasing x is labeled E, the node toward decreasing x is labeled W, the interface between nodes P and E is labeled e, and the interface between nodes P and W is labeled w.

Discretizing equation (5.15) using the velocities at the interfaces between control volumes gives

$$\frac{\varepsilon(p_p - \dot{p}_p)}{\Delta t} + p_A\left\{\frac{u_e - u_w}{\Delta x_P} + \frac{v_n - v_s}{\Delta y_P} + \frac{w_b - w_t}{\Delta z_P}\right\} = 0 \qquad (5A.1)$$

where p_P is the current-time-step disturbance pressure at P (-); $\dot{p}_P$ is the disturbance pressure from the previous time step at P (-); Δt is the time step (-); Δx_P, Δy_P, and Δz_P are the x-, y-, and z-dimensions (-) of the control volume centered at P, respectively; u_e is the x-component of the Darcy velocity (-) at the interface between the nodes P and E; u_w is the x-component of the Darcy velocity (-) at the interface between the nodes P and W; and the other Darcy velocities are defined analogously.

Patankar (1980) has shown that simultaneously applying nodal velocities and pressures to discretize the continuity equation can lead to unrealistic solutions. We therefore use the interfacial velocities (denoted by the subscripts e, w, n, s, b, and t) in combination with the nodal pressures (denoted by the subscripts P, E, W, N, S, B, and T) to avoid this problem.

5.8.4 Discretization of the Darcy-Forchheimer Equation

We discretize the Darcy-Forchheimer equation (equation (5.18)) below in one dimension, and then apply the general form to all three dimensions. This procedure generates expressions for the velocity differences appearing in equation (5A.1) in terms of the disturbance pressures at the node points surrounding P.

For the disturbance pressure variation in the x-direction about the node point P, equation (5.18) becomes

$$(1 + c|\vec{u}|)u = -\frac{k}{N_c \mu}\frac{\partial p_G}{\partial x} \tag{5A.2}$$

Discretizing equation (5A.2) between the node point P and the control-volume interface e gives

$$(1 + c_P s_P)u_e = -\frac{k_P}{N_c \mu}\left[\frac{p_e - p_P}{\frac{1}{2}\Delta x_P}\right] \tag{5A.3}$$

Discretizing equation (5A.2) between the node point E and the control-volume interface e gives

$$(1+c_E s_E)u_e = -\frac{k_E}{N_c \mu}\left[\frac{p_E - p_e}{\frac{1}{2}\Delta x_E}\right] \tag{5A.4}$$

where, in equations (5A.3) and (5A.4), the variables c, s, u, k, and p are evaluated at the locations given by their subscripts. For example, p_e is the disturbance pressure (-) at the control-volume interface e, and p_P and p_E are the disturbance pressures (-) at the node points P and E, respectively. The speeds s_P and s_E (-) are estimates of the magnitudes of the Darcy velocities at the nodes P and E, respectively. For example,

$$s_P = \frac{1}{2}\left[(u_e + u_w)^2 + (v_n + v_s)^2 + (w_b + w_t)^2\right]^{1/2} \tag{5A.5}$$

Eliminating p_e between equations (5A.3) and (5A.4) yields

$$\left[1 + \frac{\Delta x_P k_E c_P s_P + \Delta x_E k_P c_E s_E}{\Delta x_P k_E + \Delta x_E k_P}\right] u_e = -2\frac{k_e}{N_c \mu}\left[\frac{p_E - p_P}{\Delta x_P + \Delta x_E}\right] \tag{5A.6}$$

where

$$k_e = \frac{k_P k_E (\Delta x_P + \Delta x_E)}{k_P \Delta x_E + k_E \Delta x_P} \tag{5A.7}$$

Equation (5A.6) can be simplified by substituting

$$f_P = \left[1 + \frac{\Delta x_P k_E c_P s_P + \Delta x_E k_P c_E s_E}{\Delta x_P k_E + \Delta x_E k_P}\right] \tag{5A.8}$$

Applying equation (5A.8) to equation (5A.6), and solving for u_e gives

$$u_e = -2\frac{k_e}{N_c \mu}\left[\frac{p_E - p_P}{\Delta x_P + \Delta x_E}\right]\frac{1}{f_P} \tag{5A.9}$$

Written in this form, f_P is a factor that corrects the numerical approximation to Darcy's law for inertial resistance. In the limit of low flow, $f_P \to 1$.

5.8.5 Determination of the Soil-Gas Pressure Field

The soil-gas pressure iteration scheme is developed by computing a correction to the current value of the soil-gas velocity at each node point. In the following equations, an overbar indicates a current-iteration value of the previously defined variables. The current-iteration value of the x-component of velocity at the interface e is

$$\overline{u}_e = -2\frac{k_e}{N_c \mu}\left[\frac{\overline{p}_E - \overline{p}_P}{\Delta x_P + \Delta x_E}\right]\frac{1}{\overline{f}_P} \tag{5A.10}$$

where, for example, $\overline{p}_P$ is the current-iteration disturbance pressure (-) at point P.

The correction (denoted by $''$), u_e'', to $\overline{u}_e$ for the next iteration is taken as a Darcy law correction (i.e., taking $f_P = 1$)

$$u_e'' = 2\frac{k_e}{N_c\mu}\left[\frac{\overline{p}_E - \overline{p}_P}{\Delta x_P + \Delta x_E}\right] - 2\frac{k_e}{N_c\mu}\left[\frac{p_E - p_P}{\Delta x_P + \Delta x_E}\right] \tag{5A.11}$$

START computes the next-iteration value of the Darcy velocity at e, u_e, as the sum of the current value, $\overline{u}_e$, and the correction u_e'', or

$$u_e = \overline{u}_e + u_e'' \tag{5A.12}$$

The equations analogous to equation (5A.12) for the remaining velocity components are

$$u_w = \overline{u}_w + u_w'' \tag{5A.13}$$

$$v_n = \overline{v}_n + v_n'' \tag{5A.14}$$

$$v_s = \overline{v}_s + v_s'' \tag{5A.15}$$

$$w_t = \overline{w}_t + w_t'' \tag{5A.16}$$

$$w_b = \overline{w}_b + w_b'' \tag{5A.17}$$

Substituting equation (5A.11) into equation (5A.12) yields

$$u_e = -2\frac{k_e}{N_c\mu}\left[\frac{p_E - p_P}{\Delta x_P + \Delta x_E}\right] + \overline{u}_e + 2\frac{k_e}{N_c\mu}\left[\frac{\overline{p}_E - \overline{p}_P}{\Delta x_P + \Delta x_E}\right] \tag{5A.18}$$

The equations analogous to equation (5A.18) for the remaining velocity components are

$$u_w = -2\frac{k_w}{N_c\mu}\left[\frac{p_P - p_W}{\Delta x_P + \Delta x_W}\right] + \overline{u}_w + 2\frac{k_w}{N_c\mu}\left[\frac{\overline{p}_P - \overline{p}_W}{\Delta x_P + \Delta x_W}\right] \tag{5A.19}$$

$$v_n = -2\frac{k_n}{N_c\mu}\left[\frac{p_N - p_P}{\Delta y_P + \Delta y_N}\right] + \overline{v}_n + 2\frac{k_n}{N_c\mu}\left[\frac{\overline{p}_N - \overline{p}_P}{\Delta y_P + \Delta y_N}\right] \tag{5A.20}$$

$$v_s = -2\frac{k_s}{N_c\mu}\left[\frac{p_P - p_S}{\Delta y_P + \Delta y_S}\right] + \overline{v}_s + 2\frac{k_s}{N_c\mu}\left[\frac{\overline{p}_P - \overline{p}_S}{\Delta y_P + \Delta y_S}\right] \tag{5A.21}$$

$$w_b = -2\frac{k_b}{N_c\mu}\left[\frac{p_B - p_P}{\Delta z_P + \Delta z_B}\right] + \overline{w}_b + 2\frac{k_b}{N_c\mu}\left[\frac{\overline{p}_B - \overline{p}_P}{\Delta z_P + \Delta z_B}\right] \tag{5A.22}$$

$$w_t = -2\frac{k_t}{N_c\mu}\left[\frac{p_P - p_T}{\Delta z_P + \Delta z_T}\right] + \overline{w}_t + 2\frac{k_t}{N_c\mu}\left[\frac{\overline{p}_P - \overline{p}_T}{\Delta z_P + \Delta z_T}\right] \tag{5A.23}$$

where the subscripts on k define the control-volume interface where the permeability is evaluated, and Δx_E, Δx_W, Δy_N, Δy_S, Δz_B, and Δz_T are the x-, y-, and z-dimensions of the indicated control volumes.

Substituting equations (5A.18) - (5A.23) into equation (5A.1) yields

$$\frac{\varepsilon}{p_A \Delta t} p_p - \frac{\varepsilon}{p_A \Delta t} \dot{p}_p + \left\{ \frac{\overline{u}_e - \overline{u}_w}{\Delta x_P} + \frac{\overline{v}_n - \overline{v}_s}{\Delta y_P} + \frac{\overline{w}_b - \overline{w}_t}{\Delta z_P} \right\} \tag{5A.24}$$
$$-a_E p''_E - a_W p''_W - a_N p''_N - a_S p''_S - a_B p''_B - a_T p''_T$$
$$+(a_E + a_W + a_N + a_S + a_B + a_T) p''_p = 0$$

where, for example, p''_P represents the correction pressure (-) at point P, defined by equation (5A.31) below, and

$$a_E = 2 \frac{k_e}{N_c \mu \Delta x_P} \left(\frac{1}{\Delta x_E + \Delta x_P} \right) \tag{5A.25}$$

$$a_W = 2 \frac{k_w}{N_c \mu \Delta x_P} \left(\frac{1}{\Delta x_W + \Delta x_P} \right) \tag{5A.26}$$

$$a_N = 2 \frac{k_n}{N_c \mu \Delta y_P} \left(\frac{1}{\Delta y_N + \Delta y_P} \right) \tag{5A.27}$$

$$a_S = 2 \frac{k_s}{N_c \mu \Delta y_P} \left(\frac{1}{\Delta y_S + \Delta y_P} \right) \tag{5A.28}$$

$$a_B = 2 \frac{k_b}{N_c \mu \Delta z_P} \left(\frac{1}{\Delta z_B + \Delta z_P} \right) \tag{5A.29}$$

$$a_T = 2 \frac{k_t}{N_c \mu \Delta z_P} \left(\frac{1}{\Delta z_T + \Delta z_P} \right) \tag{5A.30}$$

The next-iteration pressure at point P can be written as

$$p_P = \bar{p}_p + p''_p \tag{5A.31}$$

To simplify the resulting equations, we define

$$a_P = a_E + a_W + a_N + a_S + a_B + a_T + \frac{\varepsilon}{p_A \Delta t} \tag{5A.32}$$

and

$$d = -\frac{\varepsilon}{p_A \Delta t}\bar{p}_p + \frac{\varepsilon}{p_A \Delta t}\dot{p}_p - \left\{\frac{\bar{u}_e - \bar{u}_w}{\Delta x_P} + \frac{\bar{v}_n - \bar{v}_s}{\Delta y_P} + \frac{\bar{w}_b - \bar{w}_t}{\Delta z_P}\right\} \tag{5A.33}$$

Substituting equations (5A.32) and (5A.33) into equation (5A.24) gives

$$a_P p''_P = a_E p''_E + a_W p''_W + a_N p''_N + a_S p''_S + a_B p''_B + a_T p''_T + d \tag{5A.34}$$

START first solves equation (5A.34) for individual lines in the soil block parallel to the x-direction, using previous iteration values of the pressures in neighboring lines. This procedure is repeated for lines in the y-direction, and finally for lines in the z-direction. START employs the tridiagonal matrix solver of Patankar (1980) to evaluate the pressure corrections. The process is applied in an iterative fashion to obtain a converged spatial solution at each time step. We consider the solution converged when successive iteration values of the pressure at all nodes change fractionally by less than 1×10^{-6}.

5.8.6 Determination of the Soil-Gas Concentration Field

The discretization of the transient radon concentration equation presented here follows the treatment by Loureiro (1987) of the steady-state radon concentration equation; I will use notation similar to his. Loureiro's discretization, in turn, closely follows Patankar's (1980) treatment of the Navier-Stokes equations.

Figure 5A.2 illustrates the scheme used to discretize equation (5.22); for simplicity, we have omitted the third dimension in the figure. The nondimensional radon fluxes into and out of the control volumes are

$$J_x = uC - D\frac{\partial C}{\partial x} \tag{5A.35}$$

$$J_y = vC - D\frac{\partial C}{\partial y} \tag{5A.36}$$

$$J_z = wC - D\frac{\partial C}{\partial z} \tag{5A.37}$$

where J_x, J_y, and J_z, are the radon fluxes (-) in the x, y, and z directions, respectively.

We discretize equation (5.22) as

$$\frac{\varepsilon\left(C_P - \dot{C}_P\right)\Delta x_P \Delta y_P \Delta z_P}{\Delta t} + \left(J_{x,e} - J_{x,w}\right)\Delta y_P \Delta z_P + \left(J_{y,n} - J_{y,s}\right)\Delta x_P \Delta z_P + \left(J_{z,b} - J_{z,t}\right)\Delta x_P \Delta y_P = \varepsilon\left(S_P - C_P\right)\Delta x_P \Delta y_P \Delta z_P \tag{5A.38}$$

where the second subscript on the radon fluxes references the control-volume interface that the flux crosses, C_P is the radon concentration (-) evaluated at P for the current time step, $\dot{C}_P$ is the radon concentration (-) evaluated at P from the previous time step, and S_P is the radon source strength (-) at P.

Defining the integrated fluxes (J) across each control-volume interface as

$$J_e = J_{x,e}\Delta y_P \Delta z_P \tag{5A.39}$$

$$J_w = J_{x,w}\Delta y_P \Delta z_P \tag{5A.40}$$

$$J_n = J_{y,n}\Delta x_P \Delta z_P \tag{5A.41}$$

$$J_s = J_{y,s}\Delta x_P \Delta z_P \tag{5A.42}$$

$$J_b = J_{z,b}\Delta x_P \Delta y_P \tag{5A.43}$$

$$J_t = J_{z,t}\Delta x_P \Delta y_P \tag{5A.44}$$

yields, on substitution to equation (5A.38),

$$\frac{\varepsilon\left(C_P - \dot{C}_P\right)\Delta x_P \Delta y_P \Delta z_P}{\Delta t} + \left(J_e - J_w\right) + \left(J_n - J_s\right) + \left(J_b - J_t\right) = \varepsilon\left(S_P - C_P\right)\Delta x_P \Delta y_P \Delta z_P \tag{5A.45}$$

We discretize the continuity equation (equation (5.15)) as

$$\frac{\varepsilon(p_p - \dot{p}_p)}{\Delta t}\Delta x_P \Delta y_P \Delta z_P + p_A\left\{\left(F_e - F_w\right) + \left(F_n - F_s\right) + \left(F_b - F_t\right)\right\} = 0 \tag{5A.46}$$

where the soil-gas flow (F) across each control-volume interface is

$$F_e = u_e \Delta y_P \Delta z_P \tag{5A.47}$$

$$F_w = u_w \Delta y_P \Delta z_P \tag{5A.48}$$

$$F_n = v_n \Delta x_P \Delta z_P \tag{5A.49}$$

$$F_s = v_s \Delta x_P \Delta z_P \tag{5A.50}$$

$$F_b = w_b \Delta x_P \Delta y_P \tag{5A.51}$$

$$F_t = w_t \Delta x_P \Delta y_P \tag{5A.52}$$

Dividing equation (5A.46) by p_A, and substituting

$$X = \frac{\varepsilon(p_P - \dot{p}_P)}{p_A \Delta t} \Delta x_P \Delta y_P \Delta z_P \tag{5A.53}$$

yields

$$X + (F_e - F_w) + (F_n - F_s) + (F_b - F_t) = 0 \tag{5A.54}$$

Multiplying equation (5A.54) by C_P and subtracting the result from equation (5A.45) gives

$$\frac{\varepsilon(C_P - \dot{C}_P)\Delta x_P \Delta y_P \Delta z_P}{\Delta t} - XC_P + (J_e - F_e C_P) - (J_w - F_w C_P) + (J_n - F_n C_P) - (J_s - F_s C_P) + (J_b - F_b C_P) - (J_t - F_t C_P) = \varepsilon(S_P - C_P)\Delta x_P \Delta y_P \Delta z_P \tag{5A.55}$$

The relationships between the concentrations at the node points and the six flux terms in equation (5A.55) are presented on page 101 of Patankar (1980). In the interest of brevity, we simply state them here:

$$J_e - F_e C_P = b_E (C_P - C_E) \tag{5A.56}$$

$$J_w - F_w C_P = b_W (C_W - C_P) \tag{5A.57}$$

$$J_n - F_n C_P = b_N (C_P - C_N) \tag{5A.58}$$

$$J_s - F_s C_P = b_S (C_S - C_P) \tag{5A.59}$$

$$J_b - F_b C_P = b_B (C_P - C_B) \tag{5A.60}$$

$$J_t - F_t C_P = b_T (C_T - C_P) \tag{5A.61}$$

where

$$b_E = G_e B(|P_e|) + [[-F_e, 0]] \tag{5A.62}$$

$$b_W = G_w B(|P_w|) + [[-F_w, 0]] \tag{5A.63}$$

$$b_N = G_n B(|P_n|) + [[-F_n, 0]] \tag{5A.64}$$

$$b_S = G_s B(|P_s|) + [[-F_s, 0]] \tag{5A.65}$$

$$b_B = G_b B(|P_b|) + [[-F_b, 0]] \tag{5A.66}$$

$$b_T = G_t B(|P_t|) + [[-F_t, 0]] \tag{5A.67}$$

$$B(|P|) = [[0, (1 - 0.1|P|)^5]] \tag{5A.68}$$

and $[[e, f]]$ denotes the larger of e or f. We define the conductances, G, and the Peclet numbers, P, at the control-volume interfaces as

$$G_e = \frac{D_e}{(\delta x)_e} \Delta y_P \Delta z_P; \; P_e = \frac{F_e}{G_e} \tag{5A.69}$$

$$G_w = \frac{D_w}{(\delta x)_w} \Delta y_P \Delta z_P; \; P_w = \frac{F_w}{G_w} \tag{5A.70}$$

$$G_n = \frac{D_n}{(\delta y)_n} \Delta x_P \Delta z_P; \; P_n = \frac{F_n}{G_n} \tag{5A.71}$$

$$G_s = \frac{D_s}{(\delta y)_s} \Delta x_P \Delta z_P; \; P_s = \frac{F_s}{G_s} \tag{5A.72}$$

$$G_b = \frac{D_b}{(\delta z)_b} \Delta x_P \Delta y_P; \; P_b = \frac{F_b}{G_b} \tag{5A.73}$$

$$G_t = \frac{D_t}{(\delta z)_t} \Delta x_P \Delta y_P ; \; P_t = \frac{F_t}{G_t} \tag{5A.74}$$

where $(\delta x)_e$, $(\delta x)_w$, $(\delta y)_n$, $(\delta y)_s$, $(\delta z)_b$, and $(\delta z)_t$ (-) are the distances between node points adjacent to the indicated control-volume interfaces (see Figure 5A.2), and D_e, D_w, D_n, D_s, D_b, and D_t (-) are the bulk radon diffusion coefficients evaluated at the indicated control-volume interfaces.

Substituting equations (5A.56) - (5A.61) into equation (5A.55) gives

$$\left(\frac{\varepsilon \Delta x_P \Delta y_P \Delta z_P}{\Delta t} - X + b_E + b_W + b_N + b_S + b_B + b_T + \varepsilon \Delta x_P \Delta y_P \Delta z_P \right) C_P = \tag{5A.75}$$
$$b_E C_E + b_W C_W + b_N C_N + b_S C_S + b_B C_B + b_T C_T +$$
$$\frac{\varepsilon \Delta x_P \Delta y_P \Delta z_P}{\Delta t} \dot{C}_P + \varepsilon \Delta x_P \Delta y_P \Delta z_P S_P$$

START solves equation (5A.75) iteratively, on a line-by-line basis, similar to the technique used to compute the pressure field. Again, the simultaneous equations from each line form a tridiagonal matrix, and we apply the technique of Patankar (1980) to reduce the equations. The concentration field is considered converged when the largest residual for the field falls below 1×10^{-6}.

5.8.7 References

Bonnefous Y. C. (1994) Etude numerique des systemes de ventilation du sol pour diminuer la concentration en radon dans l'habitat, Ph.D. Thesis, report LBL-34244, Lawrence Berkeley National Laboratory, Berkeley, CA.

Loureiro C. O. (1987) Simulation of the steady-state transport of radon from soil into houses with basements under constant negative pressure, Ph.D. Thesis, report LBL-24378, Lawrence Berkeley National Laboratory, Berkeley, CA.

Patankar S. V. (1980) *Numerical Heat Transfer and Fluid Flow,* Hemisphere Publishing, New York, NY.

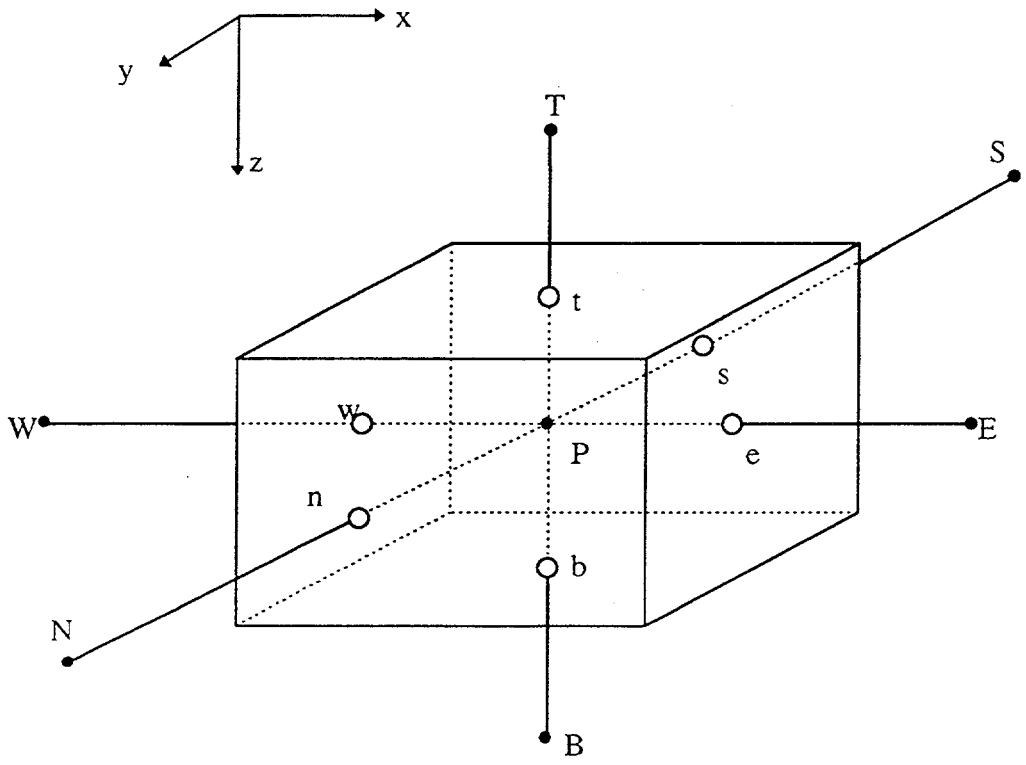

Figure 5A.1. Spatial discretization about the point P.

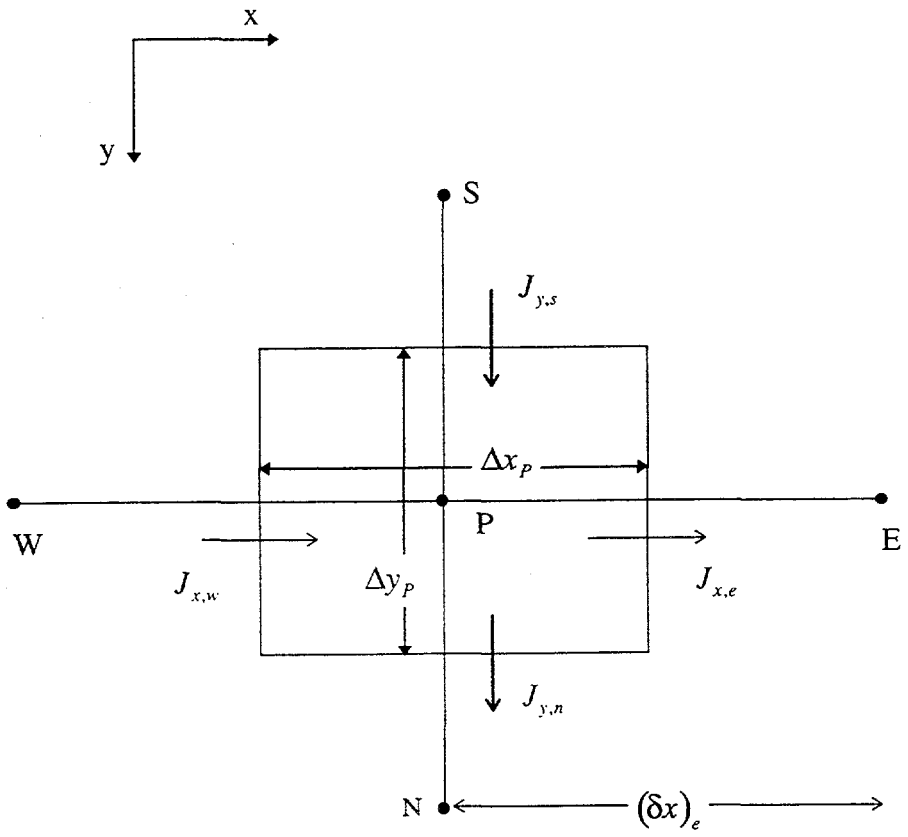

Figure 5A.2. The radon fluxes into and out of the control volume centered at P. For simplicity, only two dimensions are shown.

CHAPTER 6

A NOVEL TECHNIQUE FOR SIMULATING SUBSURFACE CONTAMINANT TRANSPORT IN SYSTEMS SUBJECT TO TRANSIENT BOUNDARY CONDITIONS: THE RapidSTART MODEL

6.1 Abstract

A numerical model is developed to simulate soil-gas and radon transport around buildings in the presence of fluctuating pressure boundary conditions. The model, named RapidSTART, incorporates a novel simulation technique based on Duhamel's theorem and runs several orders of magnitude faster than comparable three-dimensional, finite-difference models. This substantial decrease in simulation runtime makes the analysis of the impacts of transient winds on soil-gas and radon transport tractable. The model can simulate the effects of various transient pressure boundary conditions; we apply RapidSTART here for the case of a ground-surface pressure field driven by both fluctuating wind speeds and directions.

RapidSTART's runtime memory requirements can be prohibitively large for low soil permeabilities (i.e., less than ~ 10^{-12} m^2). We introduce a method to circumvent this problem using curve fits for the memory-intensive parameters. Finally, one-, two-, and three-dimensional validation tests of the model are presented. The results of these tests demonstrate that RapidSTART accurately simulates complex soil-gas and radon

flows. We expect this technique can also be productively applied to the simulation of other complex, linear systems.

6.2 Nomenclature

b_1, b_2	intercepts used in the interpolation scheme (Pa)
i	index that references the time at which $\Delta p_{w,i}$ took place (-)
j	index variable (-)
l	dummy variable of summation (-)
L_c	characteristic length of the system (m)
M	number of ground-surface pressure fields and unit-step responses (-)
m_1, m_2	slopes used in the interpolation scheme (Pa s^{-1})
N	number of intervals the unit-step response is divided into (-)
$p(x,y,z,t)$	soil-gas disturbance pressure (Pa) at the point (x,y,z) at time t
$p_w(t)$	dynamic pressure (Pa) of the wind at eave height at time t
$\Delta p_{w,i}$	magnitude of the change in wind dynamic pressure (Pa) at τ_i
q_1, q_2	values of the unit-step response used in the interpolation scheme (Pa)
$S_j(x,y,z)$	weight assigned to the effect of changing wind dynamic pressure (Pa s)
$S_1(x,y,z)$, $S_\infty(x,y,z)$	weight for the initial and final intervals, respectively (Pa s)
t	time (s)
t_k, t_{k+1}, t_{k+2}	times where the calculated unit-step response is evaluated (s)
Δt	time step between successive simulation points (s)

$U(x,y,z,t)$	unit-step response of the system (Pa)
u_k, u_{k+1}, u_{k+2}	values of the calculated unit-step response (Pa) at times t_k, t_{k+1}, t_{k+2}
V_{eh}	eave-height wind speed (m s^{-1})
x, y, z	coordinates for a point in the soil block (m)

Greek letters

δ	pressure diffusivity (m^2 s^{-1})
ε	air filled porosity (-)
$\lambda(x,y,z)$	parameter used to estimate the weighting functions (-)
ρ	air density (kg m^{-3})
τ_c	characteristic time for the pressure field to reach steady state (s)
τ_i	time before present when change in boundary conditions occurred (s)
$\Delta\tau_i$	time step over which the slope of the dynamic pressure is evaluated (s)

Note: (-) indicates a nondimensional variable.

6.3 Introduction

The finite-difference model START can simulate soil-gas and radon transport in one-, two-, and simple three-dimensional geometries. However, for complicated three-dimensional simulations, such as those necessary to examine the impacts of transient winds on radon entry into buildings, START's runtime requirements can be prohibitively large. In response to this problem, we have developed a technique using Duhamel's theorem (Duhamel, 1833) that allows substantially more rapid simulations of these complex flows. The method is implemented in the model named RapidSTART.

In this chapter we describe the development and validation of the RapidSTART model. Section 6.4 introduces Duhamel's theorem and several previous applications of the technique. Section 6.5.1 derives Duhamel's theorem in the context of soil-gas transport driven by a fluctuating wind speed. The discretization of the theorem, and implementation of the discretized equations in RapidSTART, are described in Section 6.5.2.

Since real winds vary in both speed and direction, we have developed a method to simulate the effects of a fluctuating wind direction on soil-gas and radon transport. The method distributes the wind-direction signal into bins, each corresponding to a previously determined ground-surface pressure field and unit-step response. Section 6.5.3 describes this portion of the model.

In addition to the time required to run a simulation, the runtime memory requirements of a model can be a constraint. The time required for the soil-gas pressure field to reach steady state and the spatial and temporal discretization of the simulation determine RapidSTART's runtime memory requirements. For low soil permeabilities these memory requirements can be large (~o(10,000 MB)). Section 6.5.4 describes a technique to represent the memory-intensive parameters with curve fits, thereby reducing the program's runtime memory requirements.

Section 6.6 presents four validation tests of RapidSTART. Section 6.6.1 repeats, for RapidSTART, several of the one-dimensional soil-column tests used to validate START. Section 6.6.2 compares RapidSTART and START simulation predictions for the case of a sinusoidally varying wind speed incident on a two-dimensional section of the house model described in Chapter 4. In Section 6.6.3 we test the model's convergence to steady state for three wind-incidence angles. Finally, Section 6.6.4 presents RapidSTART simulation predictions of an experiment performed at the Small Structures Facility. Comparisons are made to measurements of soil-gas and radon entry rates into the basement structure. These four tests demonstrate that RapidSTART can accurately and efficiently simulate the complex soil-gas and radon flows generated by the interaction of wind with buildings.

6.4 Duhamel's theorem and Previous Applications

Duhamel recognized that the response of a linear system to time-dependent boundary conditions could be decomposed into a sum of small responses, each of

which corresponds to the effects of a previous change in the boundary conditions. The study of heat transport in solids driven by fluctuating surface temperatures or heat fluxes has successfully applied this concept (Myers, 1987). In electrical engineering, the analysis of linear circuits employs an analogous method, termed the "convolution integral" (Nilsson, 1984).

The theorem has also been used to investigate subsurface water flow and stream flows. Weeks (1979) employed a version of the theorem to explain the impacts of barometric pressure fluctuations on wells in deep, unconfined aquifers. He found the technique well-suited to predicting the unconfined aquifer's water level. Moench et al. (1974) used the method to model variations in a perennial stream interacting with an aquifer. They showed good agreement between modeled and experimental observations of the stream-aquifer system. Pinder et al. (1969) applied the theorem to determine the diffusivity of an aquifer in Nova Scotia. Comparisons to experimental data from pumping tests showed good agreement with their modeling results. More recently, Duhamel's theorem has been successfully employed to examine the effects of atmospheric pressure fluctuations on soil-gas entry into an experimental basement structure (Robinson et al., 1995a; Robinson et al., 1995b).

None of the studies described above applied Duhamel's theorem to simulate a parameter field of the flow (e.g., fluid velocities or contaminant concentrations). Rather, the method was applied to analyze a single parameter's response to the flow. Pinder et al. (1969), for example, predicted the response of the head in an aquifer to fluctuations in a nearby river. In contrast to these investigations, RapidSTART

computes details of the flow field throughout the soil block for every time step. The previous studies also considered only spatially homogeneous boundary conditions. In contrast, spatial heterogeneity in the ground-surface pressure boundary condition is an important characteristic of wind's interactions with a building, and these effects are included in RapidSTART.

6.5 Application of Duhamel's theorem to Soil-Gas and Radon Transport

RapidSTART applies a four-step process to compute the radon entry rate into the building in the presence of fluctuating winds. First, the finite-difference model START is used to calculate the unit-step response of the soil-gas pressure field. RapidSTART then applies Duhamel's theorem (which requires the unit-step response as input) to compute the soil-gas pressure and velocity fields as a function of the input wind signal. The finite-difference technique described in Chapter 5 uses this soil-gas velocity field to determine the soil-gas radon concentration field. Finally, integrating the radon flux into the basement over the length of the footer-slab crack yields the radon entry rate into the building.

Sections 6.5.1 - 6.5.4 discuss the derivation and implementation into RapidSTART of Duhamel's theorem. Duhamel's theorem applies to the simulation of the soil-gas pressure field, since wind-induced soil-gas flow falls within the linear Darcy regime. This linearity implies, for example, that at steady state a doubling of the basement depressurization results in a doubling of the soil-gas entry rate. However, the radon entry rate is not linearly related to the depressurization driving the system. The

flow of soil gas into the house depletes the soil-gas radon concentration in the vicinity of the basement, thereby reducing the radon source available for entry. As a result, the radon concentration field cannot be simulated with the Duhamel technique. Typically, however, START consumes more than 99% of a simulation's runtime calculating the soil-gas pressure and velocity fields. RapidSTART therefore combines the Duhamel technique for solution of the soil-gas pressure field with the finite-difference technique described in Chapter 5 to calculate the radon concentration field.

The general formulation of Duhamel's theorem allows for the simulation of discrete changes in boundary conditions. However, most boundary conditions that affect soil-gas and radon transport (e.g., wind speed, barometric pressure, and outside temperature) vary continuously. As a counter example, the sudden starting of a furnace, causing a nearly instantaneous change in basement depressurization, represents a discontinuous change in boundary conditions. We have not included the formulation of discrete boundary condition changes in RapidSTART. The model can, though, approximate a discrete change in boundary condition by reducing the size of the simulation time step and applying the discrete change over this reduced time step.

6.5.1 Derivation of Duhamel's theorem for Soil-Gas Transport

We base our derivation of Duhamel's theorem on Myers' (1987) description of heat flow in solids. In that case, a surface temperature or surface heat flux defines the boundary condition controlling the heat flow and temperature profile in the solid. To simulate soil-gas transport, the wind speed - or equivalently the wind dynamic pressure

- represents the driving force for transport in the presence of fluctuating winds. *Let* $p_w(t)$ correspond to the eave-height wind dynamic pressure (Pa) at time t (s), defined as:

$$p_w(t) = \frac{1}{2}\rho V_{eh}^{\ 2} \tag{6.1}$$

where V_{eh} is the eave-height wind speed (m s^{-1}) and ρ is the air density (kg m^{-3}). In RapidSTART, the single parameter $p_w(t)$ controls the time-dependent basement depressurization and heterogeneous ground-surface pressure field for a given wind direction. Equation (3.3) and the ground-surface pressure coefficient field (Figures 3.5 and 3.6) map $p_w(t)$ to a pressure at each point on the soil surface. A pressure coefficient for the house relates $p_w(t)$ to the basement depressurization.

The unit-step response, $U(x,y,z,t)$ (Pa), characterizes the system's response to changes in the boundary conditions represented by $p_w(t)$. In particular, $U(x,y,z,t)$ is the time history of the soil-gas pressure field after a discrete change in the wind dynamic pressure from 0 to 1 Pa. We use START to evaluate the unit-step response from $t = 0$ to the time the system reaches steady state at the wind dynamic pressure of 1 Pa. This characteristic time varies inversely with soil permeability, being on the order of 10 s at 10^{-8} m^2 and 10^5 s at 10^{-12} m^2.

The time required for START to generate a unit-step response can be large, particularly for low soil permeabilities. Because the time required for the soil-gas

pressure field to reach steady state scales inversely with soil permeability, simulations of the unit-step response at a permeability of 10^{-10} m^2 must be run to a time about 100 times larger than for a soil permeability of 10^{-8} m^2. Limitations imposed on the temporal discretization of the simulation imply that, as the soil permeability decreases, the soil-gas pressure field requires more time steps to reach steady state. In other words, the temporal discretization cannot be scaled with soil permeability, resulting in an increased simulation runtime with decreasing soil permeability. The time required for START to generate the unit-step response at low soil permeabilities presents the main practical limitation to the use of RapidSTART. The same constraint, however, made three-dimensional simulations with START impractical, and provided the motivation for the development of RapidSTART. An approach to practical implication of RapidSTART for low permeability soils is described in Section 6.5.4.

RapidSTART computes the time-dependent soil-gas pressure field generated by a fluctuating wind by combining the structure of the changing ground-surface pressure field (known via $p_w(t)$) with knowledge of the system's response to these changes embodied in the unit-step response. Let $\Delta p_{w,i}$ (Pa) be the magnitude of the small change in wind dynamic pressure that occurred between the times $t-(\tau_i+\Delta\tau_i)$ and $t-(\tau_i-\Delta\tau_i)$. Here, τ_i (s) is the amount of time before the current simulation time at which $\Delta p_{w,i}$ took place, i is an index referencing this time, and $\Delta\tau_i$ (s) is the time step over which the slope of the dynamic pressure will be evaluated. Figure 6.1 illustrates

this discretization of the wind dynamic pressure signal. The response of the soil-gas pressure to $\Delta p_{w,i}$ at time t can be approximated as

$$\Delta p_{w,i} U(x, y, z, t - \tau_i) \tag{6.2}$$

where $U(x, y, z, t)$ is the unit step response of the soil-gas pressure field (Pa).

The linearity of the system implies that the cumulative effect of all the small changes in wind dynamic pressure since time $t = 0$ can be found by summing the individual responses of the soil-gas pressure field to these changes

$$p(x, y, z, t) = \sum_i \Delta p_{w,i} U(x, y, z, t - \tau_i) \tag{6.3}$$

where $p(x, y, z, t)$ is the soil-gas disturbance pressure (Pa) at the point (x, y, z) at time t.

Multiplying and dividing the right hand side of equation (6.3) by $\Delta\tau_i$ yields

$$p(x, y, z, t) = \sum_i U(x, y, z, t - \tau_i) \frac{\Delta p_{w,i}}{\Delta \tau_i} \Delta \tau_i \tag{6.4}$$

Allowing $\Delta\tau_i$ to become infinitesimally small, the summation becomes an integral over time, and the fraction becomes a time derivative:

$$p(x, y, z, t) = \int_0^t U(x, y, z, t - \tau) \frac{\partial p_w}{\partial \tau} \mathrm{d}\tau \tag{6.5}$$

Equation (6.5) represents the form of Duhamel's theorem that we use in the development of RapidSTART. Note that this equation permits only continuous changes over time in the boundary conditions. However, the discretized version of equation (6.5), described in the next section, provides a method to simulate discrete changes in the boundary conditions.

6.5.2 Discretization of Duhamel's theorem

To implement Duhamel's theorem in RapidSTART, we divide the integral in equation (6.5) into discrete time steps:

$$p(x,y,z,t) = \int_{t-\Delta t}^{t} U(x,y,z,t-\tau)\frac{\partial p_w}{\partial \tau}\,d\tau + \int_{t-2\Delta t}^{t-\Delta t} U(x,y,z,t-\tau)\frac{\partial p_w}{\partial \tau}\,d\tau + \ldots + \int_{0}^{\Delta t} U(x,y,z,t-\tau)\frac{\partial p_w}{\partial \tau}\,d\tau \tag{6.6}$$

where Δt is the time step (s) between successive simulation points; we choose Δt based on the soil-gas pressure field's response time and the characteristics of the fluctuating wind. Equation (6.6) represents the sum of $N = \frac{t}{\Delta t} - 1$ integrals. By assuming a constant time derivative of the wind dynamic pressure during each time step, equation (6.6) can be written as

$$p(x,y,z,t) = \sum_{j=0}^{N-1}\left[\left.\frac{\partial p_w}{\partial t}\right|_j\right]\int_{t-(j+1)\Delta t}^{t-j\Delta t} U(x,y,z,t-\tau)\,d\tau \tag{6.7}$$

where j is a dummy variable of summation (-), and $\left.\frac{\partial p_w}{\partial t}\right|_j$ is evaluated at the time $t-\left(j+\frac{1}{2}\right)\Delta t$, or

$$\left.\frac{\partial p_w}{\partial t}\right|_j = \frac{p_w(t-j\Delta t)-p_w(t-(j+1)\Delta t)}{\Delta t} \tag{6.8}$$

To simplify the notation, we define

$$S_j(x,y,z) = \int_{t-(j+1)\Delta t}^{t-j\Delta t} U(x,y,z,t-\tau)\mathrm{d}\tau \tag{6.9}$$

where $S_j(x,y,z)$ is the weight (Pa s) assigned to the effect of the change in wind dynamic pressure at the time $t-\left(j+\frac{1}{2}\right)\Delta t$ on the soil-gas pressure at the point (x,y,z). RapidSTART stores these weights in runtime memory, as they are used throughout the simulation.

We evaluate $S_j(x,y,z)$ with a linear, trapezoidal integration scheme, as illustrated in Figure 6.2. In this figure, u_k, u_{k+1}, and u_{k+2} (Pa) are the values of the unit-step response at a particular point in space at the times t_k, t_{k+1}, and t_{k+2} (s), respectively. The integration in equation (6.9) is performed by linearly interpolating values in the unit-step response to the required times. The values of the unit-step response, q_1 and q_2 (Pa), at the times $t-(j+1)\Delta t$ and $t-j\Delta t$, are approximated as

$$q_1 = m_1\left(t-(j+1)\Delta t\right)+b_1 \tag{6.10}$$

and

$$q_2 = m_2\left(t-j\Delta t\right)+b_2 \tag{6.11}$$

where

$$m_1 = \frac{u_{k+1}-u_k}{t_{k+1}-t_k} \tag{6.12}$$

$$b_1 = u_k - m_1 t_k \tag{6.13}$$

$$m_2 = \frac{u_{k+2}-u_{k+1}}{t_{k+2}-t_{k+1}} \tag{6.14}$$

$$b_2 = u_{k+1} - m_2 t_{k+1} \tag{6.15}$$

With these approximations, the weight can be written as

$$S_j(x,y,z) = \left(\frac{q_1+u_{k+1}}{2}\right)\left(t_{k+1}-\left(t-(j+1)\Delta t\right)\right)+\left(\frac{u_{k+1}+q_2}{2}\right)\left(\left(t-j\Delta t\right)-t_{k+1}\right) \tag{6.16}$$

There are instances, particularly toward the later times in the unit-step response, where no discrete time points used by START fall within the desired range. In these

cases, we approximate the integral by linear interpolation between the two calculated points that bound the time interval.

6.5.3 Simulations with a Fluctuating Wind Direction

In the research presented here, simulations with a varying wind direction employ the ground-surface pressure fields determined in Chapter 3 for wind-incidence angles of 0°, 45°, and 90°. Ideally, unit-step responses would be generated for more than three different wind-incidence angles. However, additional wind tunnel experiments or numerical simulations would be required to determine these ground-surface pressure fields, and the corresponding unit-step responses would need to be generated. To be general we formulate the technique to simulate a fluctuating wind direction for an arbitrary number of ground-surface pressure fields and unit-step responses.

We consider two specific types of simulations with a fluctuating wind direction: the first constrains the wind direction to vary within a 135° range, and the second allows the wind to switch direction by 180°. For the first case, the wind direction signal is discretized into three bins, each centered at a wind-incidence angle corresponding to one of the three known ground-surface pressure fields. The center of the wind direction signal is normalized to 45°. If the normalized wind direction falls between -22.5° and 22.5°, RapidSTART uses the unit-step response and ground-surface pressure field corresponding to a wind-incidence angle of 0°. If the wind

direction falls between 22.5° and 67.5°, RapidSTART uses the unit-step response and ground-surface pressure field for 45°, and when the wind direction is between 67.5° and 112.5°, the unit-step response and ground-surface pressure field for 90° are used. Therefore, any wind signal with a directional range of less than 135° can be simulated with this technique.

RapidSTART simulates an alternation of 180° in wind direction by taking advantage of the symmetry (with respect to the 0° wind direction) in the house geometry, the ground-surface pressure field, and the unit-step response. These simulations then proceed, qualitatively, in the same manner as for the case with a wind directional range of 135°.

As for varying wind speed, simulations with a changing wind direction take advantage of the linearity of the system. RapidSTART calculates the soil-gas pressure at any point and time as the sum of the effects of wind from each direction weighted for how much time the wind has been from a particular direction. Equation (6.17) illustrates this concept for the case where the wind direction has been separated into three bins (note the similarity of each of the terms in equation (6.17) to equation (6.7)):

$$p(x,y,z,t) = \sum_{j=0}^{N-1}\left[\left.\frac{\partial p_{w,1}}{\partial t}\right|_j\right]\int_{t-(j+1)\Delta t}^{t-j\Delta t} U_1(x,y,z,t-\tau)\,d\tau + \sum_{j=0}^{N-1}\left[\left.\frac{\partial p_{w,2}}{\partial t}\right|_j\right]\int_{t-(j+1)\Delta t}^{t-j\Delta t} U_2(x,y,z,t-\tau)\,d\tau + \sum_{j=0}^{N-1}\left[\left.\frac{\partial p_{w,3}}{\partial t}\right|_j\right]\int_{t-(j+1)\Delta t}^{t-j\Delta t} U_3(x,y,z,t-\tau)\,d\tau \quad (6.17)$$

Here, the numerical subscripts on $\frac{\partial p_w}{\partial t}$ and U reference the wind direction. For the case of a wind signal whose direction varies within a 135° range, the subscript 1 corresponds to a wind-incidence angle of 0°, 2 corresponds to 45°, and 3 corresponds to 90°. For the case of a 180° flip in direction, equation (6.17) would be the sum of two terms, one each for wind-incidence angles of 0° and 180°. For the general case, with M (-) ground-surface pressure fields and unit-step responses, the time-dependent soil-gas pressure field can be written as

$$p(x,y,z,t) = \sum_{l=1}^{M}\sum_{j=0}^{N-1}\left[\left.\frac{\partial p_{w,l}}{\partial t}\right|_j\right]\int_{t-(j+1)\Delta t}^{t-j\Delta t} U_l(x,y,z,t-\tau)\,d\tau \quad (6.18)$$

where l is a dummy variable of summation (-).

RapidSTART places two constraints on the wind dynamic pressure signal. First, the dynamic pressure can be non-zero in only one direction at any particular time. Second, except for the first time step after a change of wind direction, the time derivative of the wind dynamic pressure can be non-zero only in the new wind

direction. Therefore, the soil-gas pressure field at a particular time depends on both the current wind direction and speed, and, if the wind has been from another direction in the near past (i.e., less than several times the characteristic response time of the system), that wind direction and speed. For example, if the wind shifts direction from 0° to 45°, the effect on the soil-gas pressure field of the unit-step response corresponding to 0° will decay, while the effect of the unit-step response corresponding to 45° will grow.

The time over which this transition takes place can be estimated by considering a characteristic time, τ_c (s), for the pressure field to reach steady state after a perturbation. Using the pressure diffusivity, δ ($m^2\ s^{-1}$), derived in Chapter 5, we define

$$\tau_c = \frac{L_c^2}{\delta} \tag{6.19}$$

where L_c is a characteristic length (m) of the system. We take L_c to be 15 m, equivalent to half the horizontal extent of the soil block. For a soil permeability of 10^{-8} m^2, τ_c is about 2 s. If the wind direction changes from 0° to 45°, the influence of the unit-step response corresponding to 0° will essentially be nil after several characteristic times, or about 6 s. The characteristic time varies inversely with soil permeability, so, for a soil permeability of 10^{-10} m^2, τ_c is 200 s. At this soil permeability, the soil-gas pressure field requires about 600 s to stabilize once the wind direction has shifted.

6.5.4 Simplified Representation of the Weighting Function

As described in Section 6.5.2, RapidSTART stores the weighting function, $S_j(x,y,z)$, in runtime memory. The amount of memory required to store the weights depends on the length of the unit-step response, the spatial discretization of the soil and building system, and the temporal discretization of the simulation. For a tight soil this memory requirement can be large. For example, at a soil permeability of 10^{-12} m^2, the unit-step response reaches steady state after about 10^5 s. The physical discretization of the soil block contains about 40,000 control volumes. If we consider a simulation that uses a time step of 5 s and allows for three wind directions, $S_j(x,y,z)$ requires about 19,000 Mbytes of storage. Current computers cannot practically store this amount of information in runtime memory. We note that, for this dissertation, simulations have only been performed at soil permeabilities of 10^{-8} and 10^{-10} m^2, and that neither of these scenarios present runtime memory problems. However, we intend to perform simulations with tighter soils in the future, and therefore require a method to significantly reduce this memory requirement.

Parameterizing the weighting function at each point in the soil block over the time required for the system to reach steady state is a practical and effective method of reducing the program's memory requirements. An exponential ingrowth to a steady-state value closely approximates the weighting function:

$$S_j(x,y,z) = S_\infty(x,y,z) + \left[S_1(x,y,z) - S_\infty(x,y,z)\right] \exp\left\{-\lambda(x,y,z)(j-1)\right\} \qquad (6.20)$$

where $\lambda(x,y,z)$ (-) is a fit parameter, and $S_1(x,y,z)$ and $S_\infty(x,y,z)$ are the weighting functions (Pa s) for the initial and final time intervals, respectively. This characterization of the weighting function requires only three parameters for every point in the soil block: $S_1(x,y,z)$, $S_\infty(x,y,z)$, and $\lambda(x,y,z)$, and therefore significantly reduces the runtime memory requirements of the simulation. For tighter soils, more complicated curve-fitting methods may be necessary to approximate the time evolution of the weighting function. We have described this exponential technique here because the method reduced the memory requirements substantially, and, in a simple validation test, was effective for a soil permeability of 10^{-8} m^2.

6.6 Validation of RapidSTART

This section presents four sets of validation tests of the RapidSTART model. We first use RapidSTART to simulate several of the one-dimensional test cases presented in Chapter 5. Second, we perform model simulations of transient soil-gas and radon flow in a two-dimensional section of a full-scale house and soil system. Comparisons of RapidSTART's soil-gas and radon entry predictions to those from the finite-difference model (START) are presented. Third, RapidSTART's convergence to a steady-state soil-gas entry rate is compared to START predictions. Finally, we use RapidSTART to predict soil-gas and radon entry into the Small Structures test basement, and make comparisons to experimental measurements. Table 6.1 describes these validation tests, labeled as "validation scenarios" 1 - 4.

Table 6.1. The four validation tests of RapidSTART

Validation Scenario	Description	Section	Figure(s)
1	Analytical solution validation	6.6.1	6.3 - 6.4
2	Comparison to START for a two-dimensional section of the house and soil geometry	6.6.2	6.5 - 6.10
3	Steady-state convergence for three wind-incidence angles	6.6.3	6.11
4	Comparison to experimental measurements from the Small Structures Facility	6.6.4	6.12

6.6.1 Analytical Solution Validation (Validation Scenario 1)

Figures 6.3 and 6.4 present comparisons of RapidSTART predictions to the analytical solution (equation (5.28)) of the pressure 37.5 cm from the front end of a soil column subject to a fluctuating pressure boundary condition. Equations (5.25) - (5.27) give the boundary and initial conditions for this test. The simulations were performed for soil permeabilities of 10^{-8} and 10^{-10} m^2. Figures 6.3 and 6.4 are analogous to Figures 5.4 and 5.5, which demonstrated the accuracy of the finite-difference code START. Figures 6.3 and 6.4 show that, for the two soil permeabilities tested, RapidSTART simulated this scenario with the same high level of accuracy as did START.

6.6.2 Comparison to START for a Two-Dimensional Geometry (Validation Scenario 2)

This section compares START and RapidSTART simulation results for a two-dimensional section of the full-scale house model presented in Chapter 4. For these tests, we used a section of the soil block centered on the house and parallel to the 10.4 m side of the house. The ground-surface pressure field corresponded to boundary layer 1 at a wind-incidence angle of 0° (see Figure 3.5 (f)). Figures 6.5 and 6.6 show the fluctuating wind speed and dynamic pressure used as input for the tests, which were conducted for soil permeabilities of 10^{-8} and 10^{-10} m^2. The two tests use different wind dynamic pressure profiles since generating the START solution for the tighter soil is computationally very expensive. A shorter START simulation time for the 10^{-10} m^2 soil demonstrates the accuracy of the RapidSTART model without requiring excessive CPU time.

Figures 6.7 and 6.8 present the comparisons for a soil permeability of 10^{-8} m^2. Figures 6.9 and 6.10 show the analogous simulations for a soil permeability of 10^{-10} m^2. These figures demonstrate excellent agreement between RapidSTART and START. Additionally, the RapidSTART simulation was 350 times faster than START at a soil permeability of 10^{-8} m^2, and 3500 times faster than START at 10^{-10} m^2.

6.6.3 Steady-State Convergence for Three Wind-Incidence Angles (Validation Scenario 3)

We validate the fluctuating wind direction portion of RapidSTART by insuring that the model converges to the correct steady-state soil-gas entry rate for each of the

wind directions under consideration. This validation scenario considers a constant 3.6 m s^{-1} wind speed, a wind-incidence angle that switches from 0° to 45° to 90°, and a soil permeability of 10^{-8} m^2. The simulation allows sufficient time between each change of wind direction for the soil-gas pressure field to stabilize. We compare the predicted soil-gas entry rate at each of the wind directions to the result from a steady simulation performed by START. Figure 6.11 presents the result of this simulation; the steady-state values calculated by RapidSTART fall within 0.1% of those predicted by START.

6.6.4 Experimental Validation of RapidSTART (Validation Scenario 4)

This section presents a comparison between RapidSTART predictions and experimental measurements from the Small Structures Facility. The scenario considered here takes as input the same experimental data used to validate START in Section 5.5.2. For conciseness, we refer the reader to Section 5.5.2 for details of the experimental setup and measurement techniques.

One significant difference exists between the START simulation shown in Chapter 5 and the RapidSTART simulation described here. The START simulation assumed a homogeneous soil porosity field, while the RapidSTART simulation applies a depth-dependent porosity profile, determined from soil cores taken at the site. The porosity profile used is

$$\varepsilon = 0.45 \qquad \text{for} \qquad z < 1.6 \text{ m} \tag{6.21}$$

$$\varepsilon = -0.33z + 0.98 \quad \text{for} \quad 2.2 > z \geq 1.6 \text{ m} \tag{6.22}$$

$$\varepsilon = 0.25 \quad \text{for} \quad z \geq 2.2 \text{ m} \tag{6.23}$$

where ε is the air filled porosity (-), and z is the depth into the soil (m). This porosity profile was unavailable at the time we conducted the START simulations. Thus, the unit-step response for the RapidSTART simulation differs from the unit-step response that would be determined for the system presented in Figure 5.10.

Figure 6.12 presents the comparison between the simulation predictions and the experimental measurements. RapidSTART predicted the average radon entry rate over the two hour period to within 14% of the measured value. The difference in the porosity profiles between the RapidSTART simulation and the START simulation presented in Section 5.5.2 preclude a detailed comparison between the two models' predictions. Nevertheless, the results presented in this section demonstrate RapidSTART's ability to accurately simulate transient soil-gas and radon transport under real conditions.

6.7 Conclusions

We have developed a novel and efficient technique to simulate transient soil-gas and radon transport around buildings. The technique, based on Duhamel's theorem, is used in RapidSTART to compute the soil-gas pressure and velocity fields.

RapidSTART applies a finite-difference technique to evaluate the soil-gas radon concentration field. In contrast to previous applications of Duhamel's theorem, parameters of the flow field (i.e., the soil-gas pressure and velocity) are calculated at each time step. RapidSTART decreases the computational time for three-dimensional simulations by orders of magnitude compared with a standard finite-difference approach. We also present a method to reduce the runtime memory requirements of the program, which can be large. Preliminary use of this method gave good results for a soil permeability of 10^{-8} m^2. The model's performance was tested in four validation scenarios, including comparison to experimental measurements from a well-characterized basement structure. RapidSTART performed well in all of the test cases.

The simulation technique introduced here is general; we expect the method can be applied productively to many complex, linear system subject to transient boundary conditions. For example, the transport and entry into buildings of other soil-gas contaminants (e.g., VOC's) could be examined with the methods employed in RapidSTART. We are currently investigating the applicability of this modeling technique to other systems of environmental interest.

6.8 References

Duhamel (1833) Memoire sur la methode generale relative au mouvement de la chaleur dans les corps solides plonges dans les milieux dont la temperature varie avec le temps, *J. Ec. Polyt. Paris* **14**, 20.

Moench A. F., Sauer V. B., and Jennings M. E. (1974) Modification of routed streamflow by channel loss and base flow, *Wat. Resour. Res.* **10**, 963-968.

Myers G. E. (1987) *Analytical Methods in Conduction Heat Transfer,* Genium Publishing Corporation, Schenectady, NY.

Nilsson J. W. (1984) *Electric Circuits,* Addison-Wesley Publishing Co., Reading, MA.

Pinder G. F., Bredehoeft J. D., and Cooper H. H. J. (1969) Determination of aquifer diffusivity from aquifer response to fluctuations in river stage, *Wat. Resour. Res.* **5**, 850-855.

Robinson A. L., Sextro R. G., and Fisk W. J. (1995a) Soil-gas entry into houses driven by atmospheric pressure fluctuations, part 1 --- Measurements, spectral analysis, and model comparison, report LBL-38232, Lawrence Berkeley National Laboratory, Berkeley CA.

Robinson A. L., Sextro R. G., and Riley W. J. (1995b) Soil-gas entry into houses driven by atmospheric pressure fluctuations, part 2 --- The influence of soil and structural factors, report LBL-38233, Lawrence Berkeley National Laboratory, Berkeley, CA.

Weeks E. P. (1979) Barometric fluctuations in wells tapping deep unconfined aquifers, *Wat. Resour. Res.* **15**, 1167-1176.

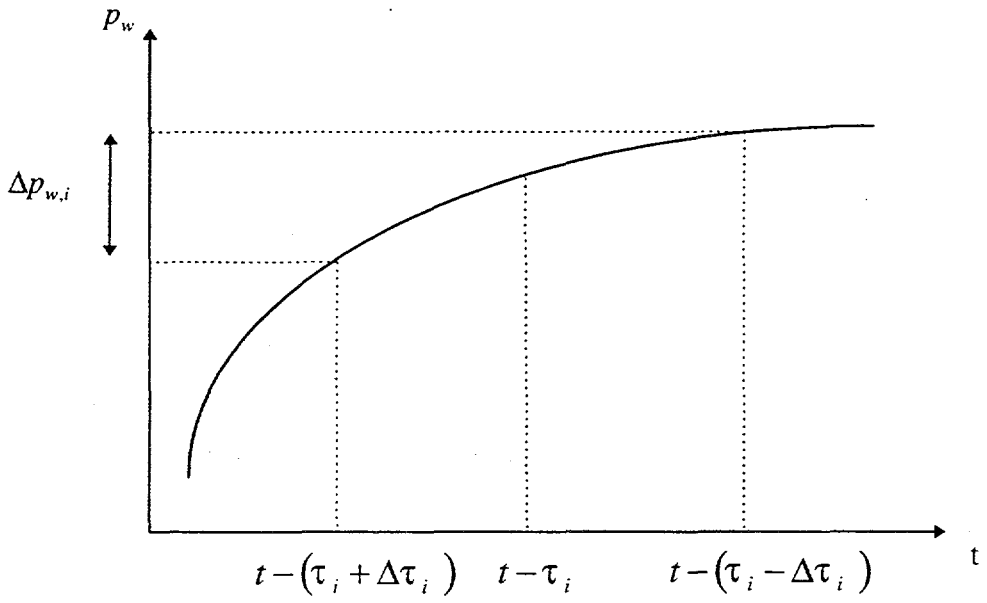

Figure 6.1. Wind dynamic pressure discretization for Duhamel's Theorem.

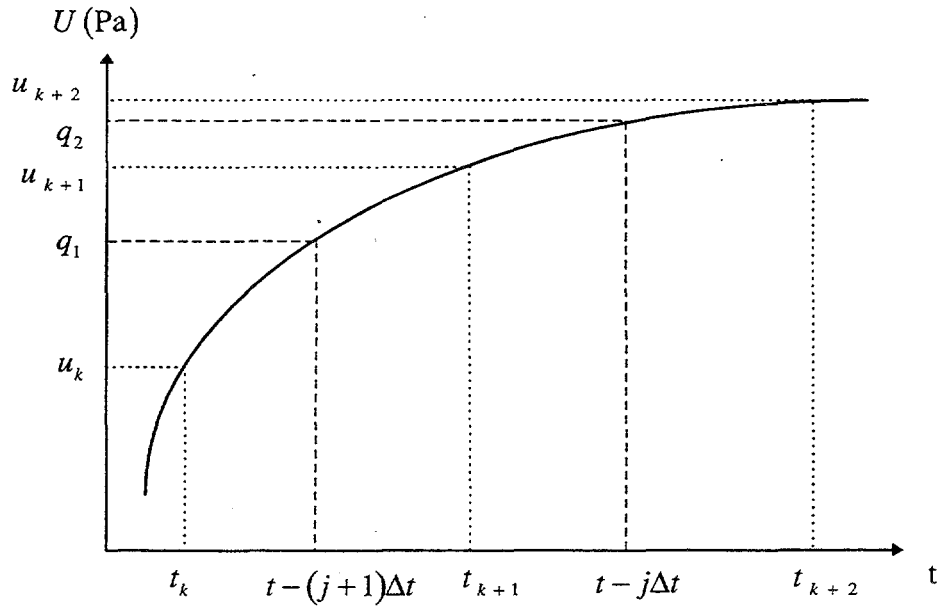

Figure 6.2. Unit step response and weights calculation.

c:\thesis\fig6_1_2.doc

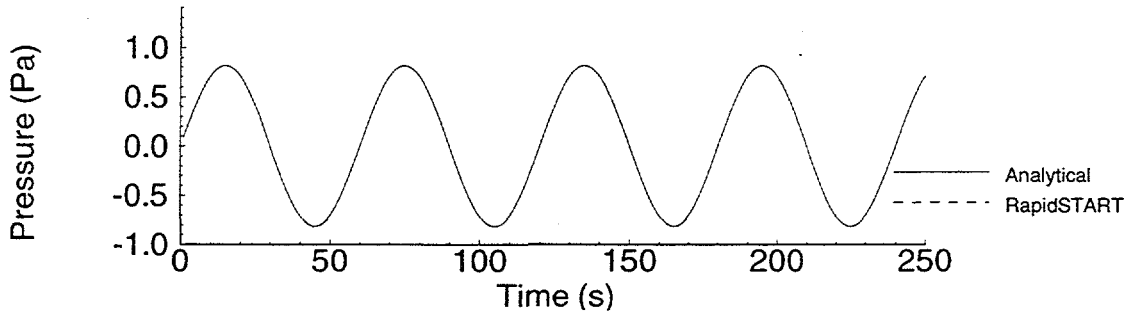

Figure 6.3. Comparison of analytical and numerical predictions of the soil-gas disturbance pressure at 37.5 cm in the soil column (validation scenario 1). The soil permeability is 10^{-8} m^2.

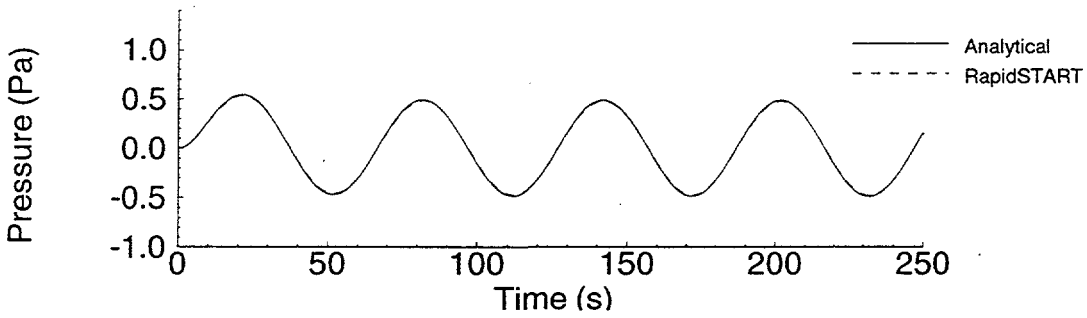

Figure 6.4. Comparison of analytical and numerical predictions of the soil-gas disturbance pressure at 37.5 cm in the soil column (validation scenario 1). The soil permeability is 10^{-12} m^2.

/transient/duhamel/fig7-3-4.lay
analytical-duh-k8 and -k12.out

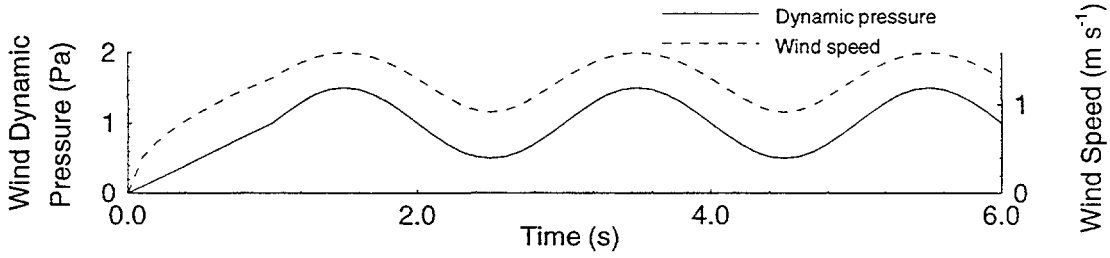

Figure 6.5. Wind dynamic pressure and speed for simulation of the two-dimensional geometry at a soil permeability of 10^{-10} m^2 (validation scenario 2).

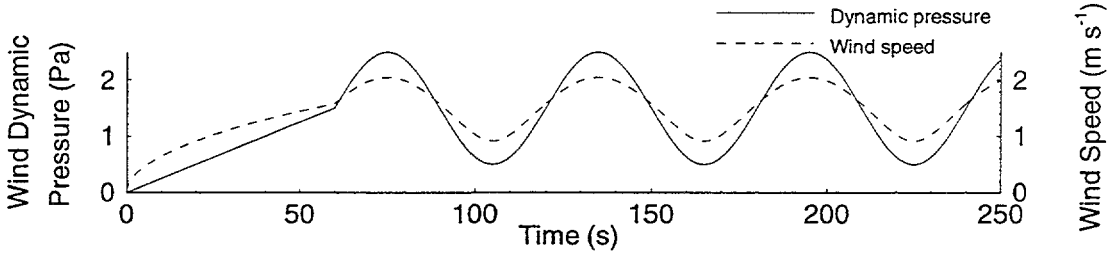

Figure 6.6. Wind dynamic pressure and speed for simulation of the two-dimensional geometry at a soil permeability of 10^{-8} m^2 (validation scenario 2).

/transient/duhamel/fig7-5-6.jav
/transient/duhamel/discrete-data-k8.plt
/transient/duhamel/discrete-data-k10.plt

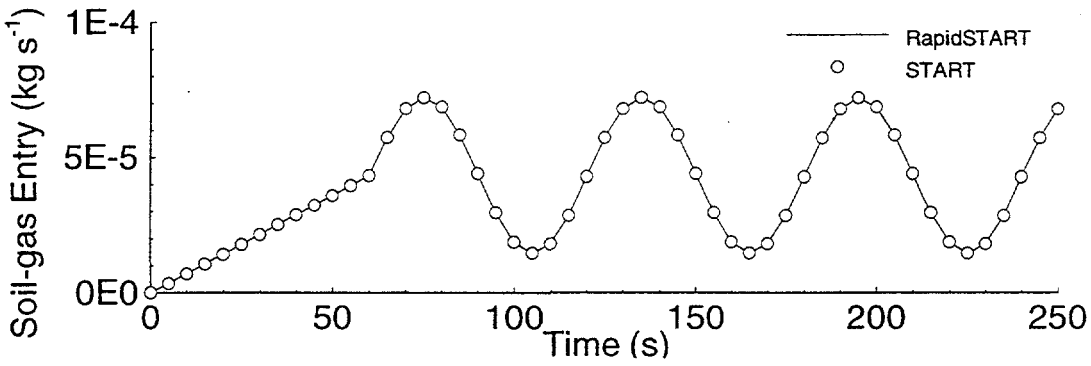

Figures 6.7. Soil-gas flow into the basement for a fluctuating wind at a soil permeability of 10^{-8} m^2 (validation scenario 2).

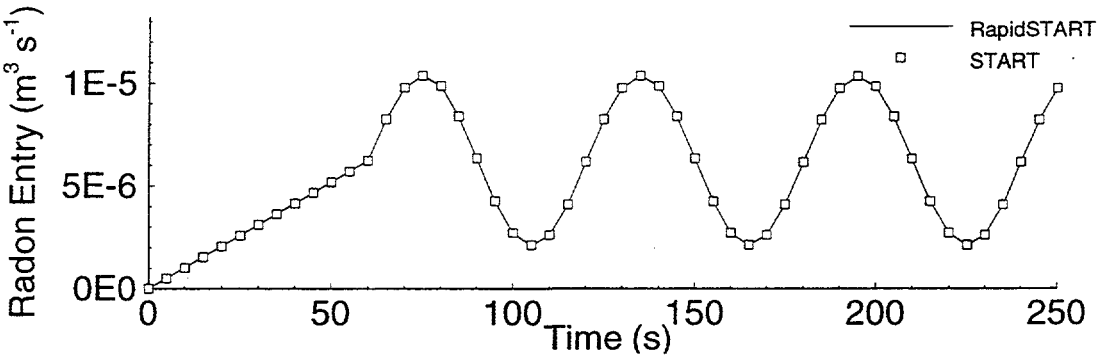

Figures 6.8. Radon entry into the basement for a fluctuating wind at a soil permeability of 10^{-8} m^2 (validation scenario 2).

/transient/duhamel/scott-2d/fig7-7-8.lay
/transient/duhamel/scott-2d/flow-combined-k8.out

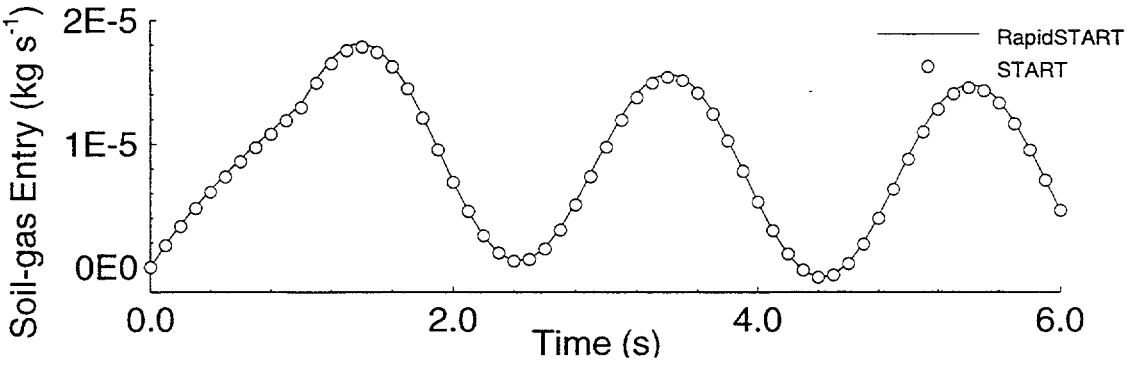

Figures 6.9. Soil gas flow into the basement for a fluctuating wind at a soil permeability of 10^{-10} m^2 (validation scenario 2).

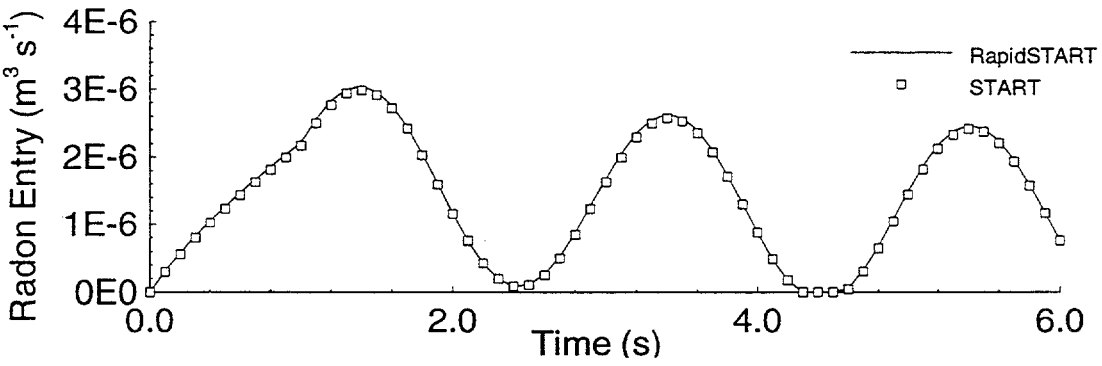

Figures 6.10. Radon entry into the basement for a fluctuating wind at a soil permeability of $10^{-10}m^2$ (validation scenario 2).

/transient/duhamel/scott-2d/fig7-9-10.lay
/transient/duhamel/scott-2d/flow-combined-k10.out

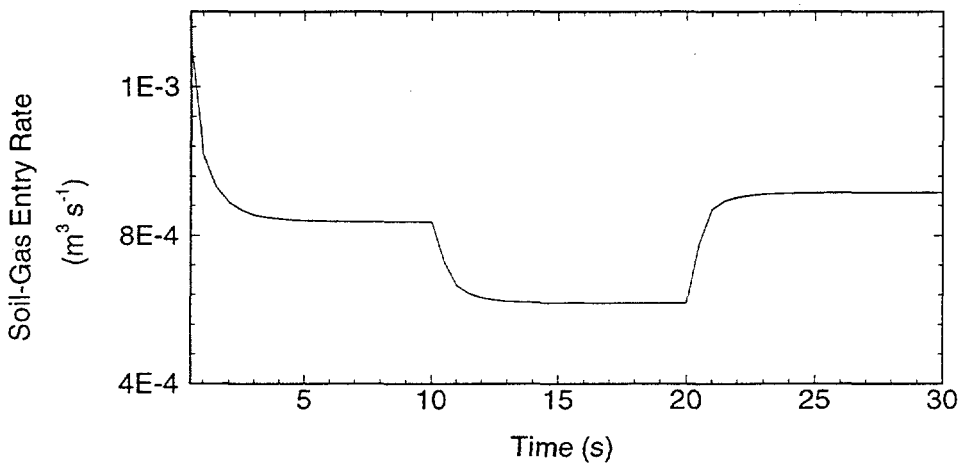

Figure 6.11. Soil-gas entry rate for a wind direction that switches from 0° to 45° to 135°. The soil permeability is 10^{-8} m^2. The predicted steady-state soil-gas entry rates for each wind direction and soil permeability are within 0.1% of the values calculated from the steady-state simulations (validation scenario 3).

/transient/duhamel/fig6-11.lay

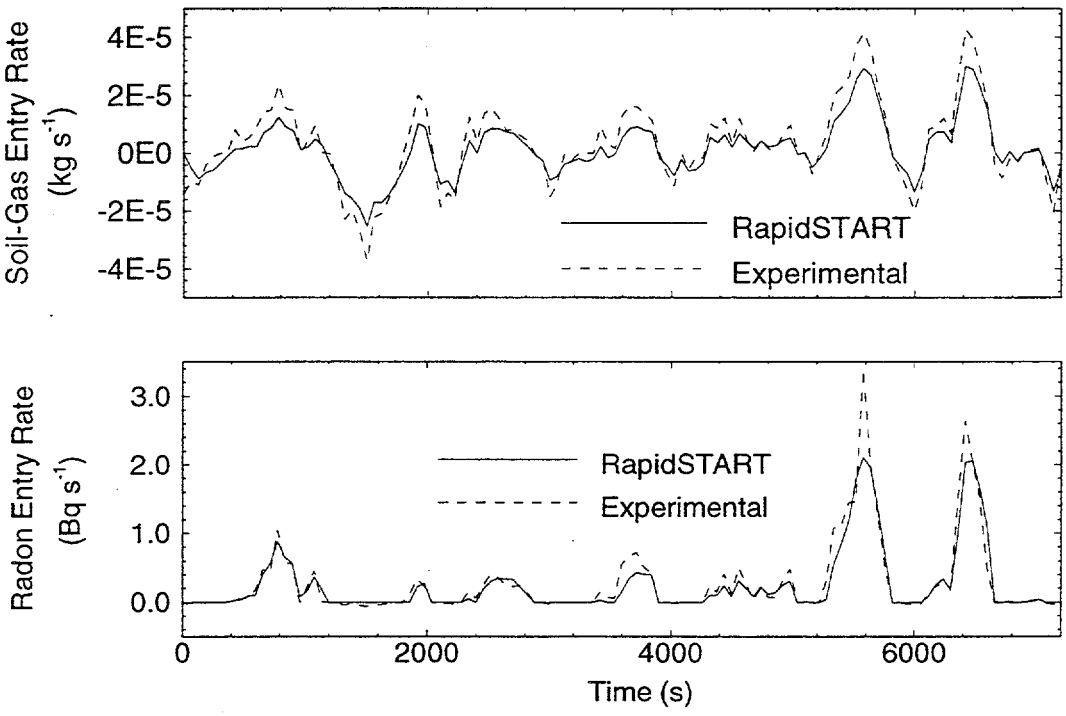

Figure 6.12. Comparison of RapidSTART predictions to measurements from the Small Structures experiment (validation scenario 4).

/user1/allen/-riley/flow-ss-duh-old.out
/user1/allen/-riley/compare-flow-ss-duh-old.out
/user1/allen/-riley/fig-7-12.lay

CHAPTER 7

IMPACT OF FLUCTUATING WINDS ON RADON TRANSPORT AND ENTRY INTO BUILDINGS

7.1 Abstract

The effects of wind on radon transport and entry into buildings can be substantial. As demonstrated in Chapter 4, a steady, wind-induced ground-surface pressure field can dominate predictions of soil-gas and radon entry rates. This chapter extends our investigation by using the START and RapidSTART models, developed in Chapters 5 and 6, to simulate soil-gas and radon flows around a building in the presence of fluctuating winds. Three sets of simulations, each with a different wind signal, are performed for soil permeabilities of 10^{-8} and 10^{-10} m^2. The characteristics of the wind signals were chosen to elucidate the effects of fluctuating wind speeds and directions on radon entry rates. For these two soil permeabilities, wind speed fluctuations typical of the peak in the wind-speed power spectrum have a negligible impact on the predicted radon entry rate. However, ignoring the fluctuating components of a real wind signal altered the predicted radon entry rate by 21%. A fluctuating wind direction that oscillated 180° diurnally increased the predictions by 30%. This chapter also demonstrates RapidSTART's ability to simulate the effects of fluctuating winds on soil-gas and radon transport. To our knowledge, the work

presented here represents the first time this technique has been applied to simulate the transport of a subsurface contaminant.

7.2 Nomenclature

C_{char}	spatial average of the normalized soil-gas radon concentration (-)
C_{∞}	deep-soil radon concentration in the soil gas (Bq m^{-3})
$E(t)$	normalized radon entry rate (m^3 s^{-1})
$\overline{E}$	time-averaged normalized radon entry rate (m^3 s^{-1})
n	frequency (s^{-1})
N	number of periods (-)
P	power in the wind signal (m^2 s^{-2})
$p_w(t)$	wind dynamic pressure (Pa)
$\overline{p_w}$	time-averaged wind dynamic pressure (Pa)
t	time (s)
T	period (s)
u_*	shear velocity (m s^{-1})
V_{eh}	eave-height wind speed (m s^{-1})
V_{eh}'	fluctuating component of the eave-height wind speed (m s^{-1})
z_{eh}	eave height (3 m)
z_0	roughness length (m)

Greek letters

κ	von Karman's constant (0.4)
ρ	air density (1.2 kg m^{-3})

Note: (-) indicates a nondimensional variable.

7.3 Introduction

Chapter 4 demonstrated that steady, wind-induced flushing of radon from soil-gas can strongly affect the predicted radon entry rate into a building. Depending on the soil permeability, this phenomenon can dominate predictions of steady-state indoor radon concentrations. In reality, though, winds fluctuate in both speed and direction, and the impacts of transient winds on radon transport and entry into buildings are unknown. We developed the START and RapidSTART models, described in Chapters 5 and 6, to investigate these features of real winds.

DSMA Atcon Ltd. (1985) conducted the only previously reported radon transport study that included time varying winds. Their modeling investigation constrained the wind speed and direction only to vary discretely on hourly intervals, thereby excluding effects of short term wind fluctuations. The numerical model also ignored key features of radon's subsurface transport, including diffusion through the soil. Finally, the investigators did not attempt to quantify the role of the fluctuating wind speed or direction on radon entry rates. We will address these issues using the RapidSTART model.

This chapter has two main goals. First, we demonstrate RapidSTART's ability to model a geometrically complex, transient soil-gas and radon transport problem. Since Duhamel's theorem has not previously been applied to simulate the transport of a subsurface contaminant, this demonstration represents an important advance.

Second, we use RapidSTART to investigate the role of transient winds in affecting soil-gas and radon entry into buildings. Section 7.4 describes three sets of simulations, each with an input wind signal chosen to highlight the impacts a fluctuating wind speed or direction might have on the radon entry rate. Section 7.5 presents and analyzes the RapidSTART simulation results. Comparisons between time-averaged transient and steady-state predictions isolate the impacts fluctuating winds have on radon entry. Although the simulations performed here do not represent an exhaustive study of the role of transient winds in near-surface soil-gas and radon transport, they illustrate the important features of the topic. The results also establish the relative importance of the fluctuating and steady components of wind and indicate directions for further research.

7.4 Methods

This section describes the RapidSTART simulations used to investigate the impacts of fluctuating winds on soil-gas and radon entry into the prototypical house described in Sections 4.4.2 and 4.4.5. Section 7.4.1 presents the first set of simulations (labeled simulation scenario 1), which predicts soil-gas and radon entry rates in the presence of a hypothetical variable speed, constant direction wind. We perform RapidSTART simulations with actual wind data collected at the Richmond Field Station (RFS) in Section 7.4.2 (simulation scenario 2). Finally, in Section *7.4.3* we model an artificial, constant speed wind signal that fluctuates diurnally between wind-incidence angles of 0° and 180° (simulation scenario 3). This simulation imitates wind

conditions characteristic of coastal regions, and illustrates the effects of large, periodic changes in wind direction. As in Chapter 4, this chapter reports normalized radon entry rates and soil-gas radon concentrations. Table 7.1 summarizes the input wind signals for each of the three simulation scenarios.

Table 7.1. The RapidSTART simulation scenarios.

Simulation Scenario	Description	Sections	Figures
1	Fluctuating wind speed simulations	7.4.1, 7.5.1	7.2, 7.3
2	Simulations with the RFS wind data	7.4.2, 7.5.2	7.1, 7.4, 7.5
3	Diurnally fluctuating wind direction simulations	7.4.3, 7.5.3	7.6, 7.7

7.4.1 Fluctuating Wind Speed (Simulation Scenario 1)

Simulation scenario 1 considers the impacts on radon entry of a wind signal with a constant wind-incidence angle (0°) and a fluctuating speed. We use the characterization of the atmospheric boundary layer presented by Teunissen (1980) to generate the wind speed component of the signal. Teunissen reports, for the "modified Kaimal model," that the peak of the horizontal wind-speed power spectrum occurs approximately at the frequency n (s^{-1}), given by

$$n = 0.02\frac{V_{eh}}{z_{eh}} \tag{7.1}$$

where V_{eh} is the eave height wind speed (m s^{-1}) and z_{eh} is the eave height (3 m). With an eave-height average wind speed of 3.6 m s^{-1}, n is 0.024 s^{-1}, corresponding to a period, T, of 42 s. This mean wind speed, 3.6 m s^{-1}, is the 50th percentile wind speed for Spokane, Washington, over a period of 25 years (see Chapter 4).

The power, P (m^2 s^{-2}), at the peak of the spectrum (n = 0.024 s^{-1}) defines the size of the wind speed fluctuation. Teunissen (1980) approximates the power in the wind signal as

$$P = \frac{\frac{105 u_*^{\,2} z_{eh}}{V_{eh}} n}{\left(0.44 + \frac{33 z_{eh}}{V_{eh}} n\right)^{5/3}} \tag{7.2}$$

The shear velocity, u_* (m s^{-1}), is

$$u_* = \frac{\kappa V_{eh}}{\ln\left(\frac{z_{eh}}{z_0}\right)} \tag{7.3}$$

where z_0 is the roughness length (m) and κ is von Karman's constant (0.4). For the simulations presented here, z_0 equals 0.1 m, corresponding to the "countryside" boundary layer (see Chapter 3).

From equation (7.2), the wind speed fluctuation (calculated as $\sqrt{P}$) at the peak frequency in the power spectrum is 0.57 m s^{-1}. We use a wind speed with a mean of

3.6 m s^{-1} and a sinusoidally varying component of 0.57 m s^{-1} to define the wind dynamic pressure signal, $p_w(t)$ (Pa). In particular,

$$p_w(t) = \frac{1}{2}\rho\left(3.6 + 0.57\ \sin(2\pi n t)\right)^2 \tag{7.4}$$

where ρ is the air density (1.2 kg m^{-3}) and t is time (s).

For fluctuating winds, the predicted radon entry rate into the structure is a function of time. To quantify the impacts of a periodic wind, and to make comparisons to the case of steady winds, we compute a time-averaged, normalized radon entry rate, $\overline{E}$ (m^3 s^{-1}):

$$\overline{E} = \frac{\int_0^{NT} E(t)\ \mathrm{dt}}{NT} \tag{7.5}$$

where $E(t)$ is the normalized radon entry rate (m^3 s^{-1}) and N (-) is the number of periods over which the average is taken. The normalized radon entry rate is the radon entry rate (Bq s^{-1}) divided by C_∞ (Bq m^{-3}), the soil-gas radon concentration deep in the soil. A typical value for C_∞ is 30 kBq m^{-3} (Nazaroff, 1992). For the simulations reported here, the integral in equation (7.5) is evaluated for ten periods after the radon entry rate has reached a steady oscillation. RapidSTART simulations with the input wind signal defined by equation (7.4) are performed for soil permeabilities of 10^{-8} and 10^{-10} m^2. We take a 1 s time step for the 10^{-8} m^2 soil and a 5 s time step for the 10^{-10} m^2 soil.

7.4.2 Varying Wind Direction (Simulation Scenario 2)

This section describes two RapidSTART simulations, each using a real, fluctuating wind signal. The wind signal was collected as part of a full-scale radon mitigation experiment at the RFS. An MRI weather station placed 5 m above the ridge of the test house's roof simultaneously measured the wind speed and direction.

The first simulation assumes a constant wind speed, calculated as the average wind speed over a 9000 s section of the experimental data. The wind direction, however, is permitted to vary according to the real wind signal. The second simulation allows both the wind speed and direction to vary as the data prescribe.

As the wind-incidence angle varies, the relative depressurization of a real house also varies. In Chapter 4 we related the house depressurization to the wind dynamic pressure through a pressure coefficient. FLUENT (1993) simulations of the air flow over the house were used to determine this pressure coefficient. The RapidSTART simulations presented here apply the single pressure coefficient determined in Chapter 4 to all three wind-incidence angles. The method of Feustel (1985) indicates that the pressure coefficients for wind incident at 45° and 90° are 1.1 and 0.90 times the pressure coefficient for wind incident at 0°, respectively. This relatively small variation of pressure coefficient with wind direction should be included in future simulations.

Figure 7.1 presents a portion of the wind speed and direction signals collected at the RFS. The average wind speed and direction over 9000 s of the wind signal are 5.1 m s^{-1} and 201°, respectively. The simulated house is oriented to normalize the

average wind-incidence angle to 45° (i.e., the center of the ground-surface pressure field data). With this normalization, the wind has an incidence angle of 0°, 45°, and 90° for 12%, 71%, and 17% of the simulation period, respectively.

The simulations begin with ground-surface pressure, soil-gas pressure, and soil-gas concentration fields that correspond to the steady-state solution for a 5.1 m s^{-1} wind incident at 45° to the house. We compare RapidSTART predictions of the time-averaged radon entry rate to the predicted entry rate in the presence of a steady 5.1 m s^{-1} wind with a wind-incidence angle of 45°.

7.4.3 Diurnally Oscillating Wind Direction (Simulation Scenario 3)

Simulation scenario 3 investigates the impacts on the radon entry rate of a wind signal that oscillates diurnally between wind-incidence angles of 0° and 180°. The input wind signal for this simulation has a constant speed of 3.6 m s^{-1} and an incidence angle of 0° for 12 hours, followed by the same speed with an incidence angle of 180° for the next 12 hours. We simulate, for a soil permeability of 10^{-10} m^2, the diurnal oscillation of the wind direction for 10 days. The average radon entry rate of the resulting steady oscillation is compared to the predicted steady-state entry rate for wind incident at 0°.

A 180° rotation of the ground-surface pressure field and unit-step response for the 0° wind-incidence angle provided these inputs for a wind-incidence angle of 180°.

This simple conversion allowed us to avoid the necessity of an additional START simulation to generate the unit-step response at a wind-incidence angle of 180°.

7.5 Results and Discussion

7.5.1 Fluctuating Wind Speed (Simulation Scenario 1)

Figures 7.2 and 7.3 show time histories of the soil-gas and radon entry rates into the house for simulation scenario 1: a constant wind direction and a wind speed that has a mean of 3.6 m s^{-1} and a fluctuating component of 0.57 m s^{-1}. The soil permeabilities for Figures 7.2 and 7.3 are 10^{-8} and 10^{-10} m^2, respectively. For a soil permeability of 10^{-8} m^2, the average normalized radon entry rate over 10 periods of the steady oscillation is 3.4×10^{-6} m^3 s^{-1}. For a soil permeability of 10^{-10} m^2, the average steady-oscillation normalized radon entry rate is 7.5×10^{-5} m^3 s^{-1}. Both of these entry rates are only about 1% higher than the comparable steady-state entry rate for a constant wind speed of 3.6 m s^{-1} incident at 0° to the house.

The time-averaged basement depressurization and ground-surface pressures created by a fluctuating wind speed are larger than those generated by a constant wind speed, even though the two cases have the same average wind speed. In particular, the time-averaged wind dynamic pressure, $\overline{p_w}$ (Pa), can be expressed as

$$\overline{p_w} = \frac{\int_0^T p_w(t)\,\mathrm{dt}}{T} = \frac{1}{2}\rho V_{eh}^{\,2} + \frac{1}{2}\rho\left(V_{eh}'\right)^2 \tag{7.6}$$

where V_{eh}' (m s^{-1}) is the size of the fluctuating component of the wind speed. For the case presented here, V_{eh}' is 0.57 m s^{-1}, making the average of the fluctuating wind dynamic pressure about 1% larger than the steady value. The larger average wind dynamic pressure likely accounts for the 1% increase in the average radon entry rate. For these two soil permeabilities, a fluctuating wind speed has a negligibly small impact on the radon entry rate.

We expect, however, different effects for tighter soils and larger amplitude, higher frequency wind speed fluctuations. At some combination of lower soil permeability and higher frequency, larger amplitude wind speed fluctuations, the building will begin "pumping", i.e., forcing basement air into the soil over a portion of the wind speed signal. Robinson et al. (1995) have shown an analogous phenomenon to be important in the presence of fluctuating atmospheric pressures.

7.5.2 Varying Wind Direction (Simulation Scenario 2)

This section presents the results of two simulations conducted at a soil permeability of 10^{-8} m^2. We base the simulations on a 9000 s section of the RFS wind signal (see Figure 7.1). Figure 7.4 presents a portion of the soil-gas and radon entry rates predicted by RapidSTART for the first simulation. Here, the input wind signal

has a constant speed of 5.1 m s^{-1} and a direction that varies according to the real wind signal. The time-averaged normalized radon entry rate over the 9000 s is 1.9×10^{-6} m^3 s^{-1}. For comparison, the normalized radon entry rate for a steady 5.1 m s^{-1} wind with a wind-incidence angle of 45° is 1.7×10^{-6} m^3 s^{-1}. Therefore, ignoring the fluctuating wind direction produced a 12% error in the predicted radon entry rate.

Figure 7.5 presents a portion of the soil-gas and radon entry rates predicted by RapidSTART for the second simulation. In this case, both the wind speed and direction vary according to the RFS wind signal. The time-averaged normalized radon entry rate over the 9000 s period of the simulation is 2.0×10^{-6} m^3 s^{-1}. The combination of the fluctuating wind speed and direction increased the predicted radon entry rate over the steady prediction by 21%.

Several factors associated with a fluctuating wind direction could contribute to an increase in the predicted radon entry rate. First, the steady-state soil-gas entry rates are different for wind-incidence angles of 0° and 90° than for a wind-incidence angle of 45°. Thus, for 29% of the simulation period, a different driving force for radon entry (larger in this case) existed. Second, the transient soil-gas pressure field established by the fluctuating wind direction affects the soil-gas concentration field. As we show in the next section, this effect can be important when the steady-state radon concentration fields established by the various wind-incidence angles are significantly different. Finally, although not accounted for in this simulation, in a real house the basement depressurization changes as the wind direction shifts. This fluctuation in basement

pressure can cause pressure gradients near the footer-slab crack, thereby affecting the soil-gas radon concentration field and the radon entry rate.

7.5.3 Diurnally Oscillating Wind Direction (Simulation Scenario 3)

This section presents the RapidSTART simulation predictions for the case of a wind signal with a constant speed of 3.6 m s^{-1} and a direction that oscillates 180° diurnally. Figure 7.6 shows a ten-day history of the predicted radon entry rate into the basement (a) and the wind-incidence angle (c). Figure 7.6 (b) shows a parameter, C_{char} (-), which represents the radon source available for entry into the basement. C_{char} is the average of the normalized radon concentration in a plane surface bounded by the lower interior edges of the basement footers. Chapter 4 applied the same parameter to demonstrate the flushing of soil-gas radon caused by steady winds (see Figure 4.7).

The simulation shown in Figure 7.6 began with a constant wind speed of 3.6 m s^{-1} and a wind-incidence angle of 0°. We imposed this boundary conditions until the radon concentration field reached steady state (the figure does not show this portion of the simulation). The first half day of simulation shows no change in the radon entry rate since, during this period, the boundary conditions are equivalent to those of the steady-state solution.

After about eight simulation days the radon entry rate into the basement has reached a steady oscillation. The time-averaged steady-oscillation radon entry rate is 9.5×10^{-5} m^3 s^{-1}. The corresponding steady-state normalized radon entry rate in the

presence of a 3.6 m s^{-1} wind with an incidence angle of 0° is 7.3×10^{-5} m^3 s^{-1}. Therefore, the diurnally oscillating wind direction resulted in about a 30% increase in the average radon entry rate into the basement.

A higher time-averaged soil-gas radon concentration near the basement is responsible for this increase in radon entry rate. As Figure 7.6 (b) indicates, the source of radon available for entry into the basement increased over the ten-day simulation period. The time-averaged steady-oscillation value for C_{char} is 0.86, a 20% increase over the initial value of 0.71.

We explain the increase in C_{char} by examining the impact of the oscillating wind direction on the soil-gas radon concentration field. Figure 7.7 shows a contour plot of the normalized soil-gas radon concentration surrounding the basement in a section centered on the house and parallel to a steady wind. In this figure, the constant wind speed and direction are 3.6 m s^{-1} and 0°, respectively. Notice the relatively high soil-gas radon concentration on the leeward side of the basement compared to the windward side. This concentration profile results from the wind-induced bulk soil-gas flow under the basement (see Section 4.5.2).

As the wind switches direction from 0° to 180°, the soil gas on the leeward side of the house moves toward the basement and the entry points of the building. Over time, the diurnally oscillating ground-surface pressure field produces a relatively enriched radon concentration field adjacent to the house. Therefore, the radon entry rate increases, even though the soil-gas entry rate remains the same.

7.6 Conclusions

We performed three sets of RapidSTART simulations to investigate the impacts of fluctuating winds on radon entry rates. The first set of simulations isolated the effect of a fluctuating wind speed (with constant wind direction) on the radon entry rate. RapidSTART took as input a sinusoidal wind speed signal with a period of 42 s, a mean of 3.6 m s^{-1}, and a fluctuating component of 0.57 m s^{-1}. These parameters correspond to the peak in a typical horizontal wind-speed power spectrum. The simulations indicated, for both soil permeabilities, that wind speed fluctuations of this character have a negligible impact on the radon entry rate.

The second set of simulations investigated the impacts of a fluctuating wind direction on radon entry rates. A wind signal collected at the RFS was used as input to RapidSTART. We calculated the time-averaged radon entry rate over a 9000 s period, and compared this value to the predicted steady-state radon entry rate. For a soil permeability of 10^{-8} m^2, the time-averaged radon entry rate predicted in the presence of a wind with constant speed and fluctuating direction was 12% higher than if a steady wind had been assumed. A simulation was also performed that allowed both the wind speed and direction to vary as prescribed by the real wind signal. This combination increased the time-averaged radon entry rate by 21% over the steady-state prediction.

The final simulation considered a wind signal with a constant speed and a direction that oscillated 180° diurnally. The fluctuating wind direction increased the time-averaged radon entry rate by about 30%. The diurnal oscillation of the wind

established a relatively enriched soil-gas radon concentration field adjacent to the basement. Although the soil-gas entry rate is unchanged, the larger source of radon near the entry points of the building results in an increased radon entry rate.

These simulations provide insight into the magnitude of the effect fluctuating winds have on radon entry into buildings. For soil permeabilities of 10^{-8} and 10^{-10} m^2, fluctuating wind speeds characteristic of the peak in the wind-speed power spectrum have a negligible effect on the radon entry rate. Ignoring the fluctuating components of wind speed and direction for the RFS wind signal altered the radon entry rate by 21%. A diurnally oscillating wind signal led to an increase in the predicted radon entry rate of 30%. We conclude that, for the soil permeabilities considered, the overall effect of transient winds on radon entry rates is small to moderate. The impact of fluctuating winds on radon entry in tight soils remains an unresolved issue.

This chapter has demonstrated the applicability of RapidSTART to the modeling of a geometrically complex, transient soil-gas and radon transport problem. Comparable simulations with a finite-difference or finite-element model would have required three orders of magnitude more computational time, rendering such models practically useless for this type of simulation. In the context of wind-induced soil-gas and radon transport, the use of RapidSTART has made the analysis of transient winds tractable.

7.7 References

DSMA Atcon Ltd. (1985) A computer study of soil gas movement into buildings, report 1389/1333, Department of Health and Welfare, Ottawa, Canada.

Feustel H. E. (1985) Development of a simplified multizone infiltration model, report LBL-19005, Lawrence Berkeley Laboratory, Berkeley, CA.

FLUENT (1993) v4.2, Fluent Incorporated, Centerra Resource Park, 10 Cavendish Court, Lebanon, NH.

Nazaroff W. W. (1992) Radon transport from soil to air, *Reviews of Geophysics* **30**, 137-160.

Robinson A. L., Sextro R. G., and Riley W. J. (1995) Soil-gas entry into houses driven by atmospheric pressure fluctuations, part 2 --- The influence of soil and structural factors, report LBL-38233, Lawrence Berkeley National Laboratory, Berkeley, CA.

Teunissen H. W. (1980) Structure of mean winds and turbulence in the planetary boundary layer over rural terrain, *Journal of Wind Engineering and Industrial Aerodynamics* **6**, 188-221.

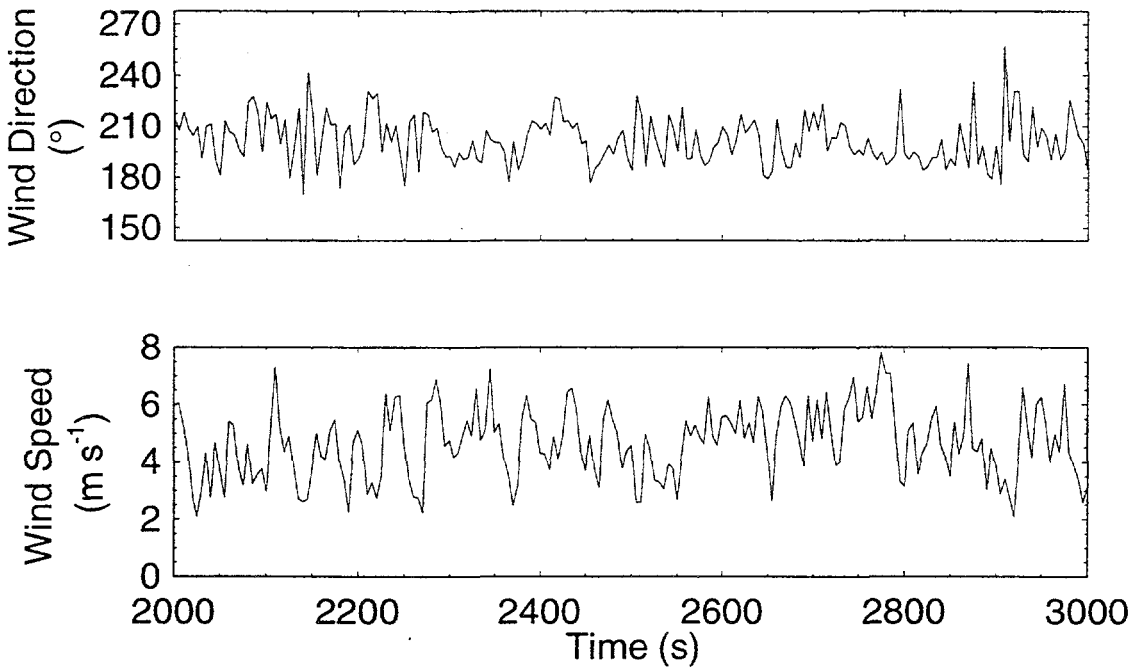

Figure 7.1. A portion of the Richmond Field Station wind data. The signal used in the RapidSTART simulation is 9000 s long (simulation scenario 2).

/riley/rfs-wind/0403-0-5a.tec
/riley/rfs-wind/rfs-wind.lay

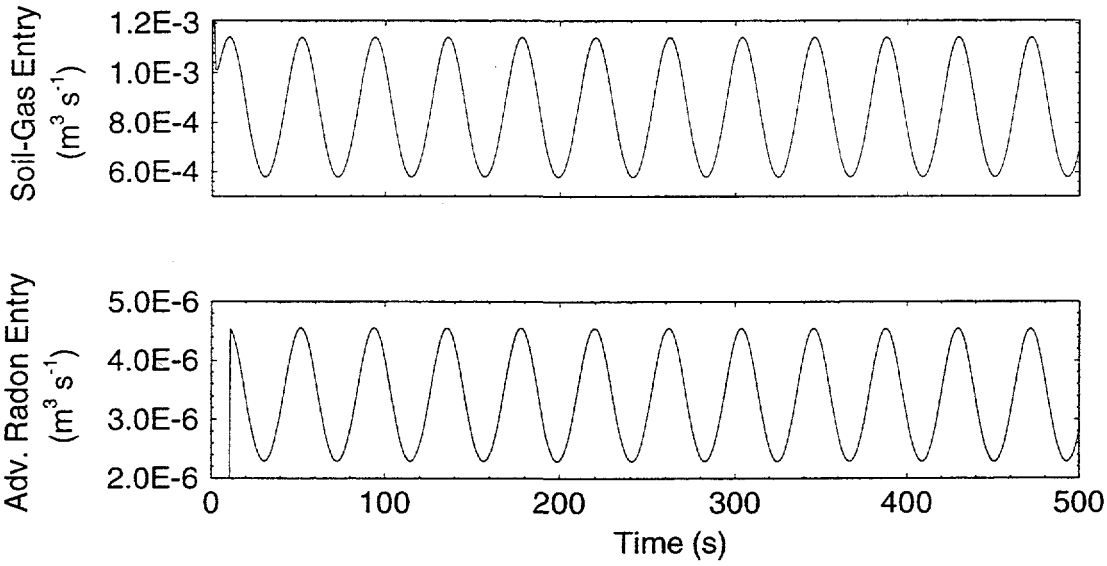

Figure 7.2. Predicted soil-gas and normalized radon entry rates into a building for a constant wind direction and a wind dynamic pressure given by equation 7.4. The soil permeability is 10^{-8} m^2 (simulation scenario 1).

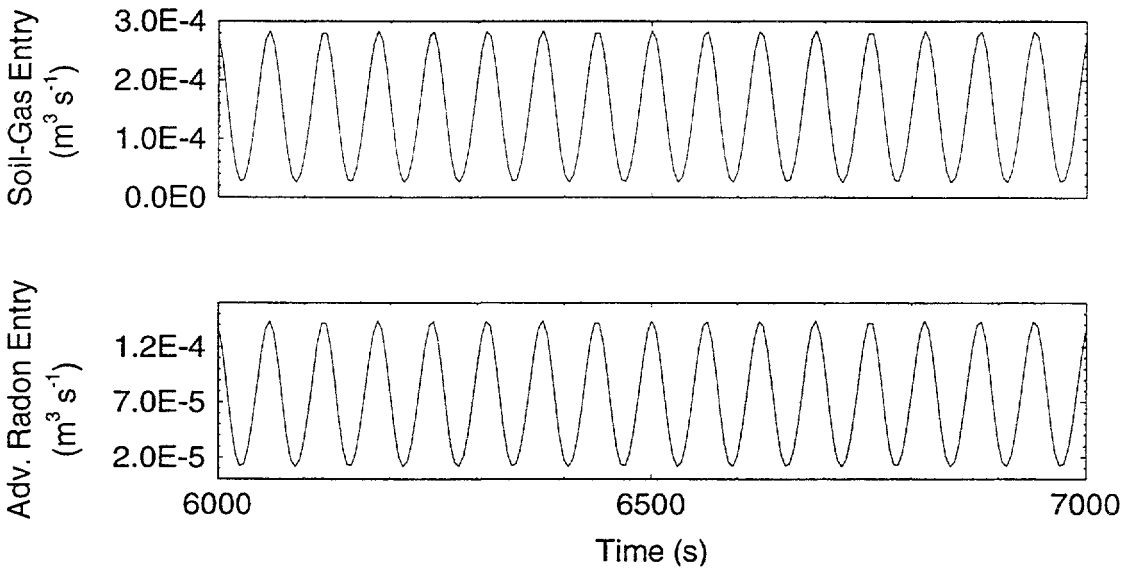

Figure 7.3. Predicted soil-gas and normalized radon entry rates into a building for a constant wind direction and a wind dynamic pressure given by equation 7.4. The soil permeability is 10^{-10} m^2 (simulation scenario 1).

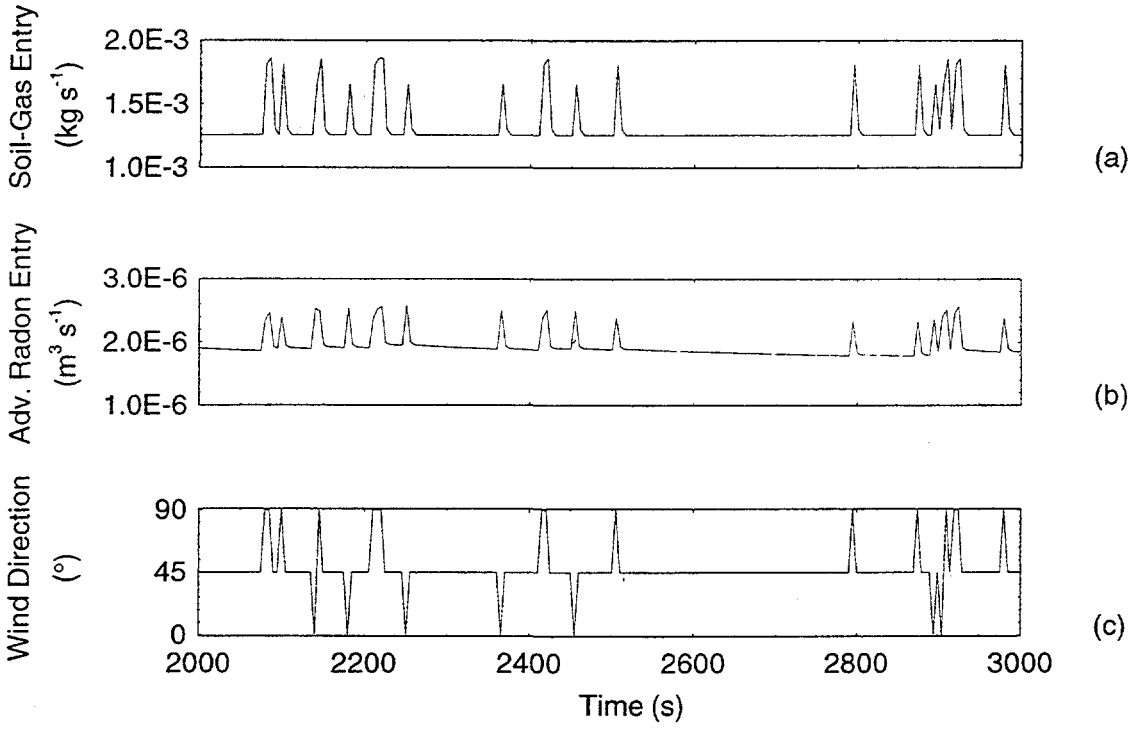

Figure 7.4. Predicted soil-gas entry rate, normalized radon entry rate, and wind direction for simulation scenario 2. The wind speed is held constant at 5.1 m s^{-1}, but the wind direction follows the data illustrated in Figure 7.1. The soil permeability is 10^{-8} m^2.

/transient/duhamel/scott-2d/flow-duh-k8-rfs7.out
/transient/duhamel/scott-2d/fig8-4.lay

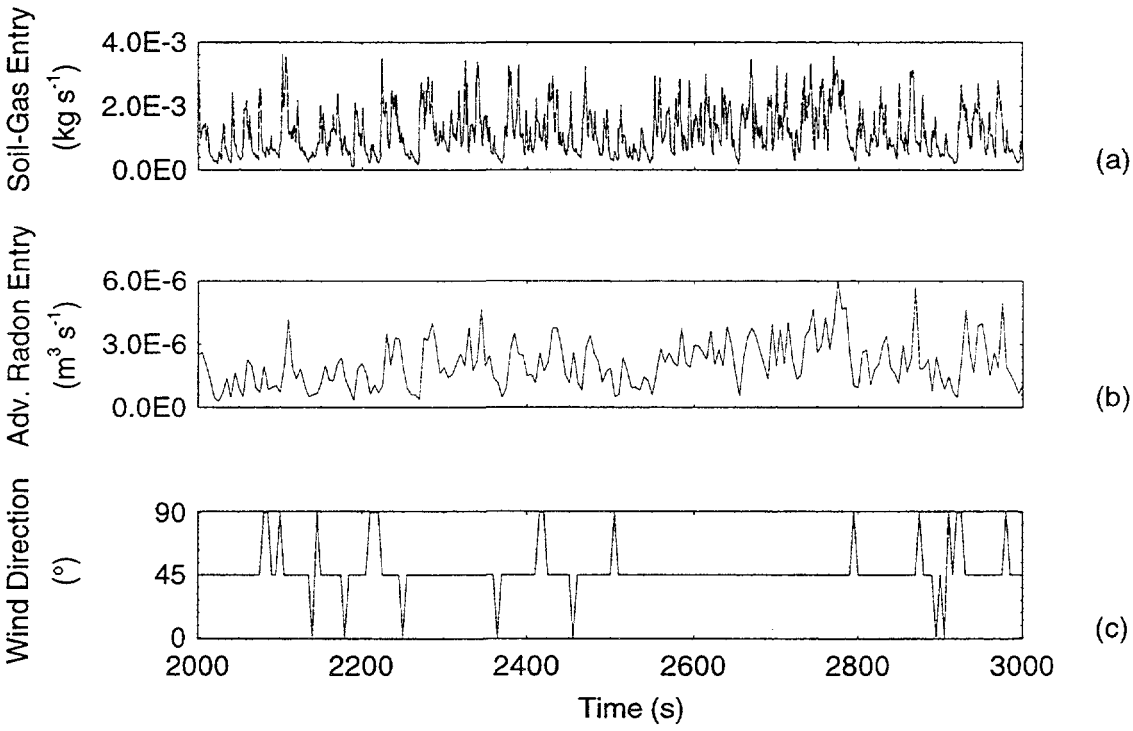

Figure 7.5. Predicted soil-gas entry rate, normalized radon entry rate, and wind direction for simulation scenario 2. The wind speed and direction follow the data presented in Figure 7.1. The soil permeability is 10^{-8} m^2.

/transient/duhamel/scott-2d/flow-duh-k8-rfs8.out
/transient/duhamel/scott-2d/fig8-5.lay

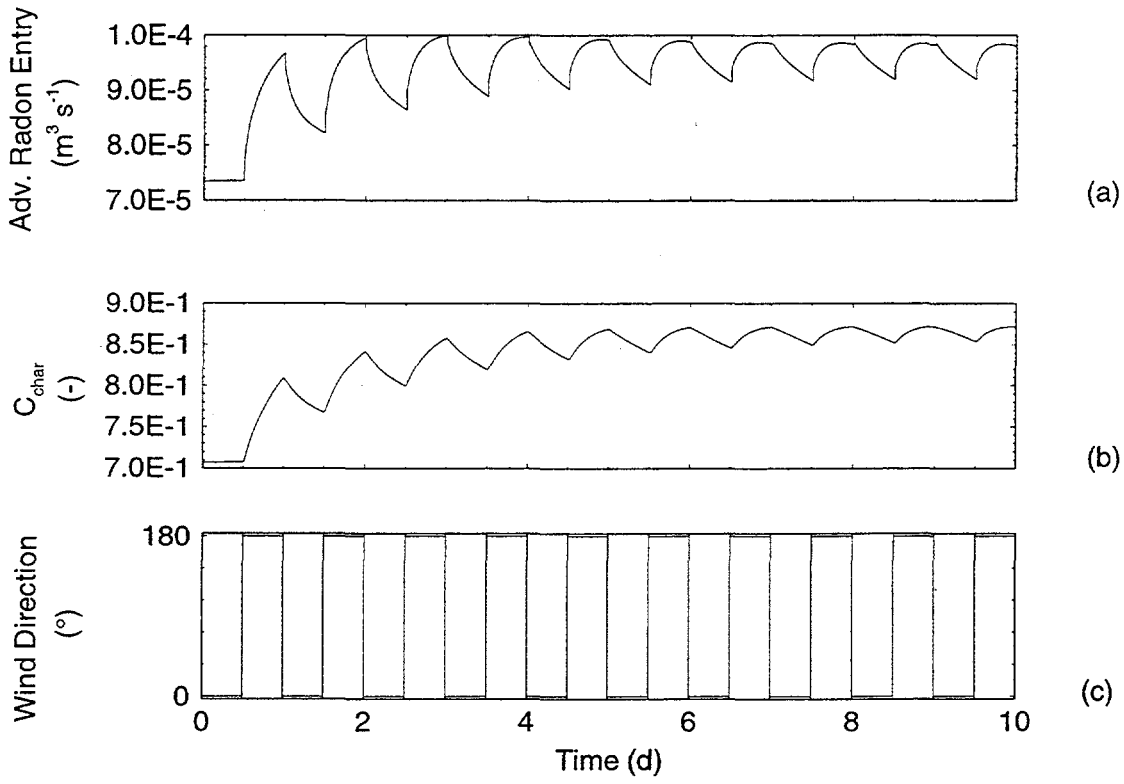

Figure 7.6. Predicted normalized radon entry, average soil-gas radon concentration, and wind direction for a wind signal that flips diurnally between 0° and 180° and has a constant speed of 3.6 m s^{-1}. The soil permeability is 10^{-10} m^2 (simulation scenario 3).

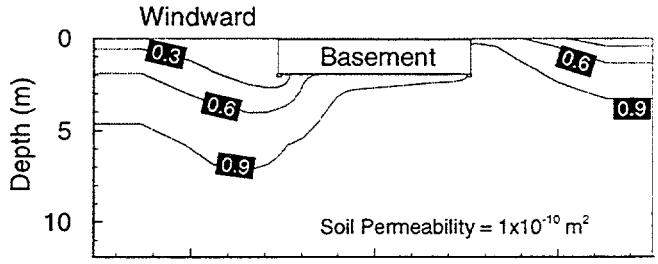

Figure 7.7. Normalized soil-gas radon concentration field near the basement for a wind speed of 3.6 m s^{-1} and a soil permeability of 10^{-10} m^2 (simulation scenario 3). This radon concentration field corresponds to the beginning of the simulation shown in Figure 7.6.

/duhamel/transient/scott-2d/fig8-7.lay
/duhamel/transient/scott-2d/w3-5-x18-2.tec

CHAPTER 8

CONCLUSIONS

8.1 Summary

The interaction of the atmospheric boundary layer with buildings and near-surface soils can strongly affect soil-gas and radon entry into houses. In particular, radon entry rates and indoor concentrations can be dominated by the ground-surface pressure field created when wind blows over a building. Before this work, the impact of wind on indoor radon concentrations, and therefore human exposures, was poorly understood.

We began our investigation of this subject by performing wind-tunnel measurements of the wind-induced ground-surface pressure field. Experiments were conducted for several wind-incidence angles, two house geometries, and two atmospheric boundary layer structures. The experimental results demonstrated that perturbations in the house geometry and in the atmospheric boundary layer structure (i.e., the roughness length and displacement height) do not significantly affect the wind-induced ground-surface pressure field.

We also performed numerical simulations of wind's interactions with a building's superstructure using a commercial computational fluid dynamics code (FLUENT, 1993). Comparisons between the simulated and experimentally measured ground-surface pressure fields were made to determine whether, for this problem,

computational methods are a viable alternative to the relatively expensive wind-tunnel experiments. Although k-ε turbulence models have fundamental limitations when applied to a system with separated flow (Murakami, 1993), we found FLUENT's predictions sufficiently accurate to simulate wind-induced soil-gas and radon transport.

The experimentally measured ground-surface pressure fields were used to investigate the impacts of steady winds on soil-gas and radon transport and entry into buildings. We also employed a previously tested three-dimensional numerical model of soil-gas and radon transport (Gadgil et al., 1991; Bonnefous et al., 1992) and an established model for determining ventilation rates in the presence of wind (Sherman, 1992). With these tools and experimental data, we examined the complex soil-gas flow patterns produced by the wind-induced ground-surface pressure field. This investigation demonstrated that the bulk soil-gas flow created by wind flushes radon from the soil adjacent to the basement. For a broad range of soil permeabilities, two wind speeds, and two wind directions, we quantified the extent of this flushing and the accompanying decrease in radon entry rates and indoor radon concentrations.

The reduction in radon entry caused by the wind-induced ground-surface pressure field depends strongly on soil permeability. For example, for a wind speed of 8.3 m s^{-1} and a soil permeability of 10^{-11} m^2, the predicted radon entry rate is a factor of 3 lower than predicted while ignoring the wind-induced ground-surface pressure field. For the same wind speed, and a soil permeability of 10^{-9} m^2, the predicted radon entry rate is reduced by a factor of 60.

We also examined experimental measurements of the time-dependent soil-gas radon concentration beneath several houses as a function of wind conditions. These measurements support our contention that wind can reduce the soil-gas radon concentration adjacent to a house. This combination of experimental and modeling evidence leads us to conclude that steady wind-induced ground-surface pressure fields play a significant role in determining radon entry rates into residential buildings.

Motivated by the large impacts of steady winds, we became interested in the effects of fluctuating winds on radon transport and entry into houses. At that time, models did not exist to simulate the three-dimensional, transient soil-gas and radon flows generated in the presence of real winds. As a result, the impacts of transient winds on radon entry rates were unknown. We therefore developed a suite of tools to examine this problem.

The first of these tools is a transient, three-dimensional, finite-difference model named START (*S*imulation of *T*ransient *A*ir and *R*adon *T*ransport). START combines previously reported techniques for simulating steady soil-gas and radon transport (Loureiro et al., 1990; Bonnefous, 1994) and a temporal discretization method described by Patankar (1980). To validate START, we compared simulation predictions to several analytical solutions. Also, START simulation predictions were compared to experimental measurements of soil-gas and radon entry rates into a structure located at the Small Structures Facility (Robinson and Sextro, 1995). Over a two-hour period, and without any fitted parameters, START predicted the time-averaged radon entry rate into the structure to within 3% of the experimental

measurements. These analytical and experimental tests demonstrate that START can accurately simulate transient, three-dimensional soil-gas and radon flows, and that the model can simulate both one- and two-dimensional geometries efficiently. However, because the three-dimensional house and soil system we wish to consider requires a fine spatial and temporal discretization, the computational requirements for a START simulation in the presence of fluctuating winds can be prohibitive. For this reason, we employ START as a preprocessor for the RapidSTART model, described below.

To make the transient, three-dimensional wind simulations tractable, we developed a novel modeling technique based on Duhamel's theorem (Duhamel, 1833; Myers, 1987). The model, named RapidSTART, applies Duhamel's theorem to compute the soil-gas pressure and velocity fields generated by fluctuating pressure boundary conditions. Given the transient velocity field, we then use a finite-difference method to calculate the soil-gas radon concentration field. Implementing the Duhamel technique in the RapidSTART model led to a reduction in simulation runtime, compared to the standard finite-difference model, of the order of 1000.

RapidSTART requires as input a unit-step response, generated by START, to characterize the temporal response of the soil-gas pressure field to a step change in the pressure boundary conditions. For the simulations presented in this dissertation, the fluctuating ground-surface pressure field and the basement depressurization are the boundary conditions of interest. We use the eave-height wind dynamic pressure as the independent variable that controls the wind-speed dependence of the ground-surface pressure field and basement depressurization. RapidSTART models the impacts of

fluctuating wind directions on the soil-gas pressure field by applying the three ground-surface pressure fields described in Chapter 3. We also present a general method to generate a finer and broader discretization of the wind-incidence angle.

We performed several validation tests of the RapidSTART model. First, simulation predictions of soil-gas and radon transport in a one-dimensional soil column were compared to analytical solutions. RapidSTART predicted conditions in the soil column very accurately. Second, we compared RapidSTART and START predictions of soil-gas and radon entry into a two-dimensional section of a house exposed to a fluctuating wind speed. The match between the RapidSTART and START simulations was excellent. Finally, we compared RapidSTART simulation predictions with experimental measurements of the radon entry rate into a basement at the Small Structures Facility (Robinson and Sextro, 1995). RapidSTART's predictions of the average radon entry rate over a two-hour period was within 14% of the experimental measurements. This combination of analytical and experimental validation tests demonstrates RapidSTART's ability to accurately simulate transient, three-dimensional soil-gas and radon transport and entry into buildings.

Using the RapidSTART model, we explored the impacts of fluctuating wind speeds and directions on radon entry into a prototypical house. Simulations were performed for several wind signals and two soil permeabilities. Our results indicate that wind speed fluctuations characteristic of the peak in the wind-speed power spectrum have a negligible impact on the time-averaged radon entry rate into the building. However, ignoring the fluctuating speed and direction of a real wind signal

led to errors of 21% in the predicted radon entry rate. Errors of 30% in the predicted radon entry rate occurred when a diurnal oscillation of 180° in wind direction was ignored. We conclude that, for the soil permeabilities considered, the fluctuating components of wind have a small to moderate impact on predicted radon entry rates. We expect these conclusions also apply qualitatively to slab-on-grade and crawl space houses.

8.2 Directions for Future Research

The impacts of fluctuating winds on radon entry into buildings situated in low-permeability soils remains an unresolved issue. RapidSTART simulations of tighter soil conditions will allow us to investigate the impacts of wind-induced soil-gas pumping on radon entry rates.

For tight soil permeabilities (i.e., less than about 10^{-11} m^2), the runtime memory requirements of RapidSTART can be large. To address this problem, we introduced the concept of curve-fitting the weighting functions at each point in the soil block over the time required for the unit-step response to reach steady state. The exponential curve fit that performed well for a soil permeability of 10^{-8} m^2 may be insufficiently precise for tighter soils. One should, therefore, consider other curve-fitting techniques. Since the unit-step response is a smooth function of time, we expect this effort will be straightforward.

To thoroughly characterize the effects of fluctuating winds, one could use RapidSTART to generate a frequency response of the radon entry rate into a

prototypical house. For a broad range of soil permeabilities, such an investigation would determine the relative attenuation or enhancement of the radon entry rate as a function of wind speed fluctuation frequency and magnitude.

The transport and entry into buildings of other subsurface contaminants, such as VOC's, can be affected by fluctuating environmental conditions (Garbesi, 1988; Little et al., 1992). Understanding the impacts these conditions have on contaminant entry into buildings is critical to predicting and controlling human exposures. The results and the tools presented in this dissertation apply to the development of such an understanding. For example, the current version of RapidSTART can predict the soil-gas flow field responsible for the entry of any gaseous contaminant into a house. Including retardation coefficients and biological degradation terms in the concentration field computations (Falta et al., 1995) will allow RapidSTART to simulate subsurface VOC transport. With these modifications, RapidSTART could be used to study the environmental and structural factors governing indoor air concentrations of VOC's that originate in soil.

The design of passive or low-energy radon mitigation systems requires an understanding of the interactions of wind with the mitigation system and the soil-gas pressure and concentration fields. RapidSTART could be applied to understand the impacts of steady and fluctuating winds on the system's performance, thereby aiding design improvements.

The linear superposition technique applied in the RapidSTART model may also have application to the simulation of other complex, transient linear systems. For

example, the technique could prove useful in heat transfer models that simulate building energy use (Simulation Research Group, 1991) and structural and earthquake building models.

8.3 Closing Remark

The research presented in this dissertation has given us an understanding of the impacts of wind on radon entry into buildings. Although the building and soil systems studied were intentionally simplified, the results and insights apply to a range of problems. The development and validation of the RapidSTART model represents an important result of this research. We demonstrated that RapidSTART accurately predicts soil-gas and radon entry rates into buildings while reducing simulation runtimes by three orders of magnitude. To our knowledge, the research presented here represents the first time this technique has been applied to a subsurface contaminant transport problem.

The simulation technique employed in RapidSTART presents a broad range of potential applications for the simulation of other complex, linear systems. Because of the potential to drastically reduce simulation runtimes while simultaneously maintaining the accuracy of the underlying model, investigations into other applications may prove fruitful.

8.4 References

Bonnefous Y. C. (1994) Etude numerique des systemes de ventilation du sol pour diminuer la concentration en radon dans l'habitat, Ph.D. Thesis, report LBL-34244, Lawrence Berkeley National Laboratory, Berkeley, CA.

Bonnefous Y. C., Gadgil A. J., Fisk W. J., Prill R. J., and Nematollahi A. R. (1992) Field study and numerical simulation of subslab ventilation systems, *Environ. Sci. Technol.* **26**, 1752-1759.

Duhamel (1833) Memoire sur la methode generale relative au mouvement de la chaleur dans les corps solides plonges dans les milieux dont la temperature varie avec le temps, *J. Ec. Polyt. Paris* **14**, 20.

Falta R. W., Pruess K., Finsterle S., and Battistelli A. (1995) T2VOC user's guide, report LBL-36400, Lawrence Berkeley National Laboratory, Berkeley, CA.

FLUENT (1993) v4.2, Fluent Incorporated, Centerra Resource Park, 10 Cavendish Court, Lebanon, NH.

Gadgil A. J., Bonnefous Y. C., Fisk W. J., Prill R. J., and Nematollahi A. (1991) Influence of subslab aggregate permeability on SSV performance, report LBL-31160, Lawrence Berkeley National Laboratory, Berkeley, CA.

Garbesi K. (1988) Experiments and Modeling of the Soil-Gas Transport of Volatile Organic Compounds into a Residential Basement, MS Thesis, report LBL-25519 Rev., Lawrence Berkeley National Laboratory,

Little J. C., Daisey J. M., and Nazaroff W. W. (1992) Transport of subsurface contaminants into buildings: An exposure pathway for volatile organics, *Environ. Sci. Technol.* **26**, 2058-2066.

Loureiro C. O., Abriola L. M., Martin J. E., and Sextro R. G. (1990) Three-dimensional simulation of radon transport into houses with basements under constant negative pressure, *Environ. Sci. Technol.* **24**, 1338-1348.

Murakami S. (1993) Comparison of various turbulence models applied to a bluff body, *J. Wind Eng. Ind. Aerodyn.* **46 & 47**, 21-36.

Myers G. E. (1987) *Analytical Methods in Conduction Heat Transfer,* Genium Publishing Corporation, Schenectady, NY.

Patankar S. V. (1980) *Numerical Heat Transfer and Fluid Flow,* Hemisphere Publishing, New York, NY.

Robinson A. L. and Sextro R. G. (1995) Direct measurements of soil-gas entry into an experimental basement driven by atmospheric pressure fluctuations, *Geophysical Research Letters* **22**, 1929-1932.

Sherman M. H. (1992) Simplified modeling for infiltration and radon entry, report LBL-33962, Lawrence Berkeley National Laboratory, Berkeley, CA.

Simulation Research Group (1991) DOE-2 basics, report LBL-29140, Lawrence Berkeley National Laboratory, Berkeley, CA.